High-resolution deep-tissue quantitative optical tomography

van der Horst, Jelle

DOI
10.4233/uuid:1b5bffc3-b7f9-49a1-91ea-ebbf25b1f73f

Publication date
2018

HIGH-RESOLUTION DEEP-TISSUE QUANTITATIVE OPTICAL TOMOGRAPHY

HIGH-RESOLUTION DEEP-TISSUE QUANTITATIVE OPTICAL TOMOGRAPHY

Proefschrift

ter verkrijging van de graad van doctor
aan de Technische Universiteit Delft,
op gezag van de Rector Magnificus Prof. dr. ir. T. H. J. J. van der Hagen,
voorzitter van het College voor Promoties,
in het openbaar te verdedigen op donderdag 14 juni 2018 om 15:00 uur

door

Jelle VAN DER HORST

Master of Science in Applied Physics, Technische Universiteit Eindhoven, Nederland
geboren te Utrecht, Nederland.

Dit proefschrift is goedgekeurd door de

promotor: Prof. dr. ir. L. J. van Vliet
copromotor: Dr. J. Kalkman

Samenstelling promotiecommissie:

Rector Magnificus,	voorzitter
Prof. dr. ir. L. J. van Vliet,	Technische Universiteit Delft, promotor
Dr. J. Kalkman,	Technische Universiteit Delft, copromotor
Onafhankelijke leden:	
Prof. dr. B. Rieger	Technische Universiteit Delft
Prof. dr. J. F. de Boer	Vrije Universiteit Amsterdam
Prof. dr. A. P. Mosk	Universiteit Utrecht
Prof. dr. J. Sijbers	Universiteit Antwerpen
Dr. A. Bassi	Politecnico Milano
Prof. dr. I. T. Young	Technische Universiteit Delft, reservelid

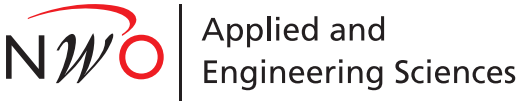

Printed by: Ridderprint BV
Front & back: Contour image of a sinogram with a noisy background.

ISBN 978-94-6299-950-3

An electronic version of this dissertation is available at
http://repository.tudelft.nl/.

CONTENTS

1

INTRODUCTION

1

1.1. 3D IMAGING IN THE LIFE SCIENCES

Ever since the invention of the first microscope, imaging techniques have been expanding the borders of knowledge in the life sciences. After the microscope, many imaging modalities have been developed that image biological structures at various length scales and provide different modes of contrast. Currently, a wide range of instruments are available for scientist to create, manipulate and visualize biological systems. In deciding which imaging technique to use, multiple factors are important. As expected, spatial resolution, imaging speed, contrast, and imaging depth are important in the choice of the most optimal imaging system. However, also the type of sample, ease of use, and cost are generally a concern.

To create an image of a sample, an interaction with an information carrier, a wave or collection of particles, is needed. The information carrier can be electromagnetic waves (light, X-ray, terahertz, MRI, gamma radiation), pressure waves (ultrasound), or particles (electron microscopy). The sample interaction with the information carrier can be based on transmission, emission, reflection, elastic scattering, Raman scattering, and fluorescence. The specific characteristic of the interaction determines the type of (functional) contrast that can be visualized in the image. For imaging biological tissue to a sufficient depth, all imaging techniques require that their interaction with water is weak. The water absorption is small for X-ray, visible, and radio wavelengths. The information carrier also determines the range of spatial resolutions that can be achieved. At small imaging depths this is often limited by diffraction of the information carrying wave. At larger imaging depths the resolution is often limited by sample interaction or detection specifics.

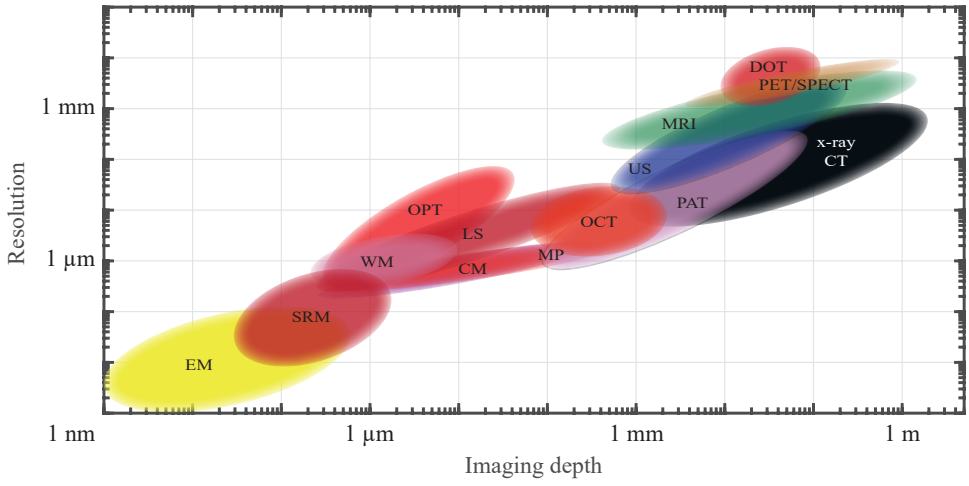

Figure 1.1: Approximate ranges of resolution and imaging depth for 3D imaging techniques in the life sciences. EM: electron microscopy, SRM: super-resolution microscopy, WM: widefield microscopy, OPT: optical projection tomography, LS: light sheet microscopy, CM: Confocal microscopy, MP: Multi-photon microscopy, OCT: Optical coherence tomography, PAT: Photoacoustic tomography, US: Ultrasound, MRI: Magnetic resonance imaging, CT: computed tomography, DOT: Diffuse optical tomography, PET: Positron emission tomography, and SPECT: Single photon emission computed tomography. Data combined from [1–6].

Figure 1.1 gives an overview of various 3D imaging techniques used for imaging in the life sciences and their approximate range of operation in terms of imaging depth and spatial resolution. Electron microscopy provides the highest resolution of the techniques described here. It is particularly suited for imaging of sub-cellular structures in structural biology. Because of the scattering of electrons by air, electron microscopy operates in vacuum and is therefore not compatible with in-vivo imaging.

A number of optical techniques operates in the range between 0.1 μm and 1 mm of imaging depth, visualized by the red and purple ellipses in figure 1.1. In this range the amount of light absorption and scattering in biological tissue is limited making it possible to collect ballistic photons (photons that do not scatter) to perform imaging. Conventional widefield microscopy operates with sample thicknesses up to approximately 20 μm. In this range the number of scattered photons is negligible compared to the ballistic photons. The resolution of widefield microscopy is limited by light diffraction. Recently, several super-resolution microscopy techniques have been developed that bridge the gap between optical microscopy and electron microscopy. Light sheet microscopy, confocal microscopy, and multi-photon microscopy, are techniques developed to cope with imaging thicker samples by reducing the effect of scattered photons. Optical projection tomography (OPT) is a tomographic imaging technique that creates 3D images from a collection of projections created with a widefield imaging technique. The resolution and imaging depth are comparable to that of widefield microscopy. Optical coherence tomography (OCT) creates images based on light backscattered from a sample. Depth sectioning in OCT is obtained by low-coherence interferometry.

Techniques to image tissue on the scale of human organs/whole body are diffuse optical tomography (DOT), magnetic resonance imaging (MRI), ultrasound (US), and X-ray computed tomography (CT). DOT is a low resolution optical imaging technique for deep tissue imaging based on measurements of photons that have been scattered many times. MRI manipulates and measures the precession of nuclear spins of hydrogen atoms in a sample in a strong magnetic field. X-ray CT is a tomographic imaging technique in which high-resolution images are created from a set of X-ray transmission images. The main disadvantage of X-ray CT is the use of ionizing radiation and the lack of contrast between different types of soft tissue. X-ray CT is also applied to achieve high-resolution imaging of small animals using a miniaturized device called micro-CT. Ultrasound imaging is based on the measurement of backscattering of high-frequency sound waves in a sample. Ultrasound, does not involve ionizing radiation and is particularly suited for in-vivo imaging (parts) of the human body. Positron emission tomography (PET) and single photon emission computed tomography (SPECT) are 3D medical imaging techniques based on the emission of gamma radiation. From a measurement at multiple angles of the gamma radiation, the 3D distribution of tracers is reconstructed. The use of tracers makes it possible to label specific types of molecules and obtain functional information.

Photoacoustic tomography (PAT) is a combination of optical and ultrasound imaging techniques. In PAT, a light pulse is send into a sample. The absorption of the energy of the light and the subsequent heating of the material creates ultrasound pulses in the tissue. The generated ultrasound waves are detected using US transducers. Because scattering of sound waves in tissue is much weaker than scattering of light, PAT allows for a larger imaging depth compared to fully optical techniques. Compared to US, PAT

1

provides stronger contrast generated by optical absorption.

1.2. OPTICAL IMAGING

Optical techniques are widely used in 3D imaging of biological samples, as evident by the multitude of optical techniques in the range between 0.1 μm and 1 mm of imaging depth in figure 1.1. Optics provides relatively low cost imaging functionality without the need for large and complicated facilities nor the use of ionizing radiation. Both structural and functional information can be obtained from optical measurements. Structural information is obtained from optical techniques providing absorption, scattering or phase contrast. Fluorescent markers, such as green fluorescent protein (GFP), are used to label specific proteins and image their spatial distribution for information on tissue function. Some organisms are genetically modified to express specific fluorescent markers.

1.2.1. DIFFRACTION

Because of its wave nature, light waves from different parts of a wavefront interfere causing light to diffract as it propagates through space and encounters obstacles [7]. Diffraction from an obstacle, such as a lens aperture, causes deviations from the classical straight ray model for light propagation that is shown in figure 1.2(a). A typical example of diffraction is the Gaussian beam shown in figure 1.2(b). A Gaussian beam is created from a flat wavefront with a Gaussian intensity profile. In contrast to the ray description of light given by geometrical optics, the Gaussian beam waist does not change linearly with propagation distance and the beam does not create an infinitely small spot in focus. Diffraction limits the resolution that can be obtained with most optical imaging systems.

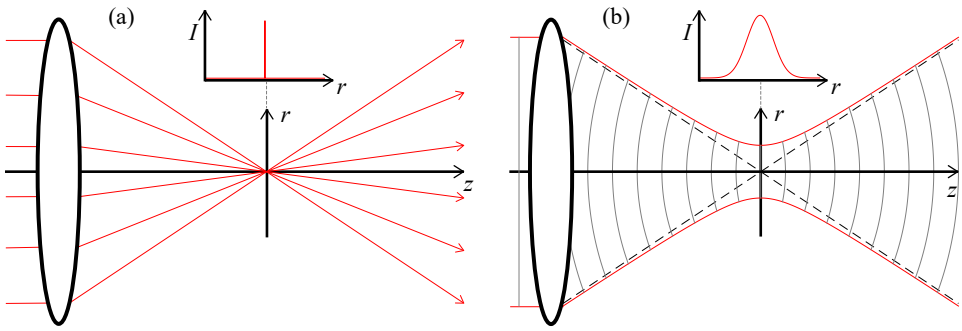

Figure 1.2: Evolution of a focused light beam along the propagation direction z according to a ray model (a), and for a Gaussian beam wave (b) showing curved wavefronts (gray). The insets show the beam intensity profiles in focus for the two models.

1.2.2. REFRACTION

Biological tissue exhibits structure and organization on a large set of length scales ranging from nanometers to meters. As a result, the refractive index of tissue also changes on all these length scales. Light refraction occurs wherever there are gradients in local

refractive index of an object. At small length scale this causes local phase changes, which causes the light to scatter. Variations in scattering lead to contrast in the reflected intensity for imaging techniques such as OCT. At larger length scales, refractive index gradients cause reflections, distortions, and aberrations that corrupt the images and degrade the image resolution. Hence most optical imaging techniques are restricted to shallow depths or thin objects. Larger scale variations in refractive index also can give rise to phase contrast, as demonstrated by several phase sensitive microscopy techniques [8]. Refractive index variation related to a change in tissue structure can be used as biomarkers for disease [9]. The degrading effects of refractive index variations on optical imaging are typically strong at object interfaces and can be reduced by matching the refractive index of the environment with that of the object using an immersion medium. However, index matching cannot correct for refractive index variations inside the sample. The refractive index variations inside the object can be chemically altered using optical clearing, as discussed in section 1.2.4. Alternatively, some techniques are able to correct some degree of refraction in the image reconstruction process [10, 11].

1.2.3. LIGHT ABSORPTION AND SCATTERING

As light propagates through materials it can be attenuated. The light can be taken out of the beam by absorption. Alternatively, the direction of the light can be changed due to scattering. Light attenuation by absorption and scattering is mathematically described by

$$I(z) = I(0)\exp(-\mu_t z), \tag{1.1}$$

where $I(z)$ is the intensity at depth z and μ_t is the total extinction coefficient. The extinction can be split into separate contributions of absorption μ_a and scattering μ_s, with $\mu_t = \mu_a + \mu_s$. The absorption spectra for some biological tissue constituents and typi-

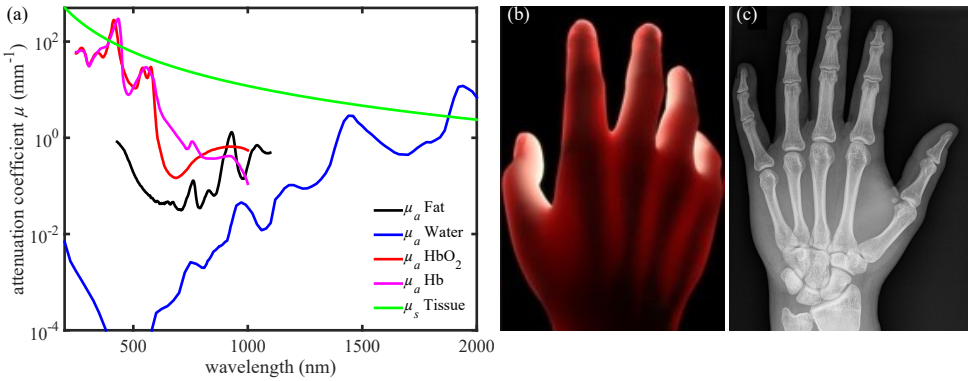

Figure 1.3: (a) Absorption spectra versus wavelength for several tissue constituents: Fat (black)[12], Water (blue)[13], oxy-hemoglobin (red), and deoxy-hemoglobin (magenta) http://omlc.org/spectra/hemoglobin/index.html. Typical wavelength dependence for tissue based on Mie scattering (green) [14]. (b) optical transmission image of a hand, (c) X-ray transmission image of a hand.

cal scattering coefficient of tissue are plotted in figure 1.3(a). For both X-ray and optical radiation water absorption has a similar magnitude. As can be seen, for most wave-

lengths, scattering is much stronger than the (water) absorption. However, since scattering is much weaker for X-ray radiation it is impossible to image bone in tissue with light whereas this is straightforward with X-ray, as shown in figure 1.3(b) and (c). For visible wavelengths tissue scatters typically less at longer wavelengths, as shown in figure 1.3(a). Therefore red light travels deeper through tissue than blue light, as is evident from the red glow in figure 1.3(b).

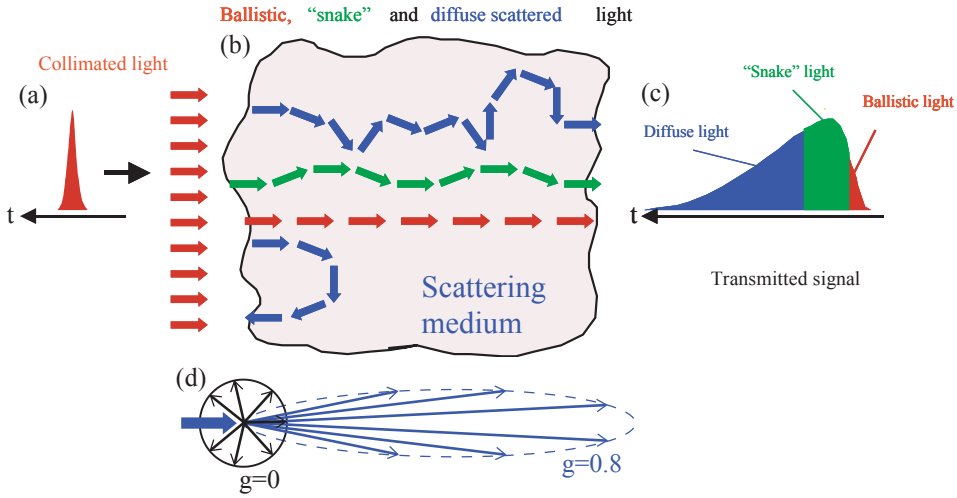

Figure 1.4: Schematic representation of a short light pulse (a) propagating in a scattering medium (b). Ballistic light (red) has not scattered an moves through the medium in a straight line. Snake photons (green) do scatter but still follow approximate straight paths though the sample. Diffuse photons (blue) have scattered many times and have completely random propagation directions in the sample. (c) Scattering causes the transmitted light to arrive at different times. (d) The probability distribution of the scattering angle is described by the phase function and the scattering anisotropy g. Images (a)-(c) taken from [1]

Light scattering is a result of small inhomogeneities of the refractive index of a material. In this section only elastic scattering is considered, hence the energy of the photon does not change. Scattering can be thought of as the change in propagation direction of a photon, as depicted in figure 1.4(b). In strongly scattering media, photons can undergo multiple scattering events while propagating though the material. The average distance between scattering events is called the scattering mean free path length l_s. The scattering coefficient $\mu_s = 1/l_s$ describes the average number of scattering events per distance travelled. The probability of a photon scattering a given angle with respect to its incoming direction is described by the scattering phase function $p(\theta)$ as shown in figure 1.4(d). Depending on their size, some particles scatter light isotropically in all directions, while others predominantly scatter in the forward direction. This behavior is described by the anisotropy factor $g = \langle \cos\theta \rangle$, the average cosine of the scattering angle. When g is large, light is mainly scattered in the forward direction, and maintains its original direction for long distances in the medium. Consequently, more light is transmitted though the sample even though it has been scattered.

Considering photons travelling through a slab of turbid (scattering and absorbing)

material shown in figure 1.3(b) several types of trajectories can be recognized. Some photons travel through the material without being scattered, these photons are referred to as ballistic photons. Some photons have scattered multiple times but still travel approximately straight through the material, these photons are referred to as snake photons. Other photons experience many scattering events and lose any correlation with their initial direction, these are the diffuse photons. Light scattering causes both spatial and temporal blurring of a light pulse, as shown in figure 1.4(c). The spatial blurring can be seen as a low pass filter that is responsible for the degradation of image resolution when imaging through turbid media.

1.2.4. OPTICAL IMAGING IN TURBID MEDIA

Scattering causes light rays to travel in complex paths through a scattering object. This makes imaging more difficult as detected photons have interacted with a larger volume, and localizing the origin of the measured signals is harder. Several techniques have been developed to address this problem and image in scattering media, like biological tissue, with high-resolution [1].

OPTICAL CLEARING

The scattering strength of a biological object can be reduced chemically using optical clearing. In optical clearing biological objects are made more transparent by replacing the water inside the object with a solution with higher refractive index [15]. This reduces the refractive index contrast between cellular structures and intracellular fluid, which, for large pieces of tissue, reduces the scattering coefficient of the tissue. Figure 1.5(a)-(c) shows ex-vivo optical clearing of 12 mm whole mouse brains and mouse embryos. Several clearing chemicals are used such as: benzyl alcohol-benzyl benzoate (BABB), glycerol, and ScaleA2 [15]. Optical clearing requires cumbersome and extensive chemical processing and can take up to several weeks to complete. Most optical clearing agents are compatible with fluorescence imaging, however, not compatible with in-vivo imaging. Cleared samples can be measured using many optical imaging techniques, including OPT [16] and OCT [17].

In-vivo imaging of glycerol optically cleared tissue has been performed, which has demonstrated an increase of the imaging depth by 33 – 46% in rat skin [15, 17]. Application of optical clearing for in-vivo imaging usually requires less than an hour but only gives modest imaging improvements. Also, both short and long term effects of optical clearing on living tissue are not known.

TIME GATING

The effect of scattering on an image can be suppressed by detecting only ballistic (non-scattered) photons. Ballistic photons travel in the shortest length straight path through the object, as shown in figure 1.4. Scattered photons travel a longer path through the sample and therefore have a later arrival time on the detector. The shorter the time window the detector is sensitive for recieving light, the stronger the scattered light can be suppressed. For micrometer resolution imaging in turbid media a time gate of 100 fs or smaller is typically required [1].

Time gated imaging of turbid media can be performed with electronically gated detection, enabling time gates of 200 ps to be reached [18]. Alternatively, a short pulsed

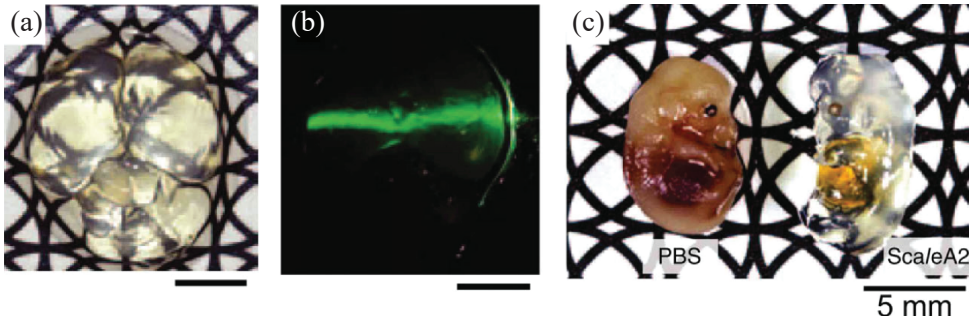

Figure 1.5: Optical clearing of a mouse brain (a) allows for improved light transmission though the tissue (b). (c) Mouse embryos cleared using two different clearing agents. Images taken from [15].

laser and a non-linear crystal can be used to select early arriving photons. In this case, light transmitted through the sample is combined with a reference pulse in a non-linear crystal. Subsequently, the light created through non-linear processes in the non-linear crystal is detected. As the light production in the non-linear crystal is only efficient at high light intensities, only photons that arrive at the non-linear crystal at the same time as the reference pulse will create a signal. The position of the time gate can be varied by adjusting the path length of the reference light. Using this technique, time gates of 100 fs can be reached, which allows time-resolved OPT imaging of non-cleared zebrafish [19].

SPATIAL FILTERING

Another approach to suppress scattered photons in the imaging process is to confine the spatial sensitive volume of the detector. Light scattering disperses photons in space. Therefore, by confining the sensitive volume of the detector, a significant part of the scattered photons can be prevented from hitting the detector. Confocal microscopy uses a pinhole to block scattered and out-of-focus light [20] and can reach imaging depths of $300-500$ μm [1]. A typical confocal microscope is depicted in Fig. 1.6(b). Lightsheet microscopy creates a spatial filter by illuminating only a confined sheet in the sample, with detection performed perpendicular to the sheet, as shown in Fig. 1.6(d). By only illuminating and imaging a single plane in the object at a time, the amount of light scattered from other parts of the object reaching the detector, is minimized [21, 22]. Multiphoton microscopy reduces the spatial volume from which light originates by using non-linear optical interaction. With this technique multiple photons are used to excite a single fluorescent probe [23]. Effectively this only happens at a narrow region around the focus of the excitation spot, confining the excitation volume of the system, as shown in Fig. 1.6(c). Moreover, for longer wavelength light the amount of scattering is reduced.

COHERENCE GATING AND POLARIZATION GATING

As light scatters in a material its polarization direction is changed. Hence, polarization gating can be used to preferentially select ballistic photons [24]. Moreover, it also makes light become less coherent. This effect also can be exploited to suppress the influence of scattered light on imaging turbid media. Typically the path length differences between ballistic and scattered photons are small so low-coherent light needs to be used to detect

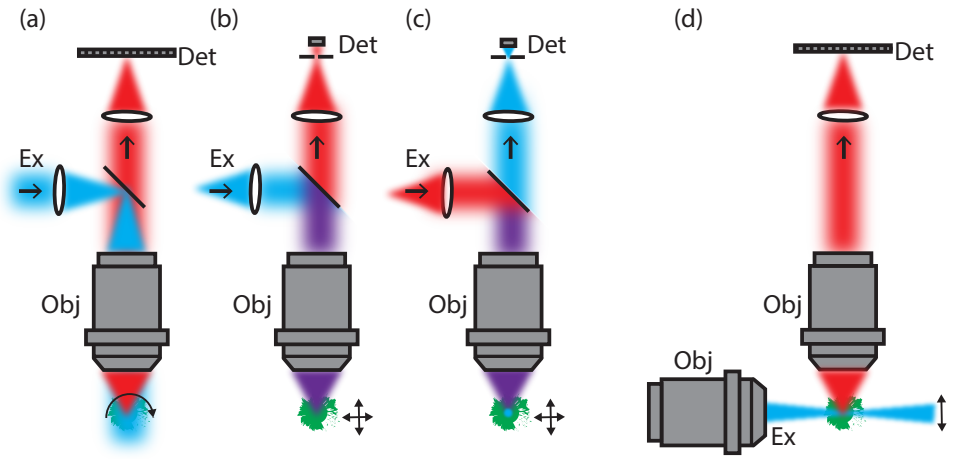

Figure 1.6: Schematic overview of various optical imaging systems. (a) OPT, widefield imaging with rotation of the object, (b) confocal microscopy, (c) multiphoton microscopy, and (d) light sheet microscopy. The arrows indicate the scanning motion needed to acquire images. Det: detector, Obj: Objective lens, and Ex: excitation light.

differences between coherence of ballistic and scattered light. By interference of light coming from a turbid sample with light from a reference beam, only light paths with path lengths smaller than the coherence length will contribute to the interference pattern [1]. OCT is an example of coherence gated reflection imaging [25]. In time-domain OCT a sample is illuminated with light from a low coherent source. Light backscattered from the sample is combined with a reference beam and only causes interference when the paths of the backscattered photons and the reference arm photons are equal to within the coherence length of the source. By scanning the length of the reference arm a depth profile can be constructed of the sample. In spectral-domain OCT the same interferometric setup is used but different wavelength components of the source are detected separately with a spectrometer or sequentially in time by scanning the wavelength of a narrowband source. A depth scan of the sample is calculated from the measured interference spectra that is obtained without scanning of the reference arm length. In most cases OCT combines coherence gating with confocal scanning in the lateral dimension. OCT typically has an imaging depth of 1-2 mm in tissue [26] and provides an axial resolution in the order of 1-20 µm. OCT is widely used in ophthalmology to inspect the condition of the layers in the human retina. Additionally, OCT has been used in a wide variety of applications such as in the field of industrial process control, forensics, and imaging cultural heritage.

WAVEFRONT SHAPING

As light travels through a scattering medium the wavefront is distorted by small variations of the refractive index. The path of the transmitted light can be reversed by sending back a phase conjugated beam (a beam with all phases reversed in amplitude). In a similar way an incident wavefront can be adapted and optimized for increased light transmission or even focusing using adaptive optics elements such as a spatial light modula-

tor or digital micro-mirror device [27, 28]. Wavefront shaping has been used for imaging through turbid media, for example, a spatial light modulator has been used for imaging behind a sample of 16 mean free pathlengths of light transport with microscopic resolution [29]. For imaging of turbid samples several approaches have been proposed including guidestar-based techniques [30]. Up till now wavefront shaping is not sufficiently fast for real-time deep tissue imaging [28].

DIFFUSE IMAGING

Instead of suppressing scattered light in the image formation, diffuse photons also can be used to create images. Diffuse optical tomography (DOT) measures diffuse light from a collection of source-detector configurations surrounding a sample. Images are reconstructed by numerical inversion of the diffusion equation. DOT is applied to $1-10$ cm sized samples, generally with a resolution of about $1/5$ the size of the object [1, 31]. Some implementations of DOT record time resolved data from many source-detector configurations. Time resolved measurements typically are performed using time-correlated single photon counting (TCSPC) or single photon avalanche diodes (SPADs) that provide a temporal resolution of about 200 ps [32, 33]. The measurement of the time resolved data and its use in the inversion provides an improved image quality. However, due to the strong blurring effect of the light diffusion through the sample high-resolution imaging is currently not feasible with DOT.

1.3. HIGH-RESOLUTION DEEP-TISSUE OPTICAL TRANSMISSION IMAGING

Of all the possible imaging geometries, transmission imaging allows for the highest number of ballistic photons to be detected. Reflection imaging techniques such as OCT and confocal microscopy have the advantage of easy optical access from a single direction and relatively straightforward image reconstruction. However, their penetration depth is limited compared to transmission imaging due to the double path travelled through the sample. Moreover, in case of reflection measurements the amount of detected reflected light is limited by the numerical aperture of the microscope. Despite these advantages, transmission images do not give direct 3D localization of the contrast sources. Therefore computed tomographic reconstruction techniques are required to create images. Next, several transmission based 3D optical imaging techniques are discussed.

1.3.1. OPTICAL PROJECTION TOMOGRAPHY

Optical projection tomography (OPT) is the optical equivalent of X-ray computed tomography (CT)[16]. Transmission or fluorescence images are recorded from several angles and reconstructed to create 3D images. As OPT is influenced by light scattering it is suitable for transparent samples, very small samples, or optically cleared tissue. In contrast to light sheet microscopy OPT can make absorption images.

A typical OPT setup is shown in Fig. 1.6(a) and resembles that of a widefield (fluorescence) microscope. Images of the sample are projected on a camera using an objective and tube lens. When used in fluorescence mode the sample is illuminated with an excitation source. In contrast to wide field microscopy, in OPT the sample is rotated during

acquisition of several camera images. The measured set of images is used to reconstruct 3D images of the sample using tomographic reconstruction techniques. To suppress the effect of light scattering on the image contrast typically optical clearing is used. For non-cleared tissue time gating has been applied to OPT to increase the imaging depth allowing for imaging of structures inside the tail of large non-cleared zebrafish [19].

TOMOGRAPHIC RECONSTRUCTION

In OPT, but also in other tomographic imaging techniques, the set of measured projections are used to reconstruct a 3D image of the object. OPT reconstruction is based on similar algorithms as used for X-ray CT. The basic principle of tomographic image reconstruction is demonstrated in 2D in Fig. 1.7. Fig. 1.7(a) shows a projection $p(\theta, t)$ created by some kind of interaction of a wave with the object along straight rays. This can be, for example, the attenuation of a light beam due to absorption or scattering, the accumulation of optical pathlength along a light path, or the accumulation of emitted light intensity along a line through a distribution of fluorescent molecules. Projections are then recorded for several angles θ, and are ordered into a sinogram, as shown in Fig. 1.7(b). Mathematically, the relation between the object $f(x, y)$ and the measured projections for straight ray propagation can be formulated with the Radon transform

$$p(\theta, t) = \int_{-\infty}^{\infty} \int_{-\infty}^{\infty} f(x, y)\delta(x\cos\theta + y\sin\theta - t)\mathrm{d}x\mathrm{d}y, \tag{1.2}$$

where the delta function describes a straight line through the object, parametrized by angle θ and lateral offset t, and (t, s) is the coordinate system in the detector frame of reference. The goal of computed tomography is to reconstruct the object $f(x, y)$ from the measurements $p(\theta, t)$.

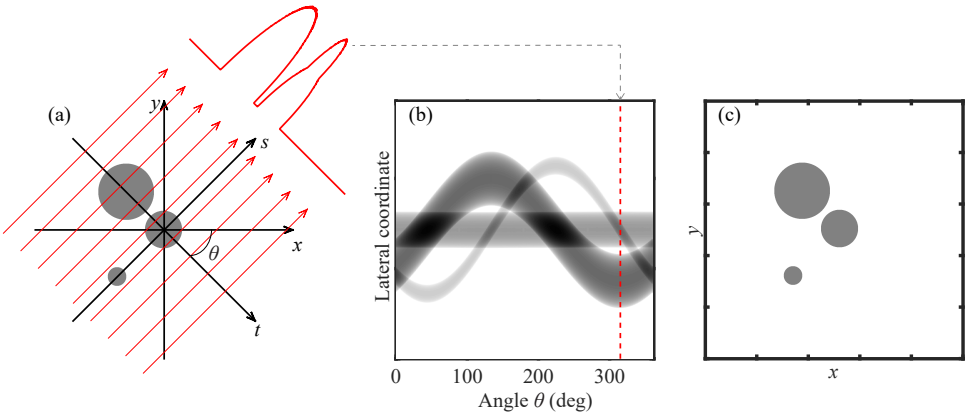

Figure 1.7: Schematic representation the principle of tomography. Projection images (a) are recorded of the sample from multiple angles and ordered in a sinogram (b) from which a tomographic image is reconstructed (c).

There are several techniques available for digitally reconstructing a tomographic image from sinogram data. One of these techniques is the inversion of the Radon trans-

form from Eq. (1.2) by using filtered back projection (FBP). The Fourier slice theorem states that the 1D Fourier transform of a projection equals a radial cross-section of the 2D Fourier transform of the object. The FBP algorithm combines the discretely measured data by filtering the projections in the Fourier domain and, after transformation back to the real domain, adding them in real space. FBP is very fast and works well with large datasets [34].

Another reconstruction approach is to find the object using optimization techniques. Algebraic reconstruction techniques approach the reconstruction problem as an inversion of a large system of linear equations

$$\mathbf{Af} = \mathbf{p}. \tag{1.3}$$

Here, each of the N_p projections is discretized with N_t pixels and stacked into a single vector $\mathbf{p}$ of size $N_t N_p$. The object is discretized on a grid with N_x and N_y pixels in x and y direction and also stacked into a single vector $\mathbf{f}$, with a size of $N_x N_y$. The geometry matrix $\mathbf{A}$ is a $N_t N_p$ by $N_x N_y$ sparse matrix describing the influence of the object on the detected signal.

This linear system of equations in Eq.(1.3.1) can be solved for $\mathbf{f}$ in various ways. The system of equations Eq.(1.3.1) is usually too large to invert directly but the equations can be solved iteratively. Many algorithms are available for this; here we will discuss several commonly used algorithms. The algebraic reconstruction technique (ART) iteratively solves the system of equations by updating the solution $\mathbf{f}$ based on each projection separately. Alternatively, simultaneous algebraic reconstruction technique (SART) updates the solution using a correction based on all the projections simultaneously. Optimization techniques such as the gradient descent method also can be used to compute the object that best matches the data.

$$\underset{\mathbf{f}}{\operatorname{argmin}} \quad \|\mathbf{A}\cdot\mathbf{f}-\mathbf{p}\|_2^2. \tag{1.4}$$

Algebraic reconstruction methods are very versatile as they can include the physics of the imaging process in the reconstruction and work well with non-uniformly sampled large data sets. Moreover, they can be adapted easily to include prior information by applying regularization or constraints in the reconstruction process [34].

DEPTH OF FIELD AND IMAGE RESOLUTION

The limited depth of field of optical imaging systems influences the image formation in OPT. As discussed in section 1.2.1, diffraction causes the light path to deviate from the straight ray, as shown in figure 1.8. Instead of sampling straight rays through the object, each pixel in a projection image is sensitive to a larger volume described by the optical point spread function (PSF) of the lens system. Consequently, the line integral approximation of Eq. 1.2 does not hold for optical tomography. Hence, when straight ray based reconstruction algorithms are applied, the images become blurred in the tangential direction, as shown in figure 1.9(b) and 1.9(c). The resolution in OPT images is related to the lateral resolution and depth of field of the lens system used in the setup. Several methods have been proposed to reduce the effects of diffraction in OPT. Experimentally,

depth of focus effects can be reduced by shifting the focus of the optical system and combining multiple datasets recorded at different focus positions [35–37]. Numerically, several filtering approaches and adapted reconstruction techniques have been developed [38–42].

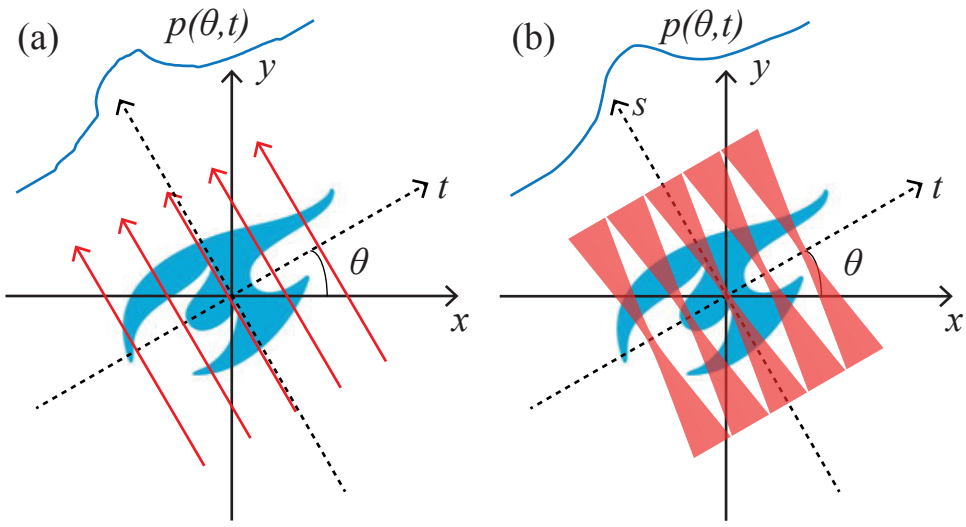

Figure 1.8: Generated projection with non-diffracted beams, like X-rays (a), and diffracting optical beams (b). Note that the projection in (b) is much smoother than in (a) due to the spatial averaging of the diffracting optical beam.

1.3.2. PHASE TOMOGRAPHY

Where OPT reconstructs absorption, scattering, or fluorescence images from a set of intensity images, tomographic images also can be created from the phase of light transmitted trough an object. Phase tomography is typically performed using holographic imaging to record the light field for each projection. The projections of the accumulated phase are extracted from the light field and the same reconstruction techniques as used in OPT are applied to reconstruct the refractive index map of the object. Phase tomography has been applied to various samples such as biological cells and small animals [43, 44]. Knowing the phase of the light makes it possible to incorporate diffraction effects in the tomographic reconstruction (this is known as optical diffraction tomography). In this case, the inversion process relies on approximations to the wave equation and reconstructs the refractive index distribution of the object. Diffraction tomography is limited to small transparent samples such as biological cells [45], transparent lenses [46] and photonic crystal fibers [47].

1.3.3. POINT SCANNING INTERFERENCE TOMOGRAPHIC IMAGING TECHNIQUES

Several imaging techniques have employed low coherence interferometry with point scanning in transmission for optical tomography. Although not always applied to scattering samples, these techniques combine confocal gating with coherence gating in the

1

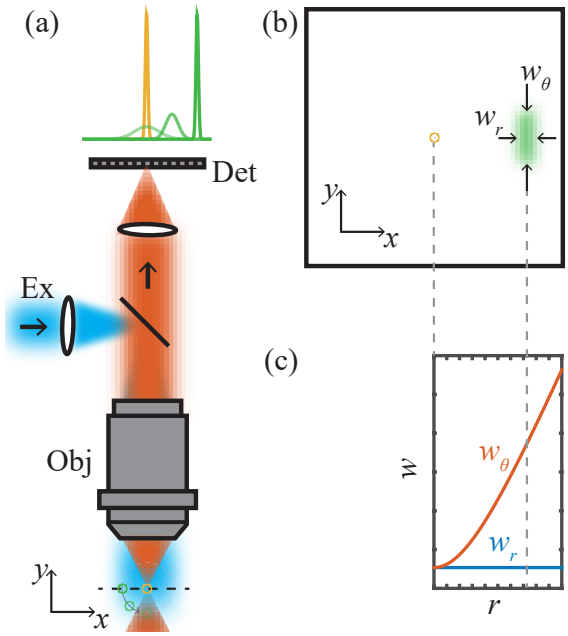

Figure 1.9: Schematic representation of the spatially dependent image resolution in optical tomography. (a) Basic OPT setup with two fluorescent points imaged for three angles. (b) The resulting reconstructed image shows blurring and elongation in the tangential direction. (c) The width of the image of a single point object in radial (blue) and tangential (red) directions as function of the radius from the center of rotation. Det: detector, Obj: Objective lens, Ex: excitation light.

imaging process. Time-domain OCT has been used in a double pass geometry and a mirror to reconstruct refractive index distributions of a transparent sample [48]. Later, spectral-domain OCT was used in transmission for imaging in scattering media [49]. In this case, absorption images were reconstructed by combining measurements from several lateral positions using a numerical inversion of radiative transport models. Transmission spectral-domain OCT has also been used to reconstruct the refractive index distribution of transparent samples using the optical path length difference of the two interferometer arms [50].

1.4. ZEBRAFISH AS A MODEL SYSTEM IN MEDICAL RESEARCH

Three dimensional imaging techniques are often applied to biological model systems such as cell cultures and small animals. Biological and medical sciences depend on the use of small animal models for studying disease origination, progression, and treatment. The results obtained for small animals are translated to the human biological system and followed by clinical trials on humans. Traditionally, mice have been the subject of many of these studies as mice are biologically very similar to humans. Over the past decades the use of Zebrafish (Danio rerio) has gained popularity. Zebrafish are tropical fresh-

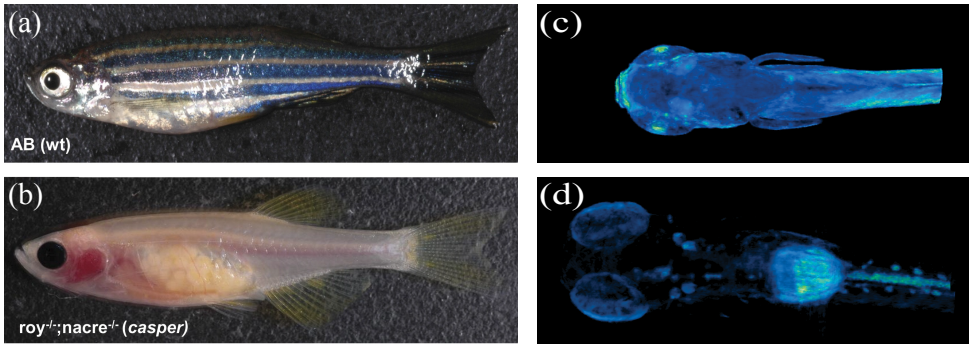

Figure 1.10: Examples of various types of zebrafish: (a) wild type, and (b) Casper zebrafish without pigment. Typical fluorescent OPT images of zebrafish larvae (c) and (d). Images (a) and (b) taken from [51].

water fish with a typical length as adults of approximately 40 mm. Zebrafish, shown in figure 1.10, are a convenient animal model as they are easy and cheap to keep, reproduce rapidly, and grow fast [52]. One of the main advantages of zebrafish for research purposes is the fact that the embryos and larvae are transparent, allowing for in-vivo optical access for inspection using microscopes. Currently, zebrafish are a well-established small animal model with many techniques available for handling, (genetic) manipulation, inspection, and classification. Numerous zebrafish models have been created for human diseases. In addition, many genetically modified species of zebrafish exist such as the Casper zebrafish that does not have any pigmentation [51], and zebrafish expressing fluorescent molecules upon the expression of a gene coding for a certain protein. There are many applications of zebrafish in biological and medical research such as drug discovery, toxicological screening [53], oncology research [54], regenerative medicine [55] and brain research [56]. Optical imaging is one of the primary tools in zebrafish

research using a variety of techniques such as: light sheet microscopy [22], OPT [57], and OCT [58]. In addition, systems have been developed for high-throughput imaging of zebrafish embryos and larvae [59].

1.5. THESIS CHALLENGES AND OUTLINE

The goal of this work is to develop techniques for 3D optical imaging of turbid media that provide high-resolution and high-contrast images. In this thesis the focus will be on imaging of adult zebrafish. Today, high-resolution in-vivo optical imaging of adult zebrafish is very challenging. In this context several challenges are addressed in this thesis. The first challenge is to perform optical imaging deep in tissue. Light scattering reduces the resolution in optical imaging of tissue, therefore strong suppression of scattered light is required. The second challenge is to create high-resolution images of relatively large objects. As shown in figure 1.1 the spatial resolution depends on the size of the sample. This is caused by several physical effects that originate from too much interaction of the information carrier with a sample, such as, wavefront aberrations, scattering, and absorption. Also diffraction, noise, radiation damage and hardware limitations can be limiting the resolution. The third challenge addressed in this thesis is providing adequate contrast. The first part of this thesis shows improvement in the OPT image quality of large objects. In the second part of this thesis the development of a new imaging modality named optical coherence projection tomography (OCPT) is presented. The thesis concludes with an outlook chapter.

CHAPTER 2: IMAGE RESOLUTION AND DECONVOLUTION IN OPTICAL TOMOGRAPHY

As the size of the measured objects becomes larger, the depth of field of the imaging system is a significant factor for the resolution in optical tomography. This chapter presents a model for the resolution in optical tomography images based on the properties of the imaging system used to measure the projections. Based on the developed theoretical framework, a deconvolution method is presented to correct for the spatially variant PSF in the tomographic images. Results are validated with OPT on fluorescent bead samples and illustrated using ex-vivo zebrafish measurements. This work improves the resolution of optical tomography imaging systems by correcting diffraction effects in the tomographic images and gives suggestions for optimal imaging system design. This chapter is based on the following publication:

> **J. van der Horst** and J. Kalkman, *Image resolution and deconvolution in optical tomography*, Optics Express, 24(21), 24460-24472, (2016).

CHAPTER 3: TRANSMISSION OPTICAL COHERENCE TOMOGRAPHY BASED MEASUREMENT OF OPTICAL MATERIAL PROPERTIES

This chapter discusses the development of Fourier-domain transmission OCT. A thorough theoretical analysis is presented of the measured signals and their relation to the material properties of the samples. The imaging system is described in detail and its performance is characterized. Finally, the capability of the system to quantitatively measure

the group refractive index, the group velocity dispersion, and the (wavelength dependent) total extinction coefficient is demonstrated with measurements using glass plates and various liquid samples. This work provides detailed knowledge about the modes of contrast that can be obtained in transmission and form the basis of OCPT, as described in chapter 4. This chapter is based on the following publication:

> A. K. Trull[1], **J. van der Horst**[1], J. G. Bijster, and J. Kalkman, *Transmission optical coherence tomography based measurement of optical material properties*, Optics Express, 23(26), 33550-33563, (2015).

CHAPTER 4: DEEP-TISSUE LABEL-FREE QUANTITATIVE TOMOGRAPHY

This chapter presents OCPT as a novel optical image modality. The deep-tissue imaging performance is quantified demonstrating a signal to noise ratio limited ballistic imaging depth of 27 mean free paths. A complete overview of the data acquisition and analysis is discussed. In addition, the performance of the OCPT machine is tested with phantoms and the 3D imaging resolution is quantified. The quantitative group refractive index and total extinction coefficient images are benchmarked with a set of scattering phantoms. Finally, OCPT is used for multimodal contrast imaging of an adult zebrafish. This chapter is based on the following publication:

> **J. van der Horst**, A. K. Trull, and J. Kalkman, *Deep-tissue label-free quantitative optical tomography*, Manuscript in preparation.

CHAPTER 5: OUTLOOK

This chapter summarizes the main results and presents future directions for research. The performance of the developed systems and techniques is compared to similar techniques. The limitations of the presented technology are discussed. Finally, some recommendations for further development of the tomographic systems and imaging in turbid media are given.

REFERENCES

[1] C. Dunsby and P. French, *Techniques for depth-resolved imaging through turbid media including coherence-gated imaging*, J. Phys. D **36**, R207 (2003).

[2] V. Ntziachristos, *Going deeper than microscopy: the optical imaging frontier in biology*, Nat. Methods **7**, 603 (2010).

[3] A. A. Appel, M. A. Anastasio, J. C. Larson, and E. M. Brey, *Imaging challenges in biomaterials and tissue engineering*, Biomaterials **34**, 6615 (2013).

[4] S. Manohar, A. van Apeldoorn, and W. Steenbergen, *Photoacoustic imaging: cells make themselves heard*, Nat. Photonics **9**, 216 (2015).

[1] These authors contributed equally to this work

[5] J. Yao and L. V. Wang, *Sensitivity of photoacoustic microscopy,* Photoacoustics **2**, 87 (2014).

[6] G. H. Karunamuni, S. Gu, M. R. Ford, L. M. Peterson, P. Ma, Y. T. Wang, A. M. Rollins, M. W. Jenkins, and M. Watanabe, *Capturing structure and function in an embryonic heart with biophotonic tools,* Front. Physiology **5**, 351 (2014).

[7] J. W. Goodman, *Introduction to Fourier optics* (Roberts and Company Publishers, 2005).

[8] C. Fang-Yen, W. Choi, Y. Sung, C. J. Holbrow, R. R. Dasari, and M. S. Feld, *Video-rate tomographic phase microscopy,* J. Biomed. Opt. **16**, 011005 (2011).

[9] Z. Wang, K. Tangella, A. Balla, and G. Popescu, *Tissue refractive index as marker of disease,* J. Biomed. Opt. **16**, 116017 (2011).

[10] M. A. Haidekker, *Optical transillumination tomography with tolerance against refraction mismatch,* Comput. Methods Programs Biomed. **80**, 225 (2005).

[11] S. J. Doran and D. N. Yatigammana, *Eliminating the need for refractive index matching in optical CT scanners for radiotherapy dosimetry: I. concept and simulations,* Phys. Med. Biol. **57**, 665 (2012).

[12] R. L. van Veen, H. Sterenborg, A. Pifferi, A. Torricelli, and R. Cubeddu, *Determination of VIS-NIR absorption coefficients of mammalian fat, with time-and spatially resolved diffuse reflectance and transmission spectroscopy,* in *Biomedical Topical Meeting* (Optical Society of America, 2004) p. SF4.

[13] G. M. Hale and M. R. Querry, *Optical constants of water in the 200-nm to 200-µm wavelength region,* Appl. Opt. **12**, 555 (1973).

[14] S. T. Flock, S. L. Jacques, B. C. Wilson, W. M. Star, and M. J. van Gemert, *Optical properties of Intralipid: a phantom medium for light propagation studies,* Lasers Surg. Med. **12**, 510 (1992).

[15] D. Zhu, K. V. Larin, Q. Luo, and V. V. Tuchin, *Recent progress in tissue optical clearing,* Laser & Photonics Rev. **7**, 732 (2013).

[16] J. Sharpe, U. Ahlgren, P. Perry, B. Hill, A. Ross, J. Hecksher-Sørensen, R. Baldock, and D. Davidson, *Optical projection tomography as a tool for 3D microscopy and gene expression studies,* Science **296**, 541 (2002).

[17] X. Wen, S. L. Jacques, V. V. Tuchin, and D. Zhu, *Enhanced optical clearing of skin in vivo and optical coherence tomography in-depth imaging,* J. Biomed. Opt. **17**, 0660221 (2012).

[18] G. M. Turner, G. Zacharakis, A. Soubret, J. Ripoll, and V. Ntziachristos, *Complete-angle projection diffuse optical tomography by use of early photons,* Opt. Lett. **30**, 409 (2005).

[19] L. Fieramonti, A. Bassi, E. A. Foglia, A. Pistocchi, C. D'Andrea, G. Valentini, R. Cubeddu, S. De Silvestri, G. Cerullo, and F. Cotelli, *Time-gated optical projection tomography allows visualization of adult zebrafish internal structures,* PLoS One **7**, e50744 (2012).

[20] J. Schmitt, A. Knüttel, and M. Yadlowsky, *Confocal microscopy in turbid media,* J. Opt. Soc. Am. **11**, 2226 (1994).

[21] J. Huisken, J. Swoger, F. Del Bene, J. Wittbrodt, and E. H. Stelzer, *Optical sectioning deep inside live embryos by selective plane illumination microscopy,* Science **305**, 1007 (2004).

[22] P. J. Keller, A. D. Schmidt, J. Wittbrodt, and E. H. Stelzer, *Reconstruction of zebrafish early embryonic development by scanned light sheet microscopy,* Science **322**, 1065 (2008).

[23] W. R. Zipfel, R. M. Williams, and W. W. Webb, *Nonlinear magic: multiphoton microscopy in the biosciences,* Nat. Biotechnol. **21**, 1369 (2003).

[24] S. Demos and R. Alfano, *Temporal gating in highly scattering media by the degree of optical polarization,* Opt. Lett. **21**, 161 (1996).

[25] J. A. Izatt, E. A. Swanson, J. G. Fujimoto, M. R. Hee, and G. M. Owen, *Optical coherence microscopy in scattering media,* Opt. Lett. **19**, 590 (1994).

[26] V. Kodach, J. Kalkman, D. Faber, and T. G. van Leeuwen, *Quantitative comparison of the OCT imaging depth at 1300 nm and 1600 nm,* Biomed. Opt. Express **1**, 176 (2010).

[27] I. M. Vellekoop and A. Mosk, *Focusing coherent light through opaque strongly scattering media,* Opt. Lett. **32**, 2309 (2007).

[28] A. P. Mosk, A. Lagendijk, G. Lerosey, and M. Fink, *Controlling waves in space and time for imaging and focusing in complex media,* Nat. Photonics **6**, 283 (2012).

[29] I. M. Vellekoop and C. M. Aegerter, *Scattered light fluorescence microscopy: imaging through turbid layers,* Opt. Lett. **35**, 1245 (2010).

[30] R. Horstmeyer, H. Ruan, and C. Yang, *Guidestar-assisted wavefront-shaping methods for focusing light into biological tissue,* Nat. Photonics **9**, 563 (2015).

[31] D. A. Boas, D. H. Brooks, E. L. Miller, C. A. DiMarzio, M. Kilmer, R. J. Gaudette, and Q. Zhang, *Imaging the body with diffuse optical tomography,* IEEE Signal Process. Mag. **18**, 57 (2001).

[32] Y. Bérubé-Lauzière, M. Crotti, S. Boucher, S. Ettehadi, J. Pichette, and I. Rech, *Prospects on time-domain diffuse optical tomography based on time-correlated single photon counting for small animal imaging,* J. Spectroscopy (2016).

[33] W. Becker, A. Bergmann, A. Gibson, N. Everdell, D. Jennions, M. Schweiger, S. Arridge, and J. C. Hebden, *Multi-dimensional time-correlated single photon counting applied to diffuse optical tomography,* in *Proc. SPIE*, Vol. 5693 (2005) pp. 34–42.

[34] A. C. Kak and M. Slaney, *Principles of computerized tomographic imaging* (SIAM, 2001).

[35] J. Sharpe, *Optical projection tomography,* Annu. Rev. Biomed. Eng. **6**, 209 (2004).

[36] L. Chen, N. Andrews, S. Kumar, P. Frankel, J. McGinty, and P. M. French, *Simultaneous angular multiplexing optical projection tomography at shifted focal planes,* Opt. Lett. **38**, 851 (2013).

[37] Q. Miao, J. Hayenga, M. G. Meyer, T. Neumann, A. C. Nelson, and E. J. Seibel, *Resolution improvement in optical projection tomography by the focal scanning method,* Opt. Lett. **35**, 3363 (2010).

[38] W. Xia, R. M. Lewitt, and P. R. Edholm, *Fourier correction for spatially variant collimator blurring in SPECT,* IEEE Transactions on Medical Imaging **14**, 100 (1995).

[39] J. R. Walls, J. G. Sled, J. Sharpe, and R. M. Henkelman, *Resolution improvement in emission optical projection tomography,* Phys. Med. Biol. **52**, 2775 (2007).

[40] A. Darrell, H. Meyer, K. Marias, M. Brady, and J. Ripoll, *Weighted filtered backprojection for quantitative fluorescence optical projection tomography,* Phys. Med. Biol. **53**, 3863 (2008).

[41] L. Chen, J. McGinty, H. B. Taylor, L. Bugeon, J. R. Lamb, M. J. Dallman, and P. M. French, *Incorporation of an experimentally determined mtf for spatial frequency filtering and deconvolution during optical projection tomography reconstruction,* Opt. Express **20**, 7323 (2012).

[42] C. M. McErlean, E. Bräuer-Krisch, J. Adamovics, and S. J. Doran, *Assessment of optical CT as a future QA tool for synchrotron X-ray microbeam therapy,* Phys. Med. Biol. **61**, 320 (2015).

[43] W. Choi, C. Fang-Yen, K. Badizadegan, S. Oh, N. Lue, R. R. Dasari, and M. S. Feld, *Tomographic phase microscopy,* Nat. Methods **4**, 717 (2007).

[44] A. Kuś, M. Dudek, B. Kemper, M. Kujawińska, and A. Vollmer, *Tomographic phase microscopy of living three-dimensional cell cultures,* J. Biomed. Opt. **19**, 046009 (2014).

[45] Y. Sung, W. Choi, C. Fang-Yen, K. Badizadegan, R. R. Dasari, and M. S. Feld, *Optical diffraction tomography for high resolution live cell imaging,* Opt. Express **17**, 266 (2009).

[46] K. Kim, J. Yoon, and Y. Park, *Large-scale optical diffraction tomography for inspection of optical plastic lenses,* Opt. Lett. **41**, 934 (2016).

[47] W. Gorski and W. Osten, *Tomographic imaging of photonic crystal fibers,* Opt. Lett. **32**, 1977 (2007).

[48] A. M. Zysk, J. J. Reynolds, D. L. Marks, P. S. Carney, and S. A. Boppart, *Projected index computed tomography,* Opt. Lett. **28**, 701 (2003).

[49] L. Li and L. V. Wang, *Optical coherence computed tomography,* Appl. Phys. Lett. **91**, 141107 (2007).

[50] Y. Wang and R. K. Wang, *High-resolution computed tomography of refractive index distribution by transillumination low-coherence interferometry,* Opt. Lett. **35**, 91 (2010).

[51] R. M. White, A. Sessa, C. Burke, T. Bowman, J. LeBlanc, C. Ceol, C. Bourque, M. Dovey, W. Goessling, C. E. Burns, *et al.*, *Transparent adult zebrafish as a tool for in vivo transplantation analysis,* Cell Stem Cell **2**, 183 (2008).

[52] G. J. Lieschke and P. D. Currie, *Animal models of human disease: zebrafish swim into view,* Nat. Rev. Genet. **8**, 353 (2007).

[53] R. T. Peterson and C. A. MacRae, *Systematic approaches to toxicology in the zebrafish,* Annu. Rev. Pharmacol. Toxicol. **52**, 433 (2012).

[54] R. White, K. Rose, and L. Zon, *Zebrafish cancer: the state of the art and the path forward,* Nat. Rev. Cancer **13**, 624 (2013).

[55] K. D. Poss, L. G. Wilson, and M. T. Keating, *Heart regeneration in zebrafish,* Science **298**, 2188 (2002).

[56] T. J. van Ham, C. A. Brady, R. D. Kalicharan, N. Oosterhof, J. Kuipers, A. Veenstra-Algra, K. A. Sjollema, R. T. Peterson, H. H. Kampinga, and B. N. Giepmans, *Intravital correlated microscopy reveals differential macrophage and microglial dynamics during resolution of neuroinflammation,* Dis. Models Mech. **7**, 857 (2014).

[57] J. McGinty, H. B. Taylor, L. Chen, L. Bugeon, J. R. Lamb, M. J. Dallman, and P. M. French, *In vivo fluorescence lifetime optical projection tomography,* Biomed. Opt. Express **2**, 1340 (2011).

[58] K. D. Rao, A. Alex, Y. Verma, S. Thampi, and P. K. Gupta, *Real-time in vivo imaging of adult zebrafish brain using optical coherence tomography,* J. of Biophotonics **2**, 288 (2009).

[59] C. Pardo-Martin, T.-Y. Chang, B. K. Koo, C. L. Gilleland, S. C. Wasserman, and M. F. Yanik, *High-throughput in vivo vertebrate screening,* Nat. Methods **7**, 634 (2010).

2

IMAGE RESOLUTION AND DECONVOLUTION IN OPTICAL TOMOGRAPHY

This chapter is based on the following publication:
J. van der Horst and J. Kalkman, *Image resolution and deconvolution in optical tomography*, Optics Express, 24(21), 24460-24472, (2016).

ABSTRACT

We present a frequency domain analysis of the image resolution of optical tomography systems. The result of our analysis is a description of the spatially-variant resolution in optical tomographic image after reconstruction as a function of the properties of the imaging system geometry. We validate our model using optical projection tomography (OPT) measurements of fluorescent beads embedded in agarose gel. Our model correctly describes both the radial and tangential resolution of the measured images. In addition, we present a correction of the tomographic images for the spatially-varying resolution using a deconvolution algorithm. The resulting corrected tomographic reconstruction shows a homogeneous and isotropic pixel-limited resolution across the entire image. Our method is applied to OPT measurements of a zebrafish, showing improved resolution. Aside from allowing image correction and providing a resolution measure for OPT systems, our model provides a powerful tool for the design of optical tomographic systems.

2.1. INTRODUCTION

Three dimensional imaging of cells and small animals is of great importance in the biological and medical sciences as our knowledge on human diseases is based on the structure and function of cells and organisms. Optical techniques can provide cost effective, high-resolution, 3D images of the structure of cells and small animals. In addition, by using labelled molecules, fluorescence imaging can give information about the function of cells and tissue.

Currently, several optical techniques are used for whole cell and small animal imaging. Microscopy is a tool for imaging live cells. Light sheet microscopy uses a light illumination sheet and images the emission from perpendicular to the sheet. It is used for imaging sub-millimeter sized samples [1]. 3D imaging studies of millimeter sized samples have used optical projection tomography (OPT) [2]. OPT measures projections of transmission or emission and reconstructs the object from the projections. OPT is used for imaging small animals such as zebrafish and mouse embryos, whole organs taken from adult mice, and plant tissue. It can be used in-vivo, or ex-vivo in combination with optical clearing techniques that suppress light scattering. OPT has the advantage of being able to create 3D images in both transmission and fluorescent modes, hence OPT is useful to study gene expression, tissue morphology and locations of fluorescently labelled tissues. In transmission mode, OPT resembles X-ray CT, in fluorescent mode, OPT is more similar to single-photon emission computed tomography (SPECT) imaging. In both cases optical radiation is used instead of X-rays or gamma quanta.

In contrast to X-ray CT and SPECT imaging, the use of visible light in OPT allows for the use of lenses to relay and magnify the projection images and achieve micrometer spatial resolution. A drawback of the use of lenses is the limited depth sensitivity, related to the finite depth of field of the optical imaging system. Generally, the resolution of the images is inversely proportional to the numerical aperture (NA) of the collecting lens. However, high NA lenses have a small depth of field, meaning that objects are only in focus in a small region around the focal plane. Using high NA lenses in OPT causes some parts of the sample to have a high resolution in a projection, while other parts are out of focus and have a low resolution.

Several studies have identified this problem and proposed methods to reduce its effect. The depth of focus can be extended by focusing on a plane between the center of rotation and the edge of the sample and recording projections over the full range of 360°[3]. Alternatively, data from multiple focal planes can be combined by either simultaneous measurement [4] or scanning of the lens focus through the object [5]. While recording data from multiple focal planes solves the issue of the depth of field, the increased number of measurements requires longer acquisition times and increased complexity of the OPT system.

Several numerical approaches have been proposed to correct for resolution blurring in OPT. Based on the frequency distance relationship (FDR) [6], OPT tomograms can be corrected for the out of focus deterioration of resolution [7]. The effects of the axial intensity distribution and defocus on the point spread function (PSF) can also be compensated by using a weighted filtered backprojection [8]. More recently, the full modulation transfer function (MTF) of the imaging optics was included as an additional filter in the filtered backprojection process [9]. While obtaining a significant reduction in image

background and artefacts using an MTF mask, the MTF correction with deconvolution did not fully correct for the tangential blurring observed in the system. McErlean et al. [10] investigated a possible spatial resolution improvement by image deconvolution with an experimentally determined PSF. However, they used a spatially-invariant PSF thereby obtaining less than optimum resolution.

The aim of this study is to quantify the effect of the imaging optics on the reconstructed images in optical tomography. In the first section we quantify this effect using a frequency domain analysis of the image resolution in a single projection and in the reconstructed tomographic image. In the second section we propose and verify our model for the spatially-variant resolution of the tomographic imaging system using OPT measurements of a sample consisting of fluorescent beads. Then, we use the derived point spread function to deconvolute the reconstructed image. A close to pixel-limited resolution after image deconvolution is demonstrated for the fluorescent bead sample. We also apply our method to a zebrafish sample. Finally, our results, and their implications for optical tomography, are discussed.

2.2. THEORY

In an optical tomography system, the spatially-variant PSF is directly related to the PSF of the imaging system that makes every projection. Here we use a Fourier optics description of the PSF of the imaging system to derive the PSF of the tomography system. Our analysis is demonstrated for fluorescence tomography, but is equally valid for transmission optical tomography.

2.2.1. IMAGE FORMATION OF A SINGLE PROJECTION

Consider an object with fluorescence distribution $f(t,s,z)$. In fluorescent tomography the light emitted by the object is focused onto a 2D detector to create projections of the object, as shown in Fig. 2.1. We assume that all fluorophores are excited at the same rate and emit isotropically. In addition, it is assumed that any emitted fluorescence can reach the detector unimpeded. Hence, effects of reabsorption, light attenuation and refraction of fluorescent light are not taken into account. The intensity in the image space is described by a convolution of the object function, $f(t,s,z)$, with the incoherent PSF of the imaging optics $|h(t,s,z)|^2$, where $h(t,s,z)$ describes the coherent PSF of the imaging system [11]. The system images the plane $s=0$ in object space onto the plane $s'=0$ in image space. The intensity distribution in image space $p(t',s',z')$ is given by a 3D convolution with the PSF

$$p(t',s',z') = f(t,s,z) \otimes |h(t,s,z)|^2 . \tag{2.1}$$

If a detector is placed in the focal plane $s'=0$, the intensity distribution on the detector is

$$p(t',z') = \int_{-\infty}^{\infty}\int_{-\infty}^{\infty}\int_{-\infty}^{\infty} f(t'-t,s'-s,z'-z)|h(t,s,z)|^2 \mathrm{d}t\mathrm{d}s\mathrm{d}z \Bigg|_{s'=0} . \tag{2.2}$$

This equation shows the main difference between OPT and straight ray based tomography. If $|h(t,s,z)|^2 = \delta(t,z)$ equation 2.2 reduces to the line integral along s for the intensity of a single point in the projection. OPT deviates from straight ray based tomography

as the measured projection points do not only sample a straight line from the source to the detector, but instead sample a complex volume of the object, described by the PSF $|h(t,s,z)|^2$.

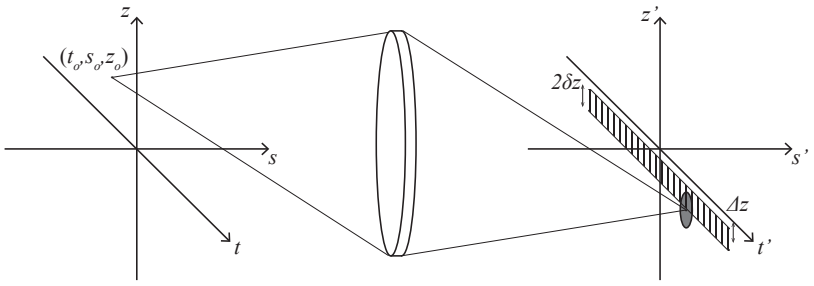

Figure 2.1: Schematic representation of the lens imaging system for the detection of a single projection

2.2.2. TOMOGRAPHIC POINT SPREAD FUNCTION

In tomographic imaging a collection of projections, acquired at different angles θ are used to construct a tomographic image of the object. Figure 2.2(a) shows a top view of the object plane with the coordinate systems used in the derivation. In the following analysis we assume that the rotation axis coincides with the z-axis, i.e., the rotation axis is in the focal plane, and the detector is positioned at $s' = 0$. In the reference frame of the detector (t', s', z'), a projection p at angle θ is given by Eq. (2.2). If the projection is taken at angle θ, this is equivalent to a rotation of the object f through angle $-\theta$. The relation between the object coordinates in the rotating frame (x, y, z) and the stationary (detector) frame of reference (t, s, z) is given by

$$\begin{bmatrix} t \\ s \\ z \end{bmatrix} = \begin{bmatrix} \cos(-\theta) & -\sin(-\theta) & 0 \\ \sin(-\theta) & \cos(-\theta) & 0 \\ 0 & 0 & 1 \end{bmatrix} \begin{bmatrix} x \\ y \\ z \end{bmatrix}. \tag{2.3}$$

The resolution of the tomographic imaging system is calculated by determining the response to a point object function, i.e., $f(x,y,z) = \delta(x - x_o, y - y_o, z - z_o) = \delta(t - t_o, s - s_o, z - z_o)$, as shown in Fig. 2.2(a). Without loss of generality we assume the point object to be placed in the plane $z_o = 0$ hence the PSF from Eq. (2.2) is

$$p(\theta, t', z') = |h(t' - t_o, -s_o, z')|^2. \tag{2.4}$$

Every individual horizontal slice of the object is reconstructed from horizontal sections of all the 2D projections. These horizontal sections correspond to one or several rows of detector pixels at the corresponding vertical position of the slice.

$$p(\theta, t') = \int_{\Delta z - \delta z}^{\Delta z + \delta z} |h(t' - t_o, s_o, z)|^2 \mathrm{d}z, \tag{2.5}$$

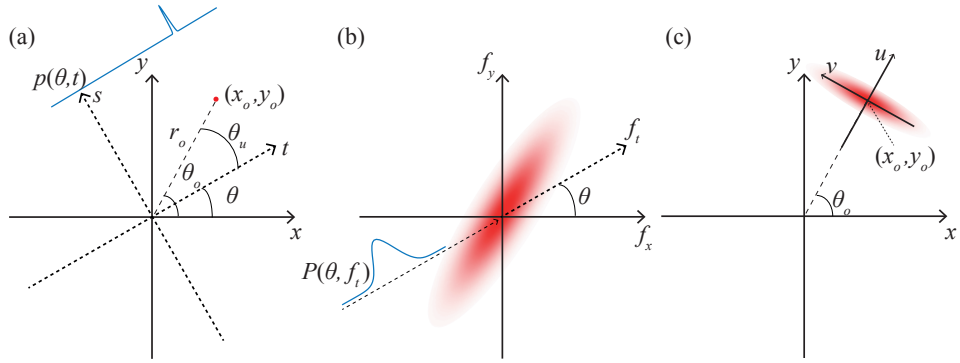

Figure 2.2: (a) Schematic representation of the coordinate systems in the object and camera frames of reference. The point object is represented by coordinates (x_o, y_o), (b) Frequency domain representation of the reconstructed image for a point object. The frequency content is composed of the frequency content of the individual projections, as indicated for a single projection at angle θ. (c) Reconstructed image resulting from a point object

with Δz the vertical distance between the point source and the slice, and $2\delta z$ the slice thickness. The set of all 1D projections is called a sinogram.

To obtain the frequency description of the projection we take the Fourier transform of Eq. (2.5) along the transverse coordinate t, to obtain

$$P(\theta, f_t) = \mathscr{F}\{p(\theta, t')\}. \tag{2.6}$$

Assuming a parallel-beam geometry the projection slice theorem states that the 2D Fourier transform of the image of the object, denoted with $OTF(f_x, f_y)$, is composed of the frequency content of the projections $P(\theta, f_t)$ [12]. Each projection $P(\theta, f_t)$ forms the radial cross-section of $OTF(f_x, f_y)$ at angle θ, as shown in Fig. 2.2(b). The OTF is calculated from Eq. (2.6) by substitution of

$$s_o = s_o(\theta) = r_o \sin(\theta_o - \theta), \tag{2.7}$$

$$\theta = \tan^{-1}\left(\frac{f_y}{f_x}\right), \tag{2.8}$$

$$r_o^2 = x_o^2 + y_o^2, \tag{2.9}$$

and

$$f_t = \sqrt{f_x^2 + f_y^2}. \tag{2.10}$$

Subsequent 2D inverse Fourier transform of $OTF(f_x, f_y)$ yields the position dependent PSF, as illustrated in Fig. 2.2(c).

GAUSSIAN BEAM PSF

The PSF of the tomographic imaging system can be calculated from the PSF of the imaging optics $|h(t, s, z)|^2$. In general, $|h(t, s, z)|^2$ can have a complicated shape. Here, we

assume the imaging PSF is a focused Gaussian beam described by

$$|h(t,s,z)|^2 = \frac{2}{\pi w^2(s)} \exp\left(-\frac{2(t^2+z^2)}{w^2(s)}\right), \tag{2.11}$$

where $w(s)$ is the beam waist, given by

$$w(s) = \sqrt{w_0^2 + \frac{\lambda^2 s^2}{\pi^2 w_0^2}}, \tag{2.12}$$

with λ the emission wavelength of the fluorophore and w_0 the Gaussian beam waist defined as the e^{-1} value of the field amplitude in focus [13]. Substituting Eq. (4.4) into Eq. (2.5) and performing the integration in the z direction over the height of the detector row results in

$$p(\theta, t') = \sqrt{2\pi} \frac{A(\theta)}{\pi w^2(s_o(\theta))} \exp\left(-\frac{2[t'-t_o]^2}{w^2(s_o(\theta))}\right), \tag{2.13}$$

with

$$A(\theta) = \frac{1}{2}\left[\mathrm{erf}\left(\frac{\sqrt{2}}{w^2(s_o(\theta))}(\Delta z + \delta z)\right) - \mathrm{erf}\left(\frac{\sqrt{2}}{w^2(s_o(\theta))}(\Delta z - \delta z)\right)\right]. \tag{2.14}$$

Fourier transformation in the transversal t' direction gives

$$P(\theta, f_t) = A(\theta) \exp\left(-\frac{\pi^2 w^2(s_o(\theta)) f_t^2}{2}\right) \exp\left(-2\pi i\, t_o f_t\right). \tag{2.15}$$

When the slice is thick with respect to the spot size of the point source on the detector, we can take the limit $\delta z \longrightarrow \infty$, resulting in $A(\theta) \longrightarrow 1$. Using the relations (2.7)-(2.10), the OTF of the tomographic system is

$$OTF(f_x, f_y) = \exp\left(-\frac{\pi^2(f_x^2+f_y^2)}{2}\left[w_0^2 + \frac{\lambda^2 r_o^2 \sin^2(\theta_o - \theta)}{\pi^2 w_0^2}\right]\right) \exp\left(-2\pi i \left(x_o f_x + y_o f_y\right)\right) \tag{2.16}$$

The last exponential term in Eq. (2.16) is a phase term resulting from the shift of the point object (x_o, y_o) in real space. Equation (2.16) can be simplified by introducing a shifted and rotated coordinate system (u, v), where u and v respectively represent the radial and tangential directions in the reconstructed image, as shown in Fig. 2.2(c) and given by

$$\begin{bmatrix} u \\ v \end{bmatrix} = \begin{bmatrix} \cos(-\theta_o) & -\sin(-\theta_o) \\ \sin(-\theta_o) & \cos(-\theta_o) \end{bmatrix} \begin{bmatrix} x - x_o \\ y - y_o \end{bmatrix}, \tag{2.17}$$

with the frequency domain counterpart (f_u, f_v). This centers the point source on the origin in the real domain and removes the Fourier-shift term in the OTF, giving

$$OTF(f_u, f_v) = \exp\left(-\frac{1}{2}\pi^2(f_u^2+f_v^2)\left[w_0^2 + \frac{\lambda^2}{\pi^2 w_0^2}\left(r_o^2 \sin^2(\theta_u)\right)\right]\right), \tag{2.18}$$

where $\theta_u = \theta_o - \theta$ now denotes the angle with the u axis. Further simplification using $\sin^2(\theta_u) = \frac{v^2}{u^2+v^2} = \frac{f_v^2}{f_u^2+f_v^2}$ reduces the expression to

$$OTF(f_u, f_v) = \exp\left(-\frac{1}{2}\pi^2\left[(f_u^2 + f_v^2)\,w_0^2 + \frac{\lambda^2}{\pi^2 w_0^2}\left(r_o^2 f_v^2\right)\right]\right), \tag{2.19}$$

Equation (2.19) is separable into two factors with dependence on u and v only, and is further simplified to

$$OTF(f_u, f_v) = \frac{1}{2\pi w_0^2}\exp\left(-\pi^2\left(f_u^2 a_u + f_v^2 a_v\right)\right), \tag{2.20}$$

with $a_u = w_0^2/2$ and $a_v = \left(w_0^2 + \frac{\lambda^2 r_o^2}{\pi^2 w_0^2}\right)/2 = w^2(r_o)/2$. Taking the inverse Fourier transform of Eq. (2.20) we obtain the PSF of the tomographic imaging system

$$PSF(u, v) = \sqrt{\frac{1}{\pi^2 a_u a_v}}\exp\left(-\left[\frac{u^2}{a_u} + \frac{v^2}{a_v}\right]\right), \tag{2.21}$$

which is the main theoretical result of this section. Figure 2.3(a) shows the modelled optical tomography PSF at several positions in the reconstructed image. The example

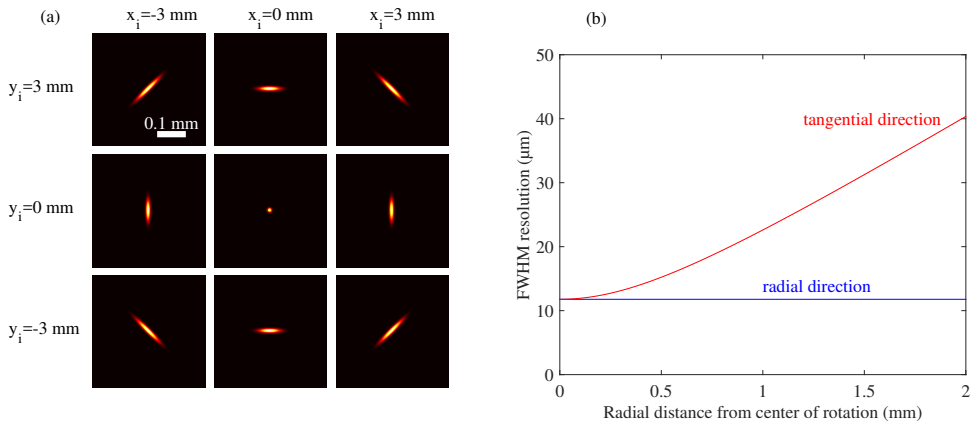

Figure 2.3: (a) Effect of the PSF on the tomographic image for point sources located at various positions (x_o, y_o), indicated at the top and right. (b) Theoretical FWHM resolution in the radial and tangential direction as function of the radial distance from the center of rotation.

is calculated with $w_0 = 10$ μm and $\lambda = 515$ nm. The PSF in the center of the image is isotropic and has a width w_0 in all directions. The effect of the lens system PSF away from the center results in a radial resolution of w_0 independent of radial position, however the tangential resolution deteriorates as the radial position of the object increases. Figure 2.3(b) shows a quantification of this effect as the tangential FWHM increases with the radial distance from the center.

2.3. METHODS

2.3.1. EXPERIMENTAL SETUP

A schematic of the fluorescence OPT setup is shown in Fig. 4.2. A collimated beam of light with a wavelength of 488 nm is created using an Argon laser (150m Select, Laser Physics). The output power of the laser is adjusted using a neutral density filter wheel (NDC-100C04M, Thorlabs). The beam is expanded with a 4f lens system consisting of two lenses with a focal length of 10 mm (LB1157, Thorlabs), and 1000 mm (LB1859, Thorlabs). The sample is placed in a cuvette (Hellma, HELL704001-30-10) with inner dimensions 30×30×30 mm (length × width × height). After passing through a color filter, the fluorescent light is detected using a camera (ORCA-ER, Hamamatsu) with an imaging lens assembly (Optem Fusion, Qioptic). The imaging lens assembly consist of a 1.67× objective lens (35-00-04-000, Qioptic) and a 1.0× tube lens (35-08-06-000, Qioptic). The numerical aperture of the lens assembly can be adjusted using an adjustable aperture stop (35-07-25-000, Qioptic) placed between the objective and the tube lens. The sample is mounted on a stage assembly to perform x, y and z translation (8MT167M-25LS, Standa) as well as a θ rotation (8MR151, Standa). An $x-y$ translation mount (SCP05, Thorlabs), and a tip-tilt mount (KC05-T/M, Thorlabs) enable fine tuning of the position of the rotation axis and the sample. The agarose sample is attached to the lower end of the tip-tilt mount using a custom metal cylinder and glue.

A total of 360 projections are recorded at 1° intervals. Measurements are performed with a camera integration time of 5.0 seconds and a laser output power of 28.13 mW. The measurement time of a complete sinogram is approximately 35 minutes.

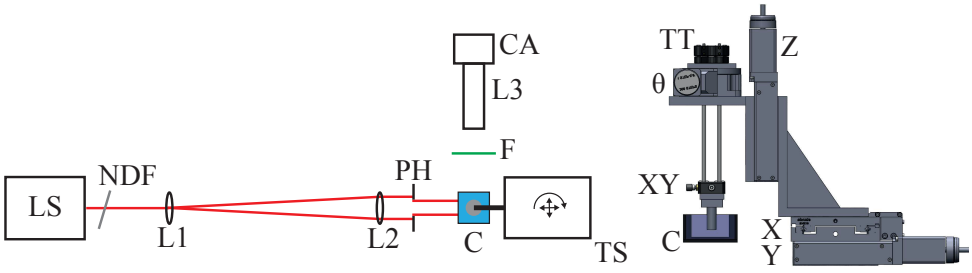

Figure 2.4: Schematic representation of the experimental OPT setup. LS: Light source, NDF: neutral density filter, PH: pinhole, C: cuvette, TS: translation stage assembly, F: filter, L1 L2 and L3 Lenses, CA, camera, XY: manual x and y translation mount, TT: tip-tilt mount, θ: rotation stage, X: x translation stage, Y: y translation stage, Z: z translation stage.

2.3.2. CALIBRATION AND PERFORMANCE

The PSF of the imaging lens system (L3) is characterized by its beam waist as function of the distance from the focal plane $w(s)$. The PSF is measured by imaging a straight knife edge inside the water-filled cuvette at multiple distances from the focal plane using the translation stage assembly. The measured PSF is fitted using a Gaussian function for all the measured stage translations to determine $w(s)$ and w_0, which is subsequently used to predict the PSF in the reconstructed images. The measured beam waist in water at the

focus is $w_0 = (6.2 \pm 0.1)$ µm.

The axis of rotation of the sample is aligned with the middle pixel column of the camera and positioned in the focal plane using the stage assembly and the tip-tilt adjuster. The center of the sample is positioned at the center of rotation using the $x - y$ adjuster.

2.3.3. SAMPLE PREPARATION

Green fluorescent silica particles (KI-PSI-G4.0, Kisker) with a diameter of 4.0 µm are suspended in 1%, low melting point agarose gel (H26417.14, VWR). The fluorescent particles have peak excitation and emission wavelengths of 485 nm and 510 nm respectively. During measurements the agarose phantom is submersed in a cuvette filled with demineralized water to reduce refractive-index differences at the borders of the sample.

A ten day old transgenic zebrafish larvae expressing membrane bound green fluorescent protein (GFP) from a beta-actin promoter is mounted in low melting point agarose and imaged in the OPT system. Before mounting, the zebrafish larvae is euthanized in ice water in the Erasmus Medical Center, Rotterdam according to animal welfare regulations. Animal experiments are approved by the Animal Experimentation Committee of the Erasmus MC, Rotterdam. Imaging of the zebrafish is performed using an additional 7 : 1 manual zoom section (35-31-10-000, Qioptic) in the lens assembly L3. Projections are measured at 1° intervals over the full 360° range with an integration time of 1 s. Ten vertical slices are averaged before applying the deconvolution algorithm for 4 iterations.

2.3.4. DATA ANALYSIS

After acquisition, sinograms are created by the summation of 100 pixel rows. This ensures that the slice is thick with respect to the spot size on the detector such that Eq. (2.16) is valid. Subsequently, a constant background is removed from the sinograms. After correction for photobleaching with a characteristic e^{-1} timescale of 798 seconds, the center pixel row in the sinograms is aligned with the center of rotation. Reconstruction of tomographic images is performed from all recorded projections using the MATLAB function *iradon*.

After reconstruction, the fluorescent beads are manually identified in the tomographic images. All visible beads are included in the analysis, except beads on the agarose-water interface as there might be clustering and refraction effects at the boundaries. A 0.31×0.31 mm region of interest (ROI) is selected for each bead and fitted with the elliptical Gaussian of Eq. (2.21) using the MATLAB function *fit*.

2.3.5. IMAGE DECONVOLUTION

The position-dependent PSF of the OPT system is used to deblur the reconstructed images. After standard reconstruction with an inverse Radon transformation the image is transformed into cylindrical coordinates (r,θ), which ensures a space-invariant PSF in the r direction. The PSF in the θ direction only changes with r. After subsequent 1D deconvolutions in the θ and r directions the image is transformed back into Cartesian coordinates to obtain a deblurred reconstruction image. The deconvolution is performed using the Lucy-Richardson method for 100 iterations implemented using the MATLAB function *deconvlucy*, The coordinate transformations and image deconvolution combined take several minutes to process on a standard desktop computer.

2.4. RESULTS

A single slice of an OPT reconstruction of the sample with fluorescent beads is shown in Fig. 2.5(a). Several individual beads are visible in the image, showing the characteristic blurring in the tangential direction, as predicted by Eq. (2.21). Also the contours of the agarose phantom are visible due to some fluorescent beads sticking to this boundary. An example of a single-bead ROI, Fig. 2.5(b), and the corresponding fitted Gaussian, Fig. 2.5(c), are also shown.

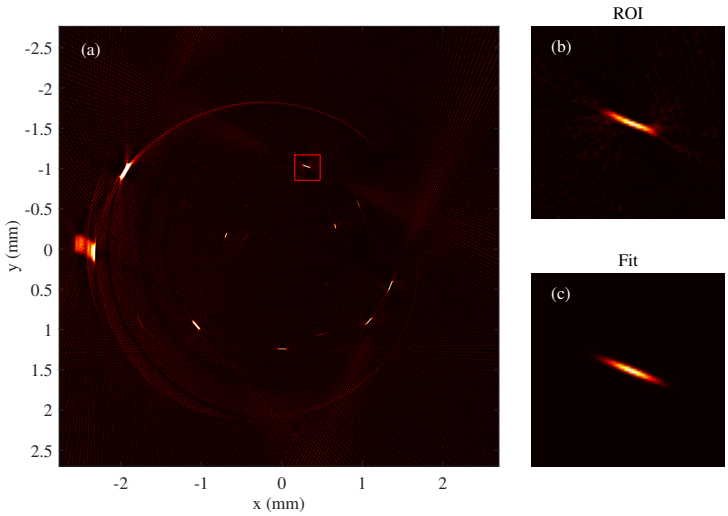

Figure 2.5: (a) Reconstructed slice of the phantom showing single fluorescent beads. A ROI (b) around the bead is selected and the fluorescence emission is fitted (c).

The radial and tangential FWHM of all the selected beads in the reconstructed images are shown in Fig. 2.6(a) for both the radial and tangential directions. The measured resolutions are compared to the theoretical model of Eq. (2.21) based only on the measured evolution of the Gaussian beam waist with displacement. The measured FWHM resolution agrees well with the theoretically predicted values. The resolution in the radial direction remains constant throughout the image, while the tangential resolution becomes worse for larger distances from the center of rotation.

Reconstructed images can be enhanced by deconvolution with the spatially-varying PSF of the OPT system based on our theory. The overall effect of the image deconvolution is shown in Fig. 2.6(b), where the radial and tangential FWHM of all the analyzed beads after deconvolution are plotted as function of their radial distance from the center of rotation. The theoretically predicted FWHM resolutions without performing deconvolution are plotted for comparison. The graph shows that the deconvolution algorithm reduces both the radial and tangential resolution for most of the beads to below the radial resolution limit.

Figure 2.7 shows the deconvolution results for two selected beads in the OPT image. An image of the beads before deconvolution (Figs. 2.7(b) and (f)) is compared to an image after deconvolution (Figs. 2.7(c) and (g)). Fluorescence cross sections in radial and

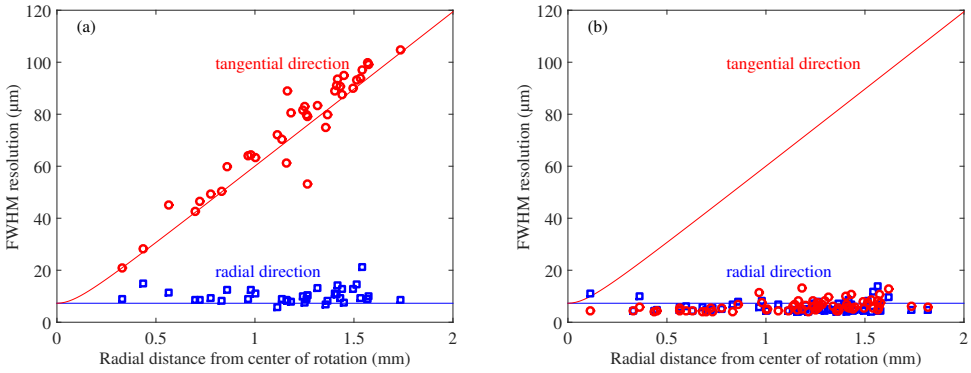

Figure 2.6: (a) Radial (blue) and tangential (red) FWHM resolution as function of the radial distance from the center of rotation. Theoretical curves (solid lines) are compared to measured FWHM resolution in radial (open blue squares) and tangential (open red circles) directions. In most cases the marker size exceeds the error margin. (b) Radial (open blue squares) and tangential (open red circles) FWHM resolution after deconvolution. Theoretical curves plotted for comparison.

tangential direction (Figs. 2.7(d) and (h)) are significantly wider in the original image compared to the corresponding cross sections in the deconvoluted image (Figs. 2.7(e) and (i)).

The deconvolution algorithm is applied to an OPT scan of a GFP labelled zebrafish larvae to illustrate the performance on a biological sample. Figure 2.8 shows the resulting reconstruction of a single slice before and after deconvolution. Figure 2.8(a) shows a single projection of the zebrafish. Comparison of Figs. 2.8(b) and (c) shows a clear improvement in image quality is obtained by application of the spatially-variant deconvolution algorithm.

2.5. DISCUSSION

In this paper, we have presented a theoretical model that describes the spatially-variant resolution of optical tomography systems. The theoretical model relates the size of the PSF in the reconstructed tomographic image to the PSF of the imaging optics. In the derivation of the model we have assumed that the reconstructed slice is thick with respect to the spot size of a point emitter on the detector. This approximation reduces the model to 2D and neglects any 3D imaging effects. If the slice is thin then the factor $A(\theta)$ in Eq. (2.15) should be taken into account. An analytical expression of this effect proved to be difficult to calculate analytically. Consequently, taking 3D effects into account leads to complex PSF shapes in the reconstruction domain that are challenging to deconvolute.

The theoretical model described in this paper assumes that the PSF of the imaging optics can be described by a Gaussian beam. Although the PSF of a typical lens system is not necessarily a Gaussian beam, for the lens system used in our experiments this was a good approximation. A fit of the measured PSF with a Gaussian beam-shape had a value of R-squared of $R^2 = 0.9962$.

The measured resolution in both radial and tangential directions agrees well with the

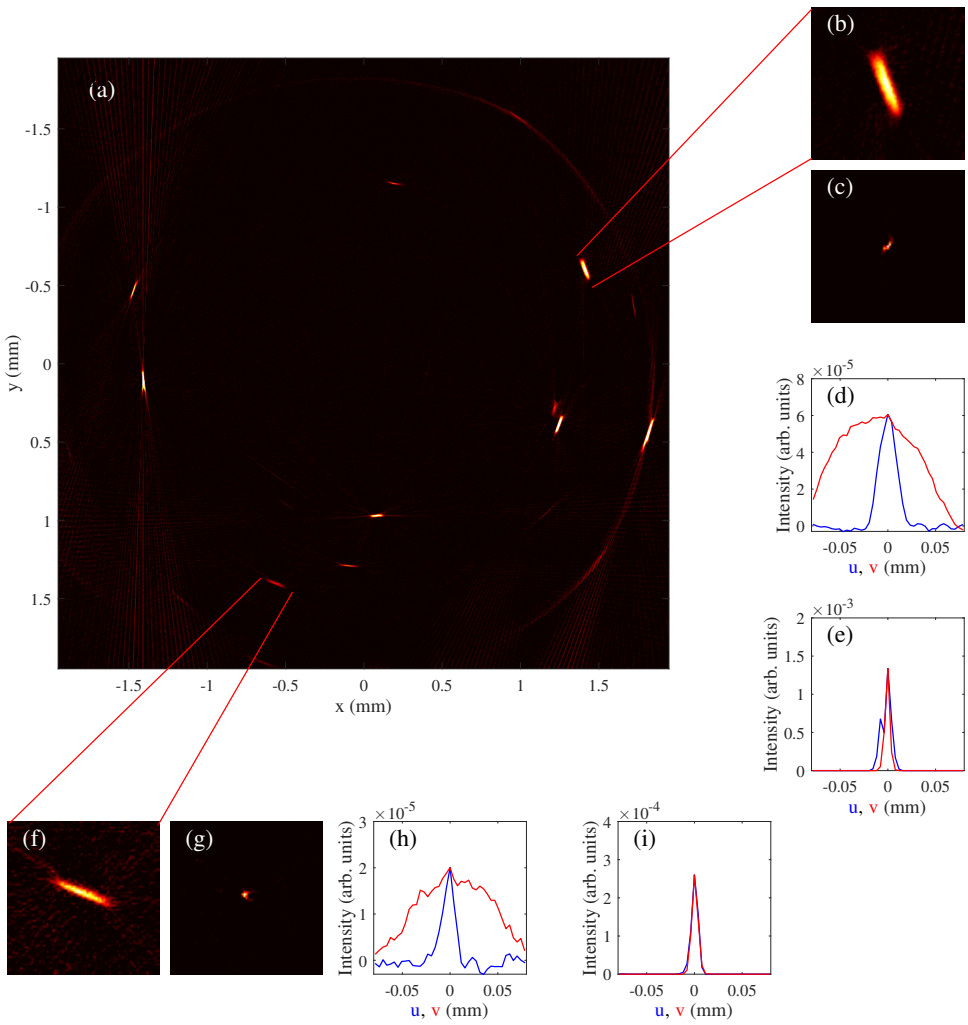

Figure 2.7: (a) Standard reconstructed slice of the fluorescence phantom. The image of a typical bead (b) and (f) show significant sharpening after the deconvolution (c) and (g). Radial (blue) and tangential (red) cross-sections of the initial and deconvoluted images of the bead are shown in (d) and (h), and (e) and (i) respectively.

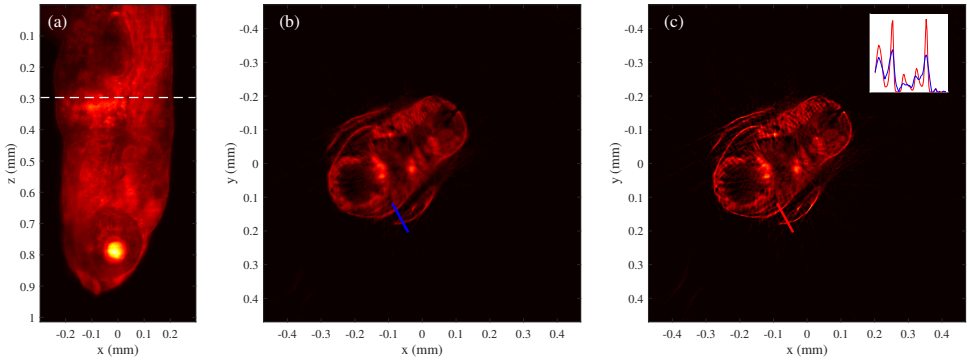

Figure 2.8: (a) Projection of a zebrafish with a reconstructed slice before (b) and after (c) deconvolution. The reconstruction corresponds to the vertical position indicated by the white line in (a). The inset compares the intensity profiles allong the indicated lines.

theoretical model. We attribute the spread in the measured dimensions of the spots to small imperfections in the alignment of the sample and the axis of rotation. The summation of 100 rows in the z-direction does not guaranty the absence of 3D effects as some beads will be close to edges of a section. This influences the resolution as well as reducing the validity of the fit-function, causing variations from the predicted resolution.

Knowledge on the spatially-variant resolution in an optical tomography setup allows for specific guidelines for the design of such systems if certain resolution targets are to be achieved. Our model describes how the trade-off between resolution and depth of focus of the imaging optics can be optimally balanced for a certain sample size. A possible design criterion might be to minimize the worst resolution in the entire reconstructed image. Since the radial resolution is constant, this amounts to limiting the tangential resolution at the largest distance from the center of rotation. Figure 2.9 shows the FWHM tangential resolution as a function of the in-focus Gaussian beam waist w_0 for several distances from the center of rotation. At a particular radial distance r a small beam waist results in a large Gaussian beam divergence, giving rise to a poor tangential resolution. As the beam waist increases the beam divergence decreases and the resolution improves. At large w_0 the resolution becomes poor due to the increased beam waist w_0 in-focus. From this result it can be seen that one can sacrifice resolution in the center to improve resolution at the edges of the image. There is clearly an optimal beam waist $w_{0,opt}$ for each distance from the center, given by

$$w_{0,opt} = \sqrt{\frac{\lambda r}{\pi}}. \tag{2.22}$$

The optimal beam waist $w_{0,opt}$ represents the in-focus beam waist for which the tangential resolution at the edges of the object is minimal.

The theoretically derived PSF in the reconstructed images allows for image de-blurring. The Lucy-Richardson deconvolution algorithm applied in this work provides a possible implementation of such a method. It shows that significant improvement can be obtained in image resolution, although the resolution improvement comes at the cost of

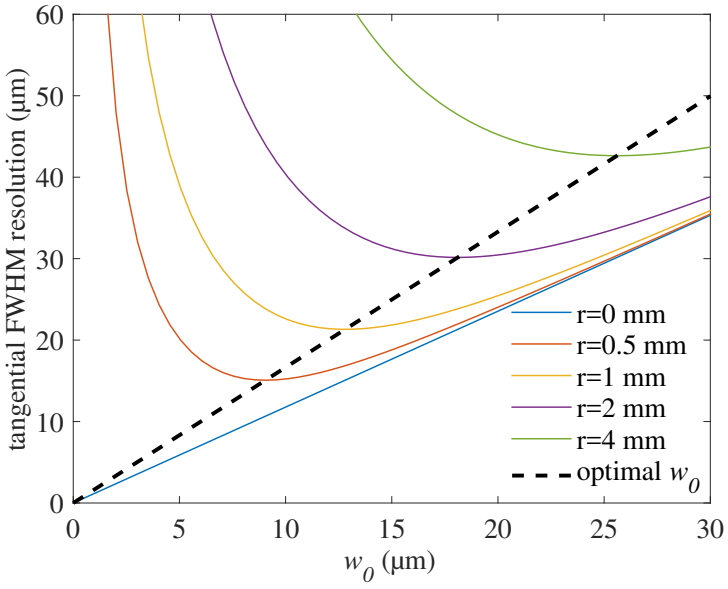

Figure 2.9: Tangential FWHM resolution as function of the beam waist, plotted for several distances from the rotation center.

some increased noise and enhancement of artefacts in the image. We observed that the number of iterations in the deconvolution has a large effect on this trade-off. The use of 100 iterations in this paper was motivated by the increase in resolution mainly. Using fewer iterations degrades the final resolution, but also shows a smaller increase in noise and artefacts. The deconvolution results shown here are a proof of concept, further optimization of our implementation is the topic of current research.

While our model is derived for a Gaussian-beam shaped PSF of the imaging optics with the rotation axes in the focal plane, it can be extended to other beam shapes and focus arrangements with relative ease. Some authors position the focal plane between the center of rotation and the edge of the sample [3]. In addition, other imaging beams can be implemented using the proposed theoretical framework. The depth-of-field of the imaging optics can be extended by implementing a Bessel-beam shaped focus. The resolution in the tomographic reconstructed image obtained by these methods can be modelled and compared in a similar manner as described in this paper.

In a broader scope, the presented model can be useful in other fields that apply tomographic imaging techniques such as terahertz tomography, tomographic phase microscopy, electron microscopy, and PET/SPECT imaging.

2.6. CONCLUSION

We have presented and validated an analysis of the image resolution in optical tomography systems. The model describes the spatially-variant PSF in the reconstructed images as a function of the properties of the imaging optics. The presented model provides users

with a description of the system resolution, provides guidelines for system design, and can be used for image restoration using deconvolution algorithms. The model can be easily adapted for various tomography applications.

REFERENCES

[1] P. J. Keller, A. D. Schmidt, J. Wittbrodt, and E. H. Stelzer, *Reconstruction of zebrafish early embryonic development by scanned light sheet microscopy,* Science **322**, 1065–1069 (2008).

[2] J. Sharpe, U. Ahlgren, P. Perry, B. Hill, A. Ross, J. Hecksher-Sørensen, R. Baldock, and D. Davidson, *Optical projection tomography as a tool for 3D microscopy and gene expression studies,* Science **296**, 541–545 (2002).

[3] J. Sharpe, *Optical projection tomography,* Annu. Rev. Biomed. Eng. **6**, 209–228 (2004).

[4] L. Chen, N. Andrews, S. Kumar, P. Frankel, J. McGinty, and P. M. French, *Simultaneous angular multiplexing optical projection tomography at shifted focal planes,* Opt. Lett. **38**, 851–853 (2013).

[5] Q. Miao, J. Hayenga, M. G. Meyer, T. Neumann, A. C. Nelson, and E. J. Seibel, *Resolution improvement in optical projection tomography by the focal scanning method,* Opt. Lett. **35**, 3363–3365 (2010).

[6] W. Xia, R. M. Lewitt, and P. R. Edholm, *Fourier correction for spatially variant collimator blurring in SPECT,* IEEE Trans. Med. Imag., **14**, 100–115 (1995).

[7] J. R. Walls, J. G. Sled, J. Sharpe, and R. M. Henkelman, *Resolution improvement in emission optical projection tomography,* Phys. Med. Biol. **52**, 2775 (2007).

[8] A. Darrell, H. Meyer, K. Marias, M. Brady, and J. Ripoll, *Weighted filtered backprojection for quantitative fluorescence optical projection tomography,* Phys. Med. Biol. **53**, 3863 (2008).

[9] L. Chen, J. McGinty, H. B. Taylor, L. Bugeon, J. R. Lamb, M. J. Dallman, and P. M. French, *Incorporation of an experimentally determined MTF for spatial frequency filtering and deconvolution during optical projection tomography reconstruction,* Opt. Express **20**, 7323–7337 (2012).

[10] C. M. McErlean, E. Bräuer-Krisch, J. Adamovics, and S. J. Doran, *Assessment of optical CT as a future QA tool for synchrotron X-ray microbeam therapy,* Phys. Med. Biol. **61**, 320 (2015).

[11] M. Gu, *Advanced optical imaging theory,* vol. 75 (Springer Science & Business Media, 2000).

[12] J. Hsieh, *Computed tomography: principles, design, artifacts, and recent advances* (SPIE, Bellingham, WA, 2009), Chap. 3, pp. 55–117.

[13] H. Kogelnik, T. Li. *Laser beams and resonators,* Appl. Opt. **5**, 1550-1567 (1966).

3

Transmission Optical Coherence Tomography Based Measurement of Optical Material Properties

This chapter is based on the following publication:
A. K. Trull[1], **J. van der Horst**[1], J. G. Bijster, and J. Kalkman, *Transmission optical coherence tomography based measurement of optical material properties*, Optics Express, 23(26), 33550-33563, (2015).

[1]These authors contributed equally to this work

3

ABSTRACT

We present transmission optical coherence tomography (transmission OCT) as a versatile tool to measure optical material properties of turbid media. The transmission OCT signal is described in detail and it is demonstrated how the group refractive index (n_g), group velocity dispersion (GVD) and optical attenuation can be determined from this signal. We experimentally validate the refractive index properties of glasses, liquids and glucose water solutions in terms of n_g and GVD. Measurements of scattering coefficients are determined using transmission OCT for suspensions of silica particles. Quantitative agreement is obtained with a dependent scattering model, both for the average as well as the wavenumber resolved optical attenuation coefficient. Good agreement is observed between our measurements and literature values.

3.1. INTRODUCTION

Optical material properties are important in the field of optics where they are paramount to the production of high-quality optical components. Also in other fields such as pharmaceuticals, medical imaging, photo-dynamic therapy and food production are optical material properties important for quality control and diagnostics. However, in contrast to optical materials such as glasses, the optical materials in these fields are turbid, i.e., they have both optical absorption and scattering. Consequently, the characterization of their optical properties such as refractive index (dispersion) and optical attenuation is a lot more challenging.

Collimated transmission measurements, for example, can be used to measure the total attenuation coefficient of turbid media [1]. However, the difficulty with this method is to avoid measuring scattered light on the detector, which is done using pinholes and long path lengths, but nevertheless restricts the measurements to relatively thin samples. Diffuse reflectance spectroscopy has been used to measure the wavelength dependent absorption coefficient and the reduced scattering coefficient to identify the age of bloodstains, where the change of hemoglobin fractions can be observed over time [2]. Yet, diffuse reflectance spectroscopy requires the use of transport theory to calculate the optical properties. Consequently, this technique is limited to samples that are homogeneous or have a known structure. A combination of transmittance and diffuse reflectance measurements can also be used to determine the absorption coefficient, the scattering coefficient and the scattering anisotropy of turbid media [3], but also suffers from the above mentioned effects.

Some techniques are capable of measuring the spatial variation in optical properties, producing an image of the sample. Optical coherence tomography (OCT) has been used to measure light attenuation of tissue and is able to differentiate between normal and tumorous tissue [4]. Low-coherence spectroscopy has been used to image the wavelength dependent absorption and scattering coefficient in vivo in the human skin [5]. Imaging of the refractive index in turbid media has been shown using bifocal OCT [6]. By measuring the optical path length between two focal spots in a sample the refractive index can be obtained. It is also possible to measure the refractive index of turbid media using confocal microscopy [7]. In this case, a layer of immersion fluid of the same thickness as the sample is used in combination with a calibrated z-stage movement. Optical properties of tissue can provide functional information regarding its biological state. The use of optical techniques for biopsies has been shown for example by Wang et al. [8], who demonstrated quantitative phase imaging of breast and prostate biopsies to identify tumour calcifications.

All the techniques described above only provide measurement of either the refractive index or the attenuation coefficients. Part of these techniques rely only on diffuse light while others suffer from it, causing restrictions on the sample size and the type of sample.

Here, we present Fourier-domain transmission optical coherence tomography (transmission OCT) that is used to determine both the refractive index and optical attenuation coefficients. Transmission OCT was first used by Hee et al. [9] for imaging of objects embedded in turbid media. Recently, transmission OCT has been used to measure the scattering coefficient μ_s in turbid media [10]. We show that transmission OCT can provide

an estimation of the group refractive index, n_g, the group velocity dispersion, GVD, as well as the (spectrally resolved) total attenuation coefficient of the material. The advantage of using transmission OCT is the combination of confocal gating and path-length selectivity (coherence gating). This allows for a strong rejection of scattered light, as well as the possibility to further filter out multiple scattered light.

First, a theoretical framework is provided that describes the transmission OCT in the presence of attenuation and dispersion. Second, the experimental setup is described together with an algorithm to analyze the experimental data. Finally, experimental data is presented that demonstrates the proposed techniques.

3.2. THEORY

3.2.1. THE TRANSMISSION FOURIER DOMAIN OCT SIGNAL

Transmission OCT is based on the interaction of light in the sample arm of a Mach-Zehnder interferometer with light propagating in the reference arm. A schematic diagram of the Mach-Zehnder interferometer with spectral-domain detection as used for transmission OCT is given in Fig. 3.1. The experimental realization of the setup is described in more detail in Section 3.3.1.

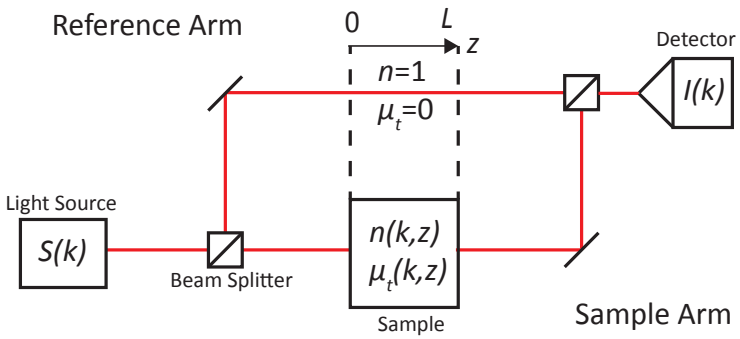

Figure 3.1: Schematic diagram of the Fourier-domain transmission OCT system. $I(k)$: detected intensity at the spectrometer, L: length of the sample, $n(k,z)$: refractive index of the sample, $\mu_t(k,z)$: total attenuation, $S(k)$: source intensity.

Light from the light source is launched into the interferometer. The source intensity spectrum is given by $S(k) = E_s(k)^* E_s(k)$, with $*$ denoting complex conjugation, k is wavenumber in vacuum $k = 2\pi/\lambda$ and $E_s(k)$ are plane electromagnetic waves. In the following, we assume one-dimensional rectilinear propagation of scalar plane waves light field through the interferometer. Polarization and multiple scattering are neglected in our model. Due to averaging over many optical cycles, the time dependence of the signals is disregarded and all parameters are real numbers unless stated otherwise. We neglect any path lengths and phase factor that are equal for both interferometer arms. The incoming beam is first split and later combined by an ideal beam splitter with an (intensity) reflection coefficient of α and transmission coefficient $1-\alpha$.

For the light wave propagating in the reference arm we assume it to be filled with

air, i.e. the refractive index is unity, $n(k,z) = 1$ and there is no attenuation, $\mu(k,z) = 0$. Assuming ideal mirrors in the interferometer with unity reflectivity, the reference arm field $E_{ref}(k)$ at the detector is given by

$$E_{ref}(k) = [\alpha(1-\alpha)]^{\frac{1}{2}} E_s(k) \exp(ikL), \tag{3.1}$$

where $i = (-1)^{1/2}$, and where L is the physical length equal to the physical length in the sample arm in which interaction takes place. After interaction with a sample of length L in the sample arm the field from the sample arm falling on the detector is

$$E_{sam}(k) = [\alpha(1-\alpha)]^{\frac{1}{2}} E_s(k) \exp\left(-\frac{1}{2}\int_0^L \mu_t(k,z)dz\right) \exp\left(ik\int_0^L n(k,z)dz\right), \tag{3.2}$$

where $\mu_t(k,z)$ is the total attenuation coefficient and L is the distance along the optical path in the sample arm where interaction takes place. In the following we consider only homogeneous media, i.e. $\mu(k,z) = \mu(k)$ and $n(z,k) = n(k)$, and the integrals are replaced by multiplications with L. The total intensity at the detector $I(k) = (E_{ref}(k) + E_{sam}(k))(E_{ref}(k) + E_{sam}(k))^*$ consists of the reference arm intensity, the sample arm intensity and the cross terms which contain the interference signal. Combining Eq. (3.1) and Eq. (3.2), and retaining only the interference term of the intensity on the detector we obtain

$$I_{int}(k) = 2\alpha(1-\alpha)E_s^2(k) \exp\left(-\frac{1}{2}L\mu_t(k)\right) \cos[kL(n(k)-1)]. \tag{3.3}$$

The measured interference signal is proportional to an exponential factor describing the optical attenuation and is proportional to a cosine with a phase that is modulated by the spectral variation of the refractive index (dispersion).

3.2.2. MATERIAL DISPERSION

The term $n(k) - 1$ in Eq. (3.3) represents the dispersive properties of the sample. Commonly, the dependence of the refractive index of a material with wavelength is expressed by the Sellmeier equation [11]. Here, we make a polynomial expansion of n around k_c, the center wavenumber of the source spectrum $S(k)$:

$$n(k) = \sum_{j=0}^{J} n_j \left(\frac{k-k_c}{k_c}\right)^j, \tag{3.4}$$

with a total number of coefficients $J \in \mathbb{N}$. Based on the literature values for the parameters of the Sellmeier equation or experimental data presenting $n(\lambda)$, the coefficients n_j of the polynomial expansion can be determined using a fit. Another common way to describe the dispersive properties of a material is in terms of the group refractive index and the GVD. At the center wavenumber, these are given by $n_g(k_c) = n(k) + k(\mathrm{d}n/\mathrm{d}k)|_{k=k_c}$ and $GVD(k_c) = 1/c^2(\mathrm{d}n_g/\mathrm{d}k)|_{k=k_c}$, respectively. Here c is the speed of light.

The dependence of $n(k)$ on k, from Eq. (3.4), causes the oscillations of the cosine in Eq. (3.3) to be non-linear. For the attenuation analysis (Section 3.2.3) and for the

dispersion estimation, the phase of the signal of Eq. (3.3) has to be extracted. Therefore the analytical signal of the interference signal is calculated [12, 13], which is given by

$$\widetilde{I_{int}}(k) = I_{int}(k) + i\mathscr{H}\{I_{int}(k)\}, \tag{3.5}$$

where $\mathscr{H}\{\cdot\}$ denotes the Hilbert transform operator. The phase of $\widetilde{I_{int}}(k)$ can then be determined by

$$\varphi(k) = \tan^{-1}\left(\frac{\mathscr{H}\{I_{int}(k)\}}{I_{int}(k)}\right), \tag{3.6}$$

which is equal to the argument of the cosine expression in Eq. (3.3) performing a Taylor expansion of $\varphi(k)$ around k_c and combining this with the polynomial expansion of $n(k)$ around k_c in Eq. (3.4) for $J = 2$, we obtain

$$\frac{\varphi(k)}{k_c L} = (n_0 - 1) + (n_0 - 1 + n_1)\left(\frac{k - k_c}{k_c}\right) + (n_1 + n_2)\left(\frac{k - k_c}{k_c}\right)^2. \tag{3.7}$$

The coefficients of Eq. 3.7 can be determined by fitting $\varphi(k)$ with a polynomial. From the fit parameters coefficients, n_0 and n_1, are determined and the group refractive index follows as $n_g(k_c) = n_0 + n_1$ and the group velocity dispersion $GVD(k_c) = 2(n_1 + n_2)/(k_c c^2)$.

In the z-domain, the dispersion leads to a broadening of the transmission peaks. Using the complex notation of the analytical signal it is easy to see that the phase can be linearized by multiplying the Hilbert transformed interference signal with $\exp[i\Delta\varphi(k)]$, where $\Delta\varphi(k) = \varphi(k) - \varphi_{\text{linear}}(k)$ [13]. The dispersion corrected signal in the z-domain is given by the inverse Fourier transform of the dispersion corrected analytic signal

$$I_c(z) = \mathscr{F}^{-1}\{|\widetilde{I_{int}}(k)|\exp[i\Delta\varphi(k)]\}, \tag{3.8}$$

where $\mathscr{F}^{-1}\{\cdot\}$ denotes the inverse Fourier transform of the given signal.

3.2.3. ATTENUATION COEFFICIENT

After dispersion correction, the attenuation coefficient can be determined both from the spectral or spatial domain signal. Taking the inverse Fourier transform of Eq. (3.3) and assuming the attenuation does not vary a lot over the spectral bandwidth of the system, i.e. $\mu_t(k) = \mu_t$, we obtain an equation for the spatial domain transmission OCT signal

$$a(z) = \alpha(1-\alpha)\exp\left(-\frac{1}{2}L\mu_t\right)\mathscr{F}^{-1}\{E_s^2(k)\}(z) \otimes \left[\delta\left(z - L(n_g - 1)\right) + \delta\left(z + L(n_g - 1)\right)\right], \tag{3.9}$$

where $\otimes$ denotes a convolution. Performing a reference measurement with attenuation $\mu_t = 0$ and a measurement on the sample, one obtains two z-domain signals. The signal of the sample differs from that of the reference measurement by a possible shift of the delta functions and a change in height, caused by the optical attenuation. From Eq. (3.9) it can be deduced that the attenuation coefficient can be determined by measuring the height of the peak in the z-domain of the reference and sample measurements, a_{ref} and a_{sam}, respectively, and using

$$\mu_t = \frac{2}{L}\ln\left(\frac{\max|a_{ref}|}{\max|a_{sam}|}\right). \tag{3.10}$$

The attenuation coefficient thus obtained is an average over the spectral bandwidth of the system. The spatial domain analysis offers the advantage of path-length selectivity. In this way the ballistic light can be filtered from the scattered light, which can then be used to estimate the attenuation μ_t and the refractive index of the sample.

Alternatively, from Eq. (3.3) and Eq. (3.8) the absolute value of the analytical signal can be recognized as the complex magnitude of the interference signal

$$|\widetilde{I_{int}}(k)| = \alpha(1-\alpha)E_s^2(k)\exp\left(-\frac{1}{2}L\mu_t(k)\right). \tag{3.11}$$

The wavenumber dependent attenuation coefficient $\mu_t(k)$ can be determined by performing a reference and a sample measurement of $|\widetilde{I_{int}}(k)|$. Similar to Eq. (3.10), the ratio of these two signals then results in $\mu_t(k)$.

3.3. METHODS

3.3.1. EXPERIMENTAL SETUP

The Fourier domain transmission OCT setup is depicted in Fig. 3.2. It is based on a Mach-Zehnder interferometer with spectral domain detection of the interference signal. A fiber based super-luminescent diode (D-1300-HP, Superlum) with a center wavelength of 1300 nm and a full width half maximum (FWHM) bandwidth of 110 nm is used as a light source. After collimation by an achromatic doublet lens (AC254-045-C-ML, Thorlabs), the light is split into the reference and sample arm by a 50/50 beamsplitter (BS015, Thorlabs). Optical power in the two arms is regulated by neutral density filters (NDC-100C-4M, Thorlabs) in each arm. The reference arm contains an optical delay line, that is tunable in length by means of a translation stage (PT1/M, Thorlabs). The sample arm contains two confocal 200 mm achromatic lenses (AC254-200-C-ML, Thorlabs). Samples are mounted in the focal point between the two lenses. After recombination by a second 50/50 beamsplitter the resulting beam is expanded by a 4-f lens system (AC254-060-C-ML and AC508-080-C-ML, Thorlabs) before being introduced to a spectrometer. A pinhole is placed at the focus position between the two lenses of the 4-f system to remove any stray light. Spectral domain detection is performed by a home build spectrometer, consisting of a holographic grating (1145 l/mm, Wasatch Photonics), an SWIR imaging lens (S5LPJ0037/360, Sill Optics), and a 76 kHz InGaAs linescan camera (GL2048L, Sensors Unlimited). Camera data is acquired using a framegrabber (PCIe-1433, National Instruments) and Labview software (National Instruments).

3.3.2. SETUP CALIBRATION AND PERFORMANCE

The spectrometer is calibrated using an Argon gas discharge lamp (AvaLight-CAL-AR, Avantes). The calibration lamp is placed on the free-side of the first beamsplitter of the interferometer. The emission spectrum of the lamp is recorded by the spectrometer and the measured emission lines are compared to reference values from literature. A third degree polynomial is fitted through the data to obtain a relation between pixel number and wavelength. The performance of the transmission OCT system is checked using the movable delay line in the reference arm. This yields a maximum path length difference of 11.6 ± 0.1 mm. The axial resolution of the system is determined by measuring the

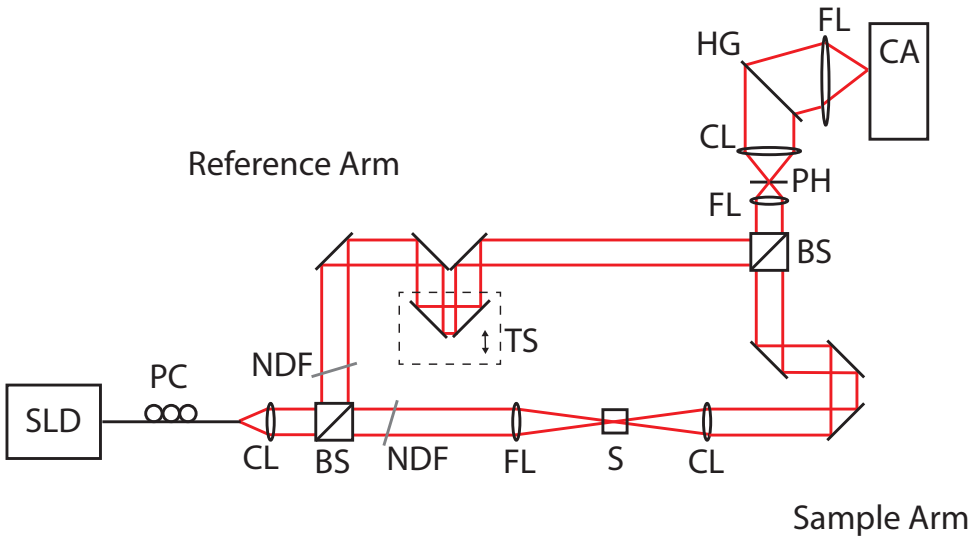

Figure 3.2: Schematic diagram of the experimental setup. BS: beam splitter, CA: camera, CL: collimation lens, FL: focusing lens, HG: holographic grating, NDF: Neutral density filter, PC: polarization controller, PH: pinhole, S: Sample, SLD: superluminescent diode, TS: translation stage

FWHM of the signal peak in the z-domain with no sample in the interferometer. The measured axial resolution of the system is 18 ± 1 µm, (bandwidth limited). The lateral point spread function, measured in air, has an in-focus FWHM waist of 32.8 ± 0.7 µm. Following the definition of Nassif et al. [14], the roll-off parameter of the system is $w = 2.1 \pm 0.1$. Measurements using neutral density filters show a signal sensitivity of -106 dB.

3.3.3. SAMPLE PREPARATION AND MEASUREMENT

Measurements of n_g and the GVD are performed on both liquid samples and glass plates. The glass plates provide a good validation as the optical material properties for glasses are well known. Four different glass plates are used in the experiments; N-BK7 (WG11050, Thorlabs), sapphire (WG31050, Thorlabs), UV-fused silica (WG41050, Thorlabs) and calcium fluorite (WG51050, Thorlabs). All glass plates are 5 mm thick and uncoated. Liquid samples used for the refractive index measurements are: ethanol (32221, Sigma-Aldrich), de-mineralized water and glucose solutions. These liquids were measured using a 10 mm path length, fused quartz cuvette (CV10Q3500F, Thorlabs) placed in the sample arm. Refractive index data is obtained after averaging of 5000 measurements per sample.

Measurements of attenuation are performed on monodisperse silica particle suspensions and on de-mineralized water. Two different particle sizes are considered; 0.5 µm and 1.5 µm diameter. Silica particles (KI-PSI-0.5P and KI-PSI-1.5P, Kisker Biothech) in powdered form are suspended in de-mineralized water containing 0.3 mM of sodium dodecyl sulfate to prevent aggregation [10]. Suspensions are vortexed for 60 minutes and sonicated for 30 minutes before measurements. All silica particle suspensions are measured in a 1 mm path length cuvette (Z802689-1EA, Sigma-Aldrich) mounted in the

sample arm. Calculating the attenuation coefficient for the silica particle suspensions, water is used as a reference in Eq. (3.10). In this way the difference in attenuation between the suspension and water is obtained, removing the contribution of the water absorption to the total attenuation of the sample. Leaving only the scattering contribution by the silica particles $\mu_t = \mu_s$. For all the measurements of silica particle suspensions, including the water reference, 100000 measurements are averaged. The wavelength dependent absorption coefficient of water is determined from 1000 spectra.

The particle-sizes are measured using a Malvern Zetasizer, obtaining a mean diameter of 1138 ± 48 nm for the KI-PSI-1.5P particles and 426.6 ± 61.5 nm for the KI-PSI-0.5P particles. These measured sizes are smaller than the factory values, but are consistent with electron microscopy measurements on the same products from the same manufacturer [10].

3.3.4. DATA ANALYSIS ALGORITHM

After acquisition the spectral data is stored in raw binary format. It is analyzed using software written in MATLAB (Mathworks, R2014b). An overview of the data processing flow is presented in Fig. 3.3. The data acquisition includes a measured spectrum $I(k)$, a spectrum of the reference arm only, $I_{ref}(k)$, and a spectrum for the sample arm only, $I_{sam}(k)$. Furthermore the calibrated wavenumber k is obtained from a combination of the spectrometer calibration and an optimization algorithm. The polynomial coefficients of the wavenumber calibration is optimized with respect to the group index of water using a trust-region algorithm (MATLAB function *fminunc*). The third order polynomial coefficients of the spectrometer calibration are used as the initial parameter estimate.

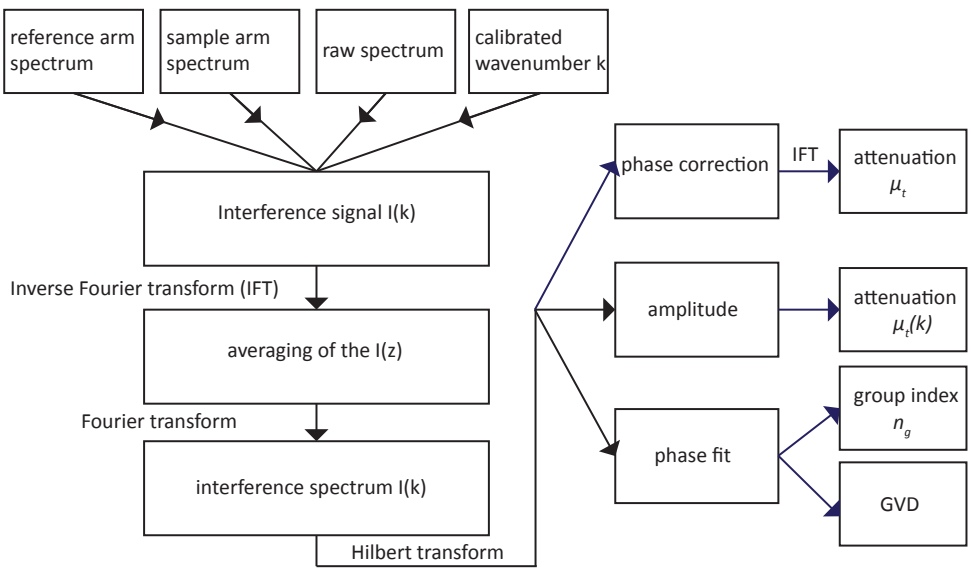

Figure 3.3: Schematic illustration of the analysis algorithm for the determination of the optical material properties.

As spectrum containing only the interference contribution is generated by subtracting all other contributions, $I_{int}(k) = I(k) - I_{ref}(k) - I_{sam}(k)$. To obtain the average interference spectrum this signal is inverse Fourier transformed, averaged and transformed back. For determination of the analytic signal, Eq. (3.5), the built-in MATLAB function *hilbert* is used. Furthermore, the function *phase* is used to determine and unwrap the phase of the given signal. The phase of the signal is cropped in k by choosing the relative heights of the envelope signal with respect to the peak of the envelope to be larger than 0.25. The phase analysis uses the built-in MATLAB function *fit* to fit a cubic polynomial, Eq. (3.7) using the generalized least squares to the difference of the measured phase and a reference phase versus k.

3.3.5. DEPENDENT SCATTERING CALCULATIONS

Calculations of the scattering coefficient are performed using a Mie theory [15] and a dependent scattering model. The effect of dependent scattering is taken into account using the structure factor for computation of the scattering efficiency ratio following the work of Nguyen et al. [10]. Although dependent scattering does not take the effects of multiple scattering into account, the model is appropriate for describing the reduction of power of the ballistic light. Only the ballistic photons that scatter for the first time reduce this power. Interactions between multiply scattered light will only affect our path-length distribution at path-lengths beyond that of the ballistic light.

The dependent scattering model uses the Percus-Yevick model to compute the radial distribution function, which accounts for interactions between particles. Furthermore, we assume the Rayleigh-Debye condition is valid, i.e. the scattering particles can be treated as point scatterers. Input to the dependent scattering calculation are the refractive indices of the medium and the suspended particles, the wavelength of the light, the experimentally determined particle radius and the concentration of the particles.

3.4. RESULTS

A typical set of averaged transmission OCT measurements through a fused silica glass slide is shown in Fig. 3.4. Figure 3.4(a) shows the raw interferometric signal versus wavenumber. The instantaneous phase obtained through Hilbert transform of the interference spectrum is shown in Fig. 3.4(b). A linear relation between the start and end point is added to show the non-linearity of the phase. The non-linear behavior of the phase is caused by the cumulative effects of the material dispersion and by the spectrometer dispersion, both indicated. The phase difference between the linear phase and the phase signal from Fig. 3.4(b) is depicted in Fig. 3.4(c).

The parabolic shape is clearly visible and caused by the large values of $n_1 + n_2$ for fused silica glass and by the non-linearity of the spectrometer. The phase after spectrometer correction (red) has a lower maximum compared to the raw phase signal and shows a more pure parabolic phase behavior. The measured and compensated signal after the Fourier transformation is shown in 3.4(d), where the peak position represents the path length of the ballistic light. Due to dispersion, the measured transmission OCT signal (blue, dashed) is decreased and broadened compared to the dispersion compensated signal (red).

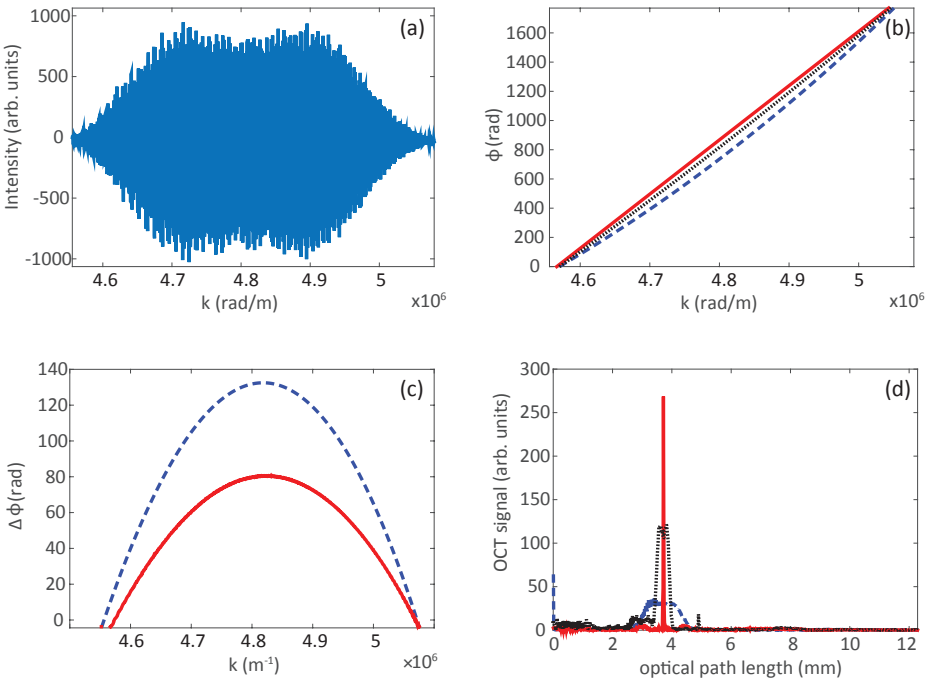

Figure 3.4: Overview of the data processing steps for the fused silica sample (a) Reference and sample arm subtracted interference spectrum. (b) Phase of the original Hilbert transformed signal (blue, dashed), the spectrometer corrected signal (black, points), and the linear phase relation (red). (c) Phase difference between the linear phase and the original signal (blue, dashed) and to the setup dispersion corrected signal (red, solid). (d) z-Domain transmission OCT signal after inverse Fourier transform without dispersion correction (blue, dashed), after setup dispersion correction (black, points) and after material dispersion correction (red, solid).

3.4.1. REFRACTIVE INDEX AND GROUP VELOCITY DISPERSION QUANTIFICATION FOR GLASSES AND LIQUIDS

Figure 3.5 shows the dispersion results of four different glasses: BK7, fused silica, sapphire and calcium fluoride (CaF_2), and two liquids: water and ethanol. Figure 3.5(a) shows the results for the group refractive index for the different materials. The red bars denote the measured values using transmission OCT. It can be seen that the group refractive indices are close to the values from literature [11, 16–28]. BK7, fused silica and CaF_2 are slightly underestimated compared to the literature values, whereas for sapphire a relatively large underestimation of 3.2 percent is observed. Water has a slight overestimation of 0.56 percent and for ethanol the underestimation is 2.5 percent. The group velocity dispersion is shown in Fig. 3.5(b). It can be seen that the group velocity dispersion of all materials, except fused silica, are somewhat overestimated compared to the literature values. For fused silica the group velocity dispersion values are spread between the literature values.

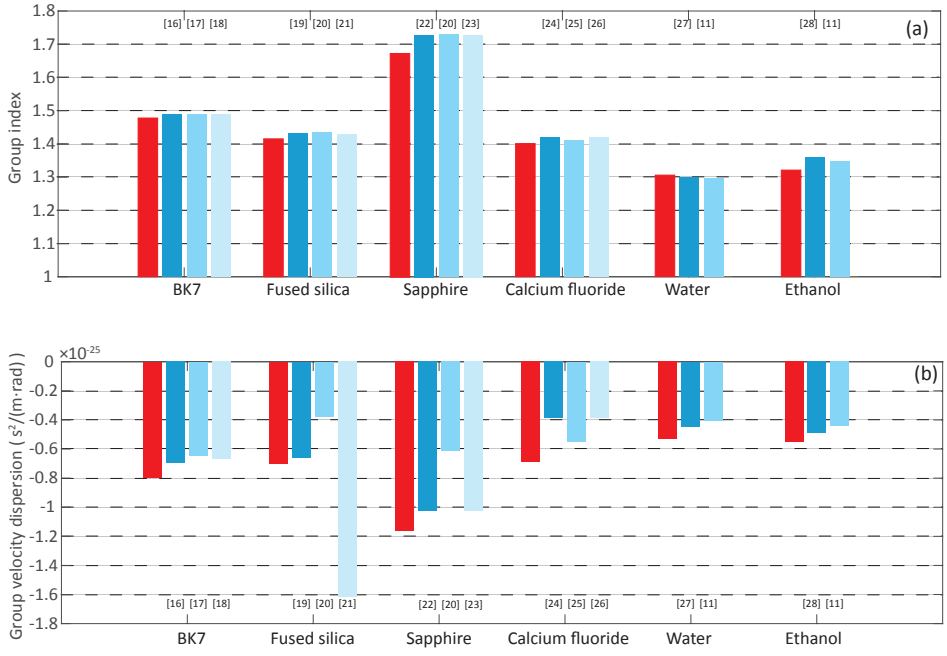

Figure 3.5: Measured group refractive index (a) and group velocity dispersion (b) compared with literature values. The measured values are denoted in red and the literature values are visualized in shades of blue with the reference indicated above and below their respective bar.

Aqueous solutions with different concentrations of glucose are measured to determine the optical properties of the constituent materials (as shown in Fig. 3.6). Both the group refractive index and the GVD follow a linear relation as would be expected from a volume-weighted average of the optical properties. The slope of $(1.21 \pm 0.02)10^{-3}$

group index change per volume percent results in a group refractive index of pure glucose of 1.465 ± 0.004, which agrees well with literature values [29, 30]. The slope of $(-2.05 \pm -0.04)\,10^{-28}\,\mathrm{s}^2/\mathrm{m}\cdot\mathrm{rad}$ GVD change per volume percent results in a GVD of pure glucose of $(-7.34 \pm 0.04)\,10^{-26}\,\mathrm{s}^2/\mathrm{m}\cdot\mathrm{rad}$.

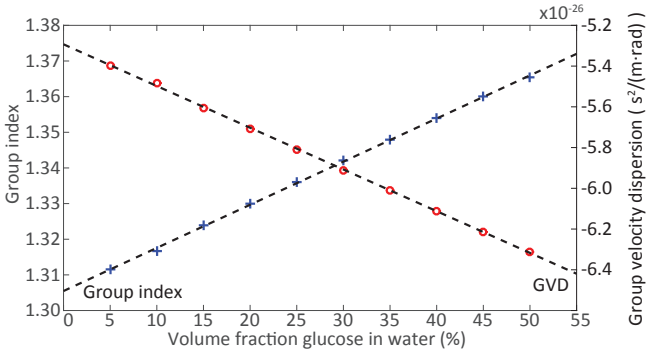

Figure 3.6: Group index and group velocity dispersion for solutions with varying glucose concentration as determined with transmission OCT. The measurements (indicated with open symbols, red and blue) are fitted with a linear regression (dashed black lines).

3.4.2. ATTENUATION AND SCATTERING MEASUREMENTS OF SILICA PARTICLE SUSPENSIONS

Transmission OCT measurements are performed for suspensions of silica particles in different concentrations. Two different particles sizes are considered; 0.5 µm and 1.5 µm diameter. Typical spatial domain data, averaged over 100000 measurements, for the 0.5 µm and 1.5 µm particles are shown in Fig. 3.7(a) and Fig. 3.7(b), respectively. For every concentration, peaks can be observed corresponding to ballistic light transmission. As the concentration of scatterers increases the peak amplitude decreases and the peak moves slightly to longer path lengths. In addition a decaying tail is observed behind the ballistic transmission peak of the 1.5 µm particle suspensions. This tail gradually becomes predominant as the concentration of scatterers increases and is caused by forward scattered light transmitted through the sample. The 0.5 µm particles have a much lower scattering coefficient and scattering anisotropy and do not show the scattered light in the transmission OCT signal.

The measured scattering coefficient μ_s as function of the concentration for the 0.5 µm and 1.5 µm silica particle suspensions are shown in Fig. 3.7(c). For higher concentrations of particles in the suspension, more light is scattered resulting in an increase of the scattering coefficient. At very high concentrations the linear relation between scattering coefficient and particle concentration does not hold and the data is best described by a dependent scattering model. A fit of this model (Section 3.3.5) with the refractive index of the particles as the free parameter, results in $n_0 = 1.430 \pm 0.009$ for the 0.5 µm particles, and $n_0 = 1.444 \pm 0.005$ for the 1.5 µm particles. This value is close to the value of the phase refractive index of 1.447 for fused silica, reported by Malitson [19].

The Hilbert transform method is used to determine the wavelength dependent atten-

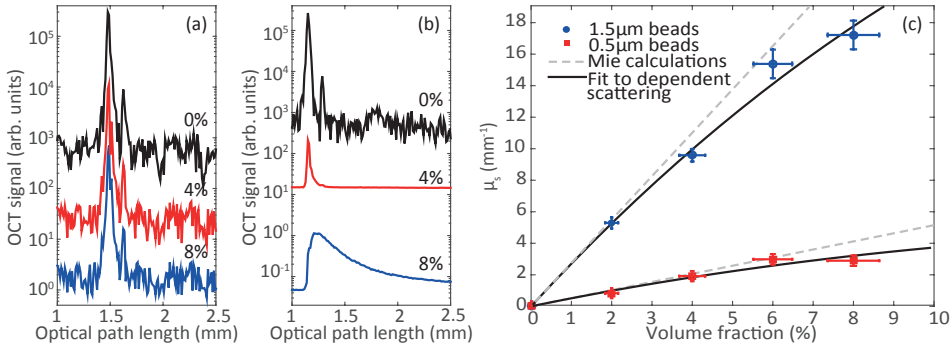

Figure 3.7: Spatial domain transmission OCT data for several concentrations of 0.5 µm (a) and 1.5 µm (b) silica particles in water. Data separated for plotting by multiplication with powers of 10. (c) Measured scattering coefficients for the silica suspensions. The data is fitted using a dependent scattering model (black, solid), which is based on Mie calculations (gray, dashed).

uation coefficient for de-mineralized water and the 2 vol.% suspension of 1.5 µm particles. The measured absorption spectrum of water is shown in Fig. 3.8(a). The measured absorption coefficient agrees well with the data from Kedenburg et al. The wavelength dependent scattering coefficient for the silica particle suspension is shown in Fig. 3.8(b). Dependent scattering calculations are performed over the spectral range for comparison to the measured data. The measured data agree well with the calculated data. In both the water and the particle suspension data, deviations are observed at the edges of the measured attenuation spectra. At these wavelengths the source intensity is low resulting in small signals.

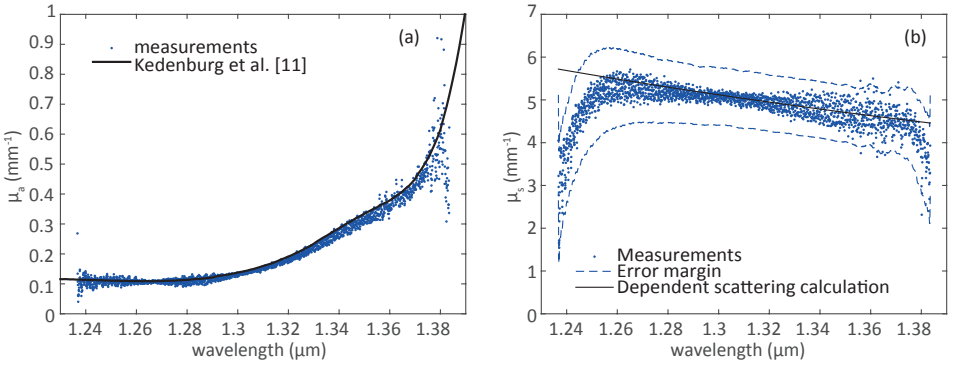

Figure 3.8: (a) Measured absorption coefficient of water versus wavelength (blue, dots) and its comparison to literature [11] (black, solid). (b) Measured scattering coefficient versus wavelength for 2 vol.% 1.5 µm silica particles (blue, dots). Error margin is denoted by the dashed lines. The data is compared to the scattering coefficient obtained from dependent scattering calculations (black, solid).

3.5. DISCUSSION

We showed transmission OCT measurements of n_g, the GVD and the (wavelength resolved) attenuation coefficient. The measurements on glass plates, liquids and glass particle suspensions validated the proposed analysis technique.

The measurements of n_g showed good agreement with values found in literature. Some variation was present in the literature data, possibly caused by differences in the materials used. Our results are slightly less accurate compared to the refractive index measurement of Dirckx et al. [7] and Zvyagin et al. [6]. The GVD measurements, in general, agree well with literature values. Due to the large spread in values reported in literature, exact estimation of the accuracy of our method is difficult. For most measurements the obtained value for the GVD is within the variation represented in literature. We observed that the measured values of n_g and the GVD are very sensitive to variations in the spectrometer calibration. More accurate measurements can be obtained by improving the spectrometer calibration procedure. Increasing the bandwidth of the setup and the thickness of the samples could also provide more accurate results for n_g and GVD. We observed that the exact choice of the cropping factor affects our estimates of both n_g and GVD. The choice of 0.25 resulted in the most accurate estimation of both group velocity index and GVD. Measurement of n_g and the GVD for glucose solutions showed a clear linear behavior over the measured concentration range. By avoiding positioning errors and realignment of the cuvette, possible alignment errors are circumvented. Hence, the glucose measurements show that small differences in refractive index can be measured. The lowest glucose concentration measurable is 0.39 vol. % and was estimated by a linear extrapolation of the slope and comparison to the error in the measurements. This concentration is still larger than typical blood glucose concentrations.

Determination of the attenuation coefficient is shown for both z-domain and spectral domain analysis. For both methods the main experimental difficulty proved to be the prevention of particle aggregation in the suspensions. The z-domain method works in principle up to 20 mean free paths (MFP) of attenuation. The technique is limited to scattering anisotropies up to approximately 0.9. Large anisotropy factors, as for example is the case for tissue, make the discrimination between ballistic and single scattered photons difficult. Increasing the spectral bandwidth results in a more narrow axial point spread function, which facilitates discrimination of ballistic light from scattered light. Additionally, information can be retrieved from the scattered light distribution, either by using a total attenuation coefficient or fitting a scattering model.

Wavelength resolved attenuation coefficients are computed from spectral domain data for water and 2 vol.% of the 1.5 µm particle suspension. The results show good agreement with literature and simulated data respectively. Deviations between measurements and literature are observed at the edges of the spectra. We attribute this to the low power of the light source at these wavelengths which makes it difficult to retrieve the envelope of the measured spectrum using the Hilbert transform. For a similar reason, measurements on samples with high attenuation coefficients (larger then approximately 10 MFP) fail to give accurate results. For highly attenuating samples short time Fourier transform techniques can be applied in combination with an analysis in the z-domain. This provides the benefit of path length discrimination, however, at the cost of reduced spectral resolution.

The measurements presented in this article demonstrate the potential of Fourier-domain transmission OCT as a powerful and versatile platform for measurements of optical properties. Transmission OCT does not rely on scattered light to perform a measurement, and therefore is not based on complicated light transport models or requires a homogeneous sample. In addition, coherence gating provides a means to filter or select scattered from the ballistic light from the measured signal.

Application of the presented techniques can provide a way to optically characterize tissue in biopsies, aiding in the diagnostics of diseases. The multiple modes of contrast provided by our technique can provide a great advantage in this respect. In addition, transmission OCT can provide compact and cost effective measurements in microfluidics and lab-on-a-chip applications. With the onset of OCT on a chip technology this technique can provide a compact, versatile and relatively cheap way to measure optical properties. In addition, the proposed methods for determining n_g and the GVD also can be applied in backscattering OCT, possibly providing additional (functional) tissue contrast. The measurements presented in this paper concern the characterization of the optical properties of a homogeneous bulk sample. The use of transmission OCT can be extended towards imaging spatially varying optical properties using computed tomography techniques.

3.6. CONCLUSION

In conclusion, we presented Fourier-domain transmission OCT as a method for measuring the group refractive index, the group velocity dispersion and the wavelength resolved attenuation coefficient of a wide range of samples. We validated the proposed methods using experimental data. The measurements are in good agreement with literature values and analytical theory. We showed that transmission OCT provides a powerful tool for measurements of various optical properties.

REFERENCES

[1] G. Zaccanti, S. Del Bianco, and F. Martelli, *Measurements of optical properties of high-density media,* Appl. Opt. **42**, 4023–4030 (2003).

[2] R. H. Bremmer, S. C. Kanick, N. Laan, A. Amelink, T. G. van Leeuwen, and M. C. Aalders, *Non-contact spectroscopic determination of large blood volume fractions in turbid media,* Biomed. Opt. Express **2**, 396–407 (2011).

[3] B. Aernouts, E. Zamora-Rojas, R. Van Beers, R. Watté, L. Wang, M. Tsuta, J. Lammertyn, and W. Saeys, *Supercontinuum laser based optical characterization of Intralipid® phantoms in the 500-2250 nm range,* Opt. Express **21**, 32450–32467 (2013).

[4] K. Barwari, D. M. de Bruin, E. C. Cauberg, D. J. Faber, T. G. van Leeuwen, H. Wijkstra, J. de la Rosette, and M. P. Laguna, *Advanced diagnostics in renal mass using optical coherence tomography: a preliminary report,* J. Endourol. **25**, 311–315 (2011).

[5] N. Bosschaart, D. J. Faber, T. G. van Leeuwen, and M. C. Aalders, *In vivo low-coherence spectroscopic measurements of local hemoglobin absorption spectra in human skin,* J. Biomed. Opt. **16**, 100504–100504 (2011).

[6] A. V. Zvyagin, K. K. Silva, S. A. Alexandrov, T. R. Hillman, J. J. Armstrong, T. Tsuzuki, and D. Sampson, *Refractive index tomography of turbid media by bifocal optical coherence refractometry,* Opt. Express **11**, 3503–3517 (2003).

[7] J. J. J. Dirckx, L. C. Kuypers, and W. F. Decraemer, *Refractive index of tissue measured with confocal microscopy,* J. Biomed. Opt. **10**, 044014–044014 (2005).

[8] Z. Wang, K. Tangella, A. Balla, G. Popescu, *Tissue refractive index as marker of disease,* J. Biomed. Opt. **11**, 116017-1160177 (2011).

[9] M. R. Hee, E. A. Swanson, J. A. Izatt, J. M. Jacobson, and J. G. Fujimoto, *Femtosecond transillumination optical coherence tomography,* Opt. Lett. **18**, 950–952 (1993).

[10] V. D. Nguyen, D. J. Faber, E. van der Pol, T. G. van Leeuwen, and J. Kalkman, *Dependent and multiple scattering in transmission and backscattering optical coherence tomography,* Opt. Express **21**, 29145–29156 (2013).

[11] S. Kedenburg, M. Vieweg, T. Gissibl, and H. Giessen, *Linear refractive index and absorption measurements of nonlinear optical liquids in the visible and near-infrared spectral region,* Opt. Mater. Express **2**, 1588–1611 (2012).

[12] Y. Verma, P. Nandi, K. D. Rao, M. Sharma, and P. K. Gupta, *Use of common path phase sensitive spectral domain optical coherence tomography for refractive index measurements,* Appl. Opt. **50**, E7–E12 (2011).

[13] A. F. Fercher, C. K. Hitzenberger, M. Sticker, R. Zawadzki, B. Karamata, and T. Lasser, *Numerical dispersion compensation for partial coherence interferometry and optical coherence tomography,* Opt. Express **9**, 610–615 (2001).

[14] N. Nassif, B. Cense, B. Park, M. Pierce, S. Yun, B. Bouma, G. J. Tearney, T. C. Chen, and J. F. de Boer, *In vivo high-resolution video-rate spectral-domain optical coherence tomography of the human retina and optic nerve,* Opt. Express **12**, 367–376 (2004).

[15] C. Mätzler, *MATLAB functions for Mie scattering and absorption, version 2,* IAP Res. Rep. **8** (2002).

[16] Schott, *Optical glass data sheets,* (2012).

[17] Hikari, *Optical catalogue,* (2015).

[18] Sumita, *Optical glass,* (2015).

[19] I. H. Malitson, *Interspecimen comparison of the refractive index of fused silica,* J. Opt. Soc. Am. **55**, 1205–1208 (1965).

[20] B. Tatian, *Fitting refractive-index data with the Sellmeier dispersion formula,* Appl. Opt. **23**, 4477–4485 (1984).

[21] Heraeus, *Quartz Glass for Optics Data and Properties* (2015).

[22] I. H. Malitson, *Refraction and dispersion of synthetic sapphire,* J. Opt. Soc. Am. **52**, 1377–1379 (1962).

[23] W. C. Tan, K. Koughia, J. Singh, and S. O. Kasap, *Fundamental optical properties of materials I,* in *Optical Properties of Condensed Matter and Applications,* Jai Singh (John Wiley and Sons, Ltd, Chichester, UK. 2006)

[24] H. H. Li, *Refractive index of alkaline earth halides and its wavelength and temperature derivatives,* J. Phys. and Chem. Ref. Data **9**, 161–290 (1980).

[25] M. Daimon and A. Masumura, *High-accuracy measurements of the refractive index and its temperature coefficient of calcium fluoride in a wide wavelength range from 138 to 2326 nm,* Appl. Opt. **41**, 5275–5281 (2002).

[26] I. H. Malitson, *A redetermination of some optical properties of calcium fluoride,* Appl. Opt. **2**, 1103–1107 (1963).

[27] M. Daimon and A. Masumura, *Measurement of the refractive index of distilled water from the near-infrared region to the ultraviolet region,* Appl. Opt. **46**, 3811–3820 (2007).

[28] J. Rheims, J. Köser, and T. Wriedt, *Refractive-index measurements in the near-IR using an Abbe refractometer,* Meas. Sci. Technol. **8**, 601 (1997).

[29] W. M. Yunus and A. B. Rahman, *Refractive index of solutions at high concentrations,* Appl. Opt. **27**, 3341–3343 (1988).

[30] S. R. Kachiraju and D. A. Gregory, *Determining the refractive index of liquids using a modified Michelson interferometer,* Opt. and Laser Technol. **44**, 2361–2365 (2012).

4

DEEP-TISSUE LABEL-FREE QUANTITATIVE OPTICAL TOMOGRAPHY

This chapter is based on the following publication:
J. van der Horst, A. K. Trull, and J. Kalkman, *Deep-tissue label-free quantitative optical tomography*, Manuscript in preparation.

4

ABSTRACT

Deep-tissue optical imaging is severely limited by light scattering, which deteriorates the imaging depth, tissue contrast, and resolution. Here, we propose optical coherence projection tomography (OCPT) as a novel three-dimensional (3D) optical imaging technique for deep-tissue imaging. OCPT creates high-resolution images in deep tissue using ballistic photons by combining sensitive heterodyne detection based on optical coherence tomography with suppression of scattered light using a combination of confocal gating, coherence gating, and time gating. In OCPT many transmission measurement are combined using computed tomography to create quantitative 3D images of both the optical attenuation coefficient and the group refractive index of the sample. We demonstrate label-free quantitative OCPT imaging of scattering tissue phantoms and a full adult zebrafish achieving an unprecedented imaging depth of 4 mm in tissue, 27 mean free paths of photon transport in biological tissue without optical clearing.

4.1. INTRODUCTION

Preventing light scattering in biological tissue from degrading the optical imaging depth, tissue contrast, and spatial resolution has been a significant scientific challenge. To tackle this problem various techniques have been developed that either aim to reduce the amount of light scattering, for example through optical tissue clearing [1, 2] or using long wavelength multi-photon imaging [3–5], or aim at reducing the (multiple) scattered light collection efficiency, for example through confocal detection [6], gating based on coherence of the collected photons [7], gating based on photon arrival times [8, 9], or decoupling illumination and detection [10, 11].

One of the most successful approaches for imaging in turbid media is optical coherence tomography (OCT) [12, 13], which is efficient in the suppression of scattered light by combining spatial confocal gating with selection based on the temporal coherence of the collected photons (coherence gating). As a result, OCT is (mainly) based on photons that travel in straight paths through the sample, i.e., ballistic photons. Based on this linear propagation, OCT images are simple to reconstruct and their quality is robust against variations in tissue composition. OCT imaging in tissue is limited to a depth of approximately 1 mm in tissue, approximately 7 photon mean free paths (MFPs; see section 4.2.2).

In the assessment of achieving the ultimate imaging depth, the optical path length trough the object is a crucial parameter since the number of ballistic photons decays exponentially with the path length through the object. Hence, in transmission a ballistic signal with a similar strength probes a twice as thick sample as in reflection. In addition, in transmission OCT there is no signal loss due to the limited collection numerical aperture (NA) of (back) scattered light. Moreover, the optical path length distribution (OPLD) measured in transmission OCT is free from the ambiguity of path length and reflection depth that is present in OCT imaging of dense scattering media [14]. Consequently, in transmission OCT ballistic photons can be selected and separated from multiple scattered light up to a coherence length in path length difference [15, 16]. In this way the ballistic imaging depth can be improved significantly by performing OCT in transmission. A disadvantage of transmission OCT imaging is that no direct 3D spatial information is present in the measured signals. Instead, path length integrated measurements of spatially varying optical properties have to be processed using computed tomography to reconstruct 3D images.

Several optical transmission-based techniques have been reported using either time-gating or confocal gating [17–20]. Some techniques focus only on group refractive imaging of transparent phantom samples [17, 18]. Othes allow attenuation-based imaging of turbid materials but are not quantitative [19] or do not use ballistic light selection for high-resolution imaging [20]. Hence, the applied gating techniques for transmission imaging are not used to their full potential.

Here, we present optical coherence projection tomography (OCPT) as an optical imaging modality for deep-tissue quantitative imaging of turbid objects. OCPT is based on the detection of (near) ballistic photons by using sensitive heterodyne path length resolved detection of transmitted light.

In this work we show that the combination of spatial and temporal gating is essential for deep-tissue optical tomography. We demonstrate the detection of ballistic transmis-

sion through a depth of 4 mm in tissue, corresponding to 27 mean free paths (MFP), without the use of optical clearing. This pushes ballistic imaging to its fundamental SNR-based limit and demonstrates a significant increase in imaging depth compared to current state of the art [21]. Through tissue phantom experiments we show that the spatial imaging resolution in OCPT is not deteriorated by the presence of light scattering. Moreover, OCPT allows for label-free imaging of both optical attenuation and group refractive index tissue contrast. Finally, we demonstrate the full functionality of OCPT with the high resolution deep-tissue 3D quantitative imaging of an adult zebrafish and its application to quantitative 3D tissue analysis.

4.2. THEORY

4.2.1. PRINCIPLE

The general concept of OCPT is depicted in Fig. 4.1(a)-(d). In OCPT many transmission OCT measurements are made from various lateral offsets and angles. Signals from (near) ballistic photons are isolated from the path-length resolved transmission OCT measurements of all transmitted light and used for tomographic image reconstruction of the 3D group refractive index, n_g, and attenuation coefficient, μ_t, distributions in the sample.

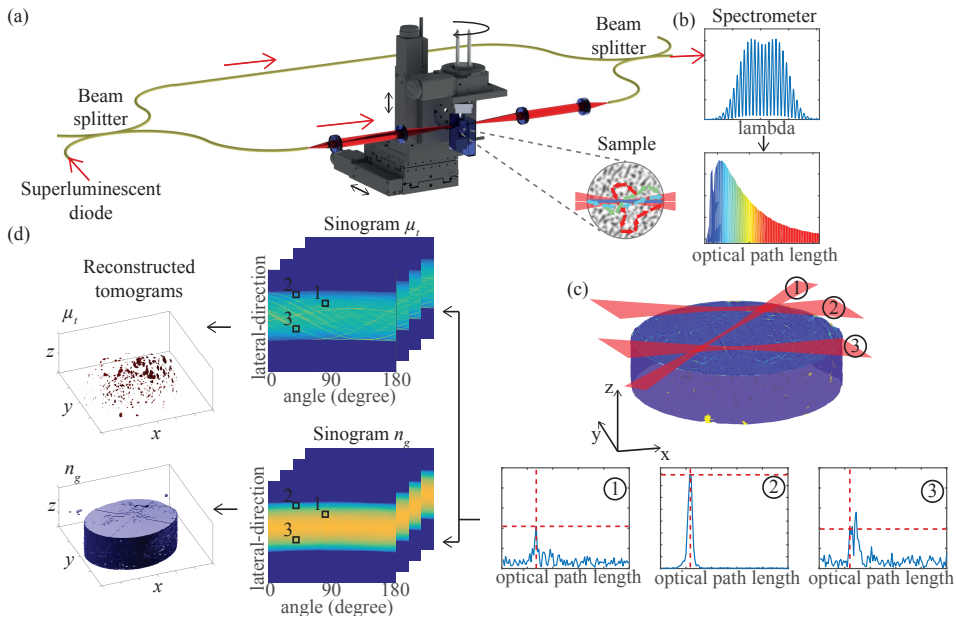

Figure 4.1: The general principle of OCPT imaging. (a) Fiber-based spectral domain transmission OCT system. (b) Optical path length distributions are computed from the measured interference spectra. Based on the measured OPLDs the signal from ballistic photons is selected and used for imaging. (c) Many transmission measurements are taken from different lateral positions and angles. For each measurement an OPLD is computed and the height and location of the ballistic signal is analyzed and ordered into sinograms for the attenuation coefficient and the group refractive index. 3D images of these optical properties are reconstructed from the sinograms (d).

We employ a fiber-based spectral domain transmission OCT system operating at a center wavelength of 1300 nm (see section 4.3.1 and Fig. 4.2). Light from the sample arm of a Mach-Zehnder interferometer is focused in the sample and transmitted photons are collected with a lens and coupled into a single-mode fiber. The collected light is combined with light from the reference arm and the resulting interference pattern is measured on a spectrometer. From the interference spectrum, the OPLD of the light transmitted by the sample is calculated through an inverse Fourier transform.

Ballistic photons that travel straight through the object accumulate the shortest optical path and create a sharp peak in the OPLD, Fig. 4.1(b). Photons scattered in the sample travel longer distances and those that are detected appear as a distribution with longer pathlengths than the ballistic peak in the OPLD. By selecting the signal corresponding to light that travels the shortest optical path, only (near) ballistic photons are filtered from the total light transmission through the sample. Relative to an empty sample arm, the height and location of the ballistic peak are a measure of the path length integrated attenuation coefficient and group refractive index of the sample, respectively.

Transmission OCT is a point scanning technique and no direct 3D spatial information is available as the measurements only give path length integrated optical properties of the sample. By moving the object and recording many transmission OCT measurements from different angles and lateral shifts 3D images of the optical properties can be reconstructed, see Fig. 4.1(c)-(d). The collected ballistic transmission peak heights and peak positions are ordered in two separate sinograms that are reconstructed independently using the algebraic reconstruction technique (ART) [22] (see section 4.3.2 for a detailed description of the setup and the signal processing steps).

4.2.2. OCPT IMAGING DEPTH

For optical imaging techniques the imaging depth increases with increasing sensitivity and stronger rejection of scattered light. The precise trade-offs between these two parameters and the sample properties makes it complicated to determine the exact imaging depth a priori [23].

OCPT is strongly related to OCT. In OCT the imaging depth is dependent on the sensitivity and the properties of the sample. The maximum imaging depth is defined as the number of mean free path lengths of photon transport for which the signal to noise ratio (SNR) becomes 1. The SNR defined as SNR= $10\log(P_0/P_{noise})$, where P_0 and P_{noise} are the signal and noise powers respectively. The maximum imaging depth for a backscatter-based OCT system is given by

$$z_{\mathrm{OCT}} = \frac{1}{2}\left[\ln(l_s p_{NA}\mu_s) + \frac{\mathrm{SNR_{dB}}}{10}\ln 10\right], \tag{4.1}$$

where l_s is the coherence length of the OCT system, $p_{\mathrm{NA}} \approx 4\cdot 10^{-5}$ is the scattering phase function integrated over the collection numerical aperture (NA) of the imaging system lens, and μ_s is the scattering coefficient of the sample [24]. The first term in Eq.(4.1) describes that only a fraction of the scattered light is scattered in the backward direction limiting the signal received by a backscatter-based OCT system. For a system with coherence length l_s = 10 µm, SNR = 116 dB, and μ_s = 4 mm^{-1} this results in a maximum imaging depth z_{OCT} = 7 MFP. Performing OCT in transmission, as is the case in OCPT,

eliminates the first term in Eq.4.1 since all transmitted light is detected. Moreover, due to the absence of a return path through the sample also the factor 1/2 is absent. Hence, the transmission OCT imaging depth is

$$z_{\mathrm{tOCT}} = \left[\frac{\mathrm{SNR_{dB}}}{10} \ln 10 \right], \tag{4.2}$$

which is approximately equal to the OCPT imaging depth z_{OCPT}. Consequently, transmission OCT has an increased imaging depth compared to conventional backscatter-based OCT. For a transmission OCT system with a sensitivity of 116 dB the maximum imaging depth would be $z_{\mathrm{tOCT}} = 27$ MFP, which is almost a factor 4 larger than the imaging depth computed for backscatter-based OCT. For tomographic imaging of a homogeneous sample, the OCPT imaging depth equals that of transmission OCT $z_{\mathrm{OCPT}} = z_{\mathrm{tOCT}}$. For heterogeneous samples the imaging depth is more complex to calculate and Eq. 4.2 can be considered as an approximation. Moreover, compared to backscatter-based OCT the image contrast is better due to the absence of path length ambiguity of multiple scattered optical paths mapping onto shallower depths [14].

The ability of OCPT to reject scattered light in the image formation relies on the combination of confocal gating, coherence gating, and time gating. The ratio of detected ballistic to diffuse power for a transmission confocal system is given by [23]

$$R_{bd} = \frac{\pi L^2}{2\lambda^2} \mu_s (1-g) L \exp(-\mu_s L), \tag{4.3}$$

where L is the sample thickness, g the scattering anisotropy, and λ the light wavelength. Based on Eq. 4.3, using the same parameters as used above, $\lambda = 1300$ nm, and taking a typical value of $g = 0.9$ in tissue the detected ballistic power equals the scattered light power for a transmission confocal system at $L = 17.2$ MFP. An increase to 21.5 MFP has been measured in transmission confocal system with a narrow bandwidth heterodyne detection [23]. Considering the sensitivity limit $z_{\mathrm{OCPT}} = 27$ MFP of our OCPT system, only confocal gating would not sufficiently reject scattered light to guarantee ballistic imaging. Consequently, the coherence and time gating applied in OCPT are essential to sufficiently reject scattered light in the imaging.

4.2.3. IMAGE RESOLUTION

As OCPT imaging is entirely based on ballistic light the resolution is not affected by scattering in the sample, but instead is determined solely by the imaging system specifications. The spatial resolution of the OCPT system depends on the entire through-focus PSF of the confocal lens system and is a function of distance from the center of rotation. The resolution of OCPT images is anisotropic, and varies with position in the image and is caused by the limited depth of field of the imaging system, and has been studied extensively for optical projection tomography (OPT). In our measurements, the optical focus coincides with the center of rotation. Hence, objects at the center of rotation are in focus for every projection angle creating an isotropic image PSF with a full width at half maximum (FWHM) size equal to the beam waist in focus. Objects at locations away from the center of rotation are periodically in focus and out of focus depending on the projection angle. For these locations the image PSF is elongated in the tangential direction. The

OCPT resolution in the tangential and radial direction is well described by the 2D model for OPT [25].

Consider the intensity distribution $I(r,s)$ of a focused Gaussian beam described by

$$I(r,s) = \frac{2}{\pi w^2(s)} \exp\left(-\frac{2r^2}{w^2(s)}\right), \tag{4.4}$$

where r is the radial distance from the optical axis, and $w(s)$ is the beam waist through focus, given by

$$w(s) = \sqrt{w_0^2 + \frac{\lambda^2 s^2}{\pi^2 w_0^2}}, \tag{4.5}$$

with λ the emission wavelength of the fluorophore and w_0 the Gaussian beam waist defined as the e^{-1} value of the field amplitude in focus [26].

In OPT, the spatial point spread function PSF in the tomographic images caused by the imaging optics is given by

$$PSF(u,v) = \sqrt{\frac{1}{\pi^2 a_u a_v}} \exp\left(-\left[\frac{u^2}{a_u} + \frac{v^2}{a_v}\right]\right). \tag{4.6}$$

where (u,v) is a rotated and translated coordinate system, as shown in Fig 4.5(a), with axes along the local radial (u) and tangential (v) directions. The Gaussian widths $a_u = w^2(0)/2$ and $a_v = w^2(s)$ are related to the through focus beam waist $w(s)$. For every object position (x_o, y_o) in the image (u,v) is given by

$$\begin{bmatrix} u \\ v \end{bmatrix} = \begin{bmatrix} \cos(-\theta_o) & -\sin(-\theta_o) \\ \sin(-\theta_o) & \cos(-\theta_o) \end{bmatrix} \begin{bmatrix} x - x_o \\ y - y_o \end{bmatrix}, \tag{4.7}$$

where $\theta_o = \tan^{-1} y_0/x_0$.

In OCPT, the projection data are pre-processed using Eq. and before reconstruction, causing a change in the resolution of the processed sinograms compared to an OPT system with the same optical system. Consequently, the image resolution in the reconstructed tomographic images differs between an OCPT and an OPT system using the same optical system. Here, we process both the reference measurement of $I(r,s)$, and the tomographic experimental data in the same way to determine the accuracy of the model for OCPT.

4.3. METHODS

4.3.1. EXPERIMENTAL SETUP

The OCPT setup is a fiber-based transmission spectral-domain OCT setup, as shown in Fig. 4.1(a), and, in more detail, in Fig. 4.2. Light from a super-luminescent diode (D-1300-HP, Superlum), with a center wavelength of 1300 nm and a bandwidth of 110 nm is coupled into a Mach-Zehnder interferometer based on two 90/10 fiber-optic couplers (TW1300R2A2, Thorlabs). Light in the sample arm is focused onto the sample with a 100 mm focal distance lens (AC254-100-C-ML, Thorlabs), where it interacts with

the measured object before being collimated with a second 100 mm lens and recombined with a reference beam. Detection is performed using a home build spectrometer based on a holographic grating (1145 l/mm, Wasatch Photonics), an SWIR imaging lens (S5LPJ0037/360, Sill Optics), and a 76 kHz InGaAs linescan camera (GL2048L, Sensors Unlimited). An optical amplifier (BOA11323S, Thorlabs) is placed in the sample arm to increase the optical power on the sample to a maximum of 100 mW. The polarization of both arms is controlled using two fiber polarization controllers (FPC560, Thorlabs). The spectrometer data is transferred to the computer via a framegrabber (PCIe-1433, National Instruments). The spectrometer camera is triggered by the stage controller and the entire system is operated by custom Labview software. The transmission OCT setup has a lateral FWHM resolution of 20 µm measured in water, a sensitivity of −116 dB and an axial resolution of 29 µm (in air). The sample is rotated and translated with a motorized sample holder to obtain projection data of the entire object under different angles and lateral offsets, as required for tomographic reconstruction of slices of the measured object.

The sample holder consist of 3 linear stepper motors (8MT167-25LS, Standa) and a stepper motor for rotation (8MR151-30, Standa). The stepper motor stage assembly is controlled using a 4 axis stage controller (Tango Desktop, Marzhauser). A sample is mounted right below the rotation stage using a 16 mm cage system that provides manual tip-tilt and x, y translation for fine alignment of the sample with respect to the rotation axis. The system is aligned so that the center of rotation coincides with the focal point of the sample arm lenses and with the center of the sample. The sample is glued to the cage system and immersed into a $10 \times 50 \times 50$ optical glass cuvette (HELL700000-10-10, VWR) filled with a refractive index matched fluid to reduce refraction effects.

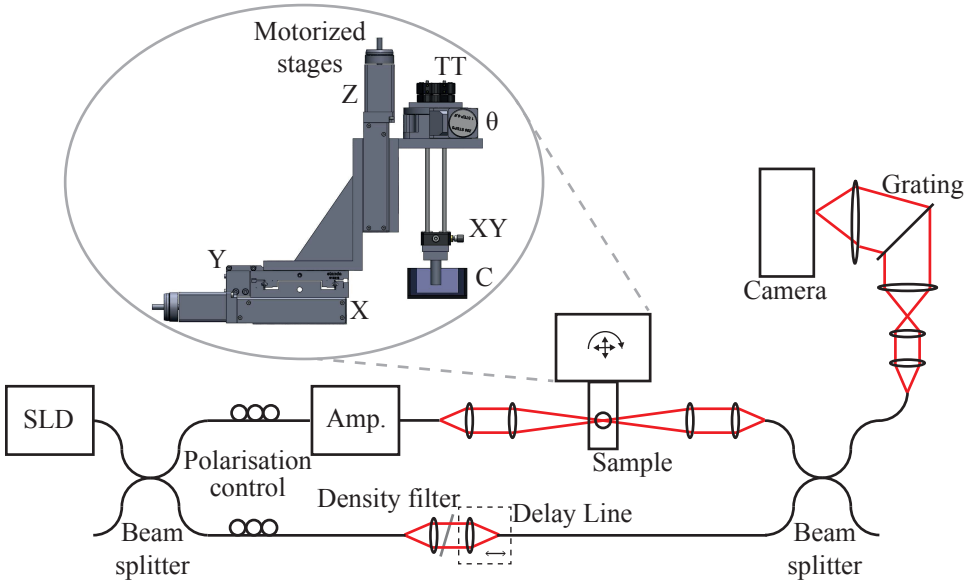

Figure 4.2: Schematic representation of the OCPT setup.

4.3.2. DATA PROCESSING AND IMAGE RECONSTRUCTION

After acquisition the experimental data is stored in raw binary format. Data is processed using software written in MATLAB (Mathworks, R2014b). The data analysis steps are depicted in Fig. 4.1(a)-(d). The transmission OCT signal as a function of optical path length is calculated from the recorded spectra using standard OCT signal processing [15, 16]. The background spectrum of the reference arm is subtracted from the measured interference signal and the resulting spectrum is corrected for dispersion mismatch and nonlinear sampling of the spectrum in the spectrometer [27]. Finally, the OPLD is calculated by taking the absolute value of the inverse Fourier transform of the corrected spectrum.

Scattered light is suppressed in the data analysis by selecting only early arriving photons from the OPLD. The first rising edge in the OPLD is detected by locating the first value higher than three times the standard deviation σ of the noise floor in a region of interest, as shown in Fig. 4.3(c). The region of interest is set prior to the analysis based on the size and estimated refractive index of the sample. A fit with a Gaussian function is initialized with 10 pixels around the rising edge. The location and height of the fitted Gaussians are used as measures for the path length integrated group refractive index and the total attenuation accumulated along the ballistic light path [15, 16].

The large difference in light transmission T between the immersion fluid ($T \approx e^{-1}$) and a highly scattering object ($T \approx e^{-25}$) requires a high dynamic range of the detection setup. Due to the limited dynamic range of the OCPT hardware (38 dB) the setup is optimized for the detection of the small signals originating from the sample. Therefore the spectrometer is saturated when sampling the immersion fluid surrounding and edge regions of the object. Spectrometer saturation is detected in the interference spectra and the corresponding sinogram pixels are set to the values corresponding to the immersion fluid, obtained by separate measurements with the appropriate dynamic range settings.

The calculated path-length integrated attenuation coefficient and group refractive index are placed in two separate sinograms $p_\mu(\theta, t)$ and $p_n(\theta, t)$ using

$$p_\mu(\theta, t) = \int \Delta\mu(s, t)\mathrm{d}s = \delta s \sum_{j=1}^{N} \Delta\mu_j = 2\ln\left(\frac{a_{ref}}{a_{samp}}\right), \tag{4.8}$$

and

$$p_n(\theta, t) = \int \Delta n(s, t)\mathrm{d}s = \delta s \sum_{j=1}^{N} \Delta n_j = b_{samp} - b_{ref}. \tag{4.9}$$

Where δs describes the voxel size in the s direction (along the ray path), t is the lateral coordinate, θ the projection angle, a_{samp} is the peak height determined from a Gaussian fit, b_{samp} is the location of the detected peak, and a_{ref} and b_{ref} are reference values obtained by performing a reference measurement of a cuvette filled with immersion fluid.

The problem of reconstructing images from the collection of path-length integrated values $p_\mu(\theta, t)$ and $p_n(\theta, t)$ is the same as for X-ray computed tomography (CT), provided that the depth of field of the transmission OCT system is comparable or larger than the object size [25]. Initially, the sinograms are filtered to remove outliers that cause streak artifacts in the reconstructed images. When a sinogram pixel deviates more than 15 % from the average of its 8 surrounding pixels it is replaced by the median value of these

surrounding pixels. After correction of the sinograms for center of rotation offsets, quantitative maps of the optical properties relative to the index matching fluid are reconstructed using filtered backprojection (FBP) or the algebraic reconstruction technique (ART) [22]. The ART reconstruction uses a randomized projection order, and executes 4 iterations over all the projections. During the ART reconstruction of the attenuation image a positivity constraint is imposed. Reconstruction using ART takes approximately 18 seconds per slice. Finally, the absolute value of the group refractive indices and attenuation coefficients are calculated by adding an offset from a reference transmission OCT measurement of the surrounding medium. Visualizations in 3D are created using an intensity threshold and opacity settings in ImageJ software package.

By applying different data analysis steps to the same OCPT data set three different reconstructions can be obtained: a solely confocal gated attenuation image, a confocal plus coherence gated attenuation image, and an OCPT image. This allows the study of the improvements achieved by the separate gating techniques.

From the transmission OCT spectrum $S(k_j)$ the confocal only transmission signal is determined by subtraction of the reference arm spectrum S_{ref} and integration of the remaining intensity (the interference contribution cancels). From this transmission signal the projections of the attenuation are determined and a tomographic image is reconstructed with ART. The confocal only sinogram is given by

$$p_{\mu\text{conf}}(\theta, t) = \ln \frac{\sum S_{\text{bg}}(k_j)}{\sum S(k_j) - \sum S_{\text{ref}}(k_j)}, \tag{4.10}$$

where S_{bg} is the sample arm transmission spectrum of the background (index matching) medium. Reference arm and sample arm spectra are recorded separately by blocking of the opposite interferometer arm. The sum in Eq. 4.10 extends over all pixels j of the spectrometer and effectively filters out the high frequency interference signal from the remaining sample arm transmission spectrum, as shown in Fig. 4.3(a). The sinogram $p_{\mu\text{conf}}$ is reconstructed in the same way as the OCPT sinograms. As the confocal gated reconstructed image is created without making use of the interference signal, this image does not profit from the heterodyne detection, the coherence gate, and the time gate.

A confocal and coherence gated attenuation image is made by omitting the time gating, the analysis of the ballistic beak in the OPLD, in the OCPT signal processing. The recorded OPLDs are integrated over a region of 2 mm starting right before the ballistic signal, as shown in Fig. 4.3(b). The confocal and coherence gated sinogram is computed using

$$p_{\mu\text{conf+coh}}(\theta, t) = 2\ln\left(\frac{|\sum a_{ref,i}(z)|}{|\sum a_{samp,i}(z)|}\right), \tag{4.11}$$

with $a_{ref,i}(z)$ and $a_{samp,i}(z)$ the OCT signals of a reference measurement and a measurement with a sample. The sum is taken over the pixels i in the OPLD in the described 2 mm region. Again, tomographic images are reconstructed in the same manner as before.

4.3.3. IMAGE SEGMENTATION

The segmentation of the zebrafish organs is based on the assumption that neighboring pixels have a similar attenuation coefficient and/or refractive index. The zebrafish

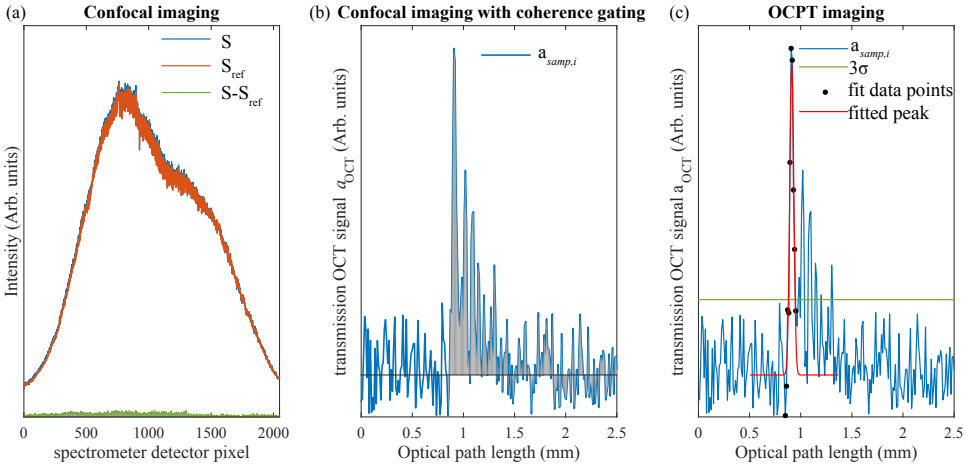

Figure 4.3: Overview of the analysis of the raw data to create sinograms. (a) Analysis of the recorded interference spectra to create confocal gated tomographic images. (b) Analysis of the OPLD to create a confocal and coherence gated tomographic image. (c) Analysis of the OPLD to create confocal gated, coherence gated, and time gated OCPT images.

organs are segmented using several standard methods, applied to either the refractive index image, the attenuation image or to both images. The segmentation of the skin surface is performed by thresholding the attenuation image using the threshold $\mu = 5$ mm^{-1}. The swim bladder is segmented by thresholding the refractive index image using the threshold $n_g = 1.35$. The eye lens is segmented using region growing with a maximum distance of 0.1 mm. The brain is segmented by hand. The spine is segmented by successive application of spatial averaging, *k*-means clustering on the combined μ and n_g images (MATLAB function *kmeans*), image erosion and dilation and a Hough transform to select cylindrical shaped structures. (MATLAB function *circlehough*).

The region growing algorithm is publicly available at MathWorks file exchange [28]. For the estimation of the optical properties values, the MATLAB build-in function *median* was used. The volumes are determined by the *regionprops* with the additional property *Area*. All the areas, which are estimated by the number of pixels, are summed for all slices and then multiplied by the voxel volume 9 pL.

4.3.4. PHANTOM IMAGING

Silicone phantoms were created by mixing and curing Sylgard (Sylgard 184 elastomer kit, Dow Corning) in a cylindrical container. Before curing, titanium dioxide (Titanium(IV) oxide anatase, Aldrich) was added to the solution, to create scattering centers in the material [29]. The sample was immersed in a cuvette filled with index matching 48% sugar water solution to minimize refraction along the light path. The phantom material was measured in 64 axial slices spaced 8 µm apart. Each slice was measured with 1000 lateral sampling points covering 8 mm, and 180 angular projections with a sampling distance of 1°. The total acquisition time was approximately 7 hours. In the angular direction the acquisition was undersampled to limit the total acquisition time.

Validation measurements of the quantitative image contrast were performed using a 2% low melting point agarose (VWR) cylinder immersed in dilutions of Intralipid with water (Intralipid 20 %, Fresenius Kabi). For each concentration 1 axial slice was reconstructed using 1000 lateral measurements covering 8 mm and 180 angular projections with a 1° spacing. The optical properties were determined by averaging a region of interest of 100 by 100 pixels. The results were compared with single transmission OCT measurements of the bulk Intralipid-water mixtures and the agarose.

4.3.5. ZEBRAFISH IMAGING

Experiments were performed on adult zebrafish mounted in 2% low melting point agarose gel. Before fixation in agarose, the zebrafish were euthanized in ice water in the Erasmus University Medical Center Rotterdam (Erasmus MC) according to animal welfare regulations. Animal experiments were approved by the Animal Experimentation Committee of the Erasmus MC. The agarose was encased in a tube of 4 mm inner diameter. The tube was made of fluorinated ethylene propylene (FEP), which has a refractive index close to that of water. The FEP tube containing the agarose and the zebrafish was attached to the sample holder assembly. The zebrafish sample was immersed in a cuvette filled with water to minimize differences in refractive index along the light path. A total of 140 axial slices were recorded, uniformly spaced over a 20 mm range. The lateral and angular sampling was the same as presented for the phantom experiments. The 3D volume was acquired in 14 hours during which 96 GB of raw data was acquired.

4.4. RESULTS

4.4.1. OCPT IMAGING OF TISSUE PHANTOMS

In Fig. 4.4 we demonstrate quantitative OCPT imaging with a measurement of a silicone phantom doped with titanium dioxide (see Methods). The cylindrical phantom has a diameter of approximately 4 mm a mean attenuation coefficient of $\mu_t = 1.3 \pm 0.8$ mm^{-1} and a mean group refractive index of $n_g = 1.463 \pm 0.001$.

Sinograms for μ_t and n_g are shown in Fig. 4.4(a) and 4.4(b), respectively. Clear differences can be observed between the sinograms of the two modes of contrast. These differences are also clearly visible in the reconstructed 2D slices, as shown in Fig 4.4(c) and 4.4(d). The attenuation coefficient image shows the structure of the object and many strongly scattering clusters of titanium dioxide. The refractive index image shows a homogeneous refractive index within the phantom. Some of the larger clusters of titanium dioxide are also visible in the refractive index image. The 3D image of the sample attenuation coefficient is visualized using a false color representation in Fig. 4.4(e). The figure shows the 3D spatial distribution of the titanium clusters through the sample volume.

4.4.2. OCPT IMAGE RESOLUTION

The tomographic image resolution is determined experimentally from the images of the individual titanium dioxide clusters in the Sylgard phantom. The titanium dioxide clusters, previously reported as having a mean diameter of 730 ± 600 nm [29], can be considered point objects for OCPT. Their image in the tomographic reconstruction is characterized by the FWHM in the radial, tangential, and vertical directions. First, the PSF $I(r, s)$

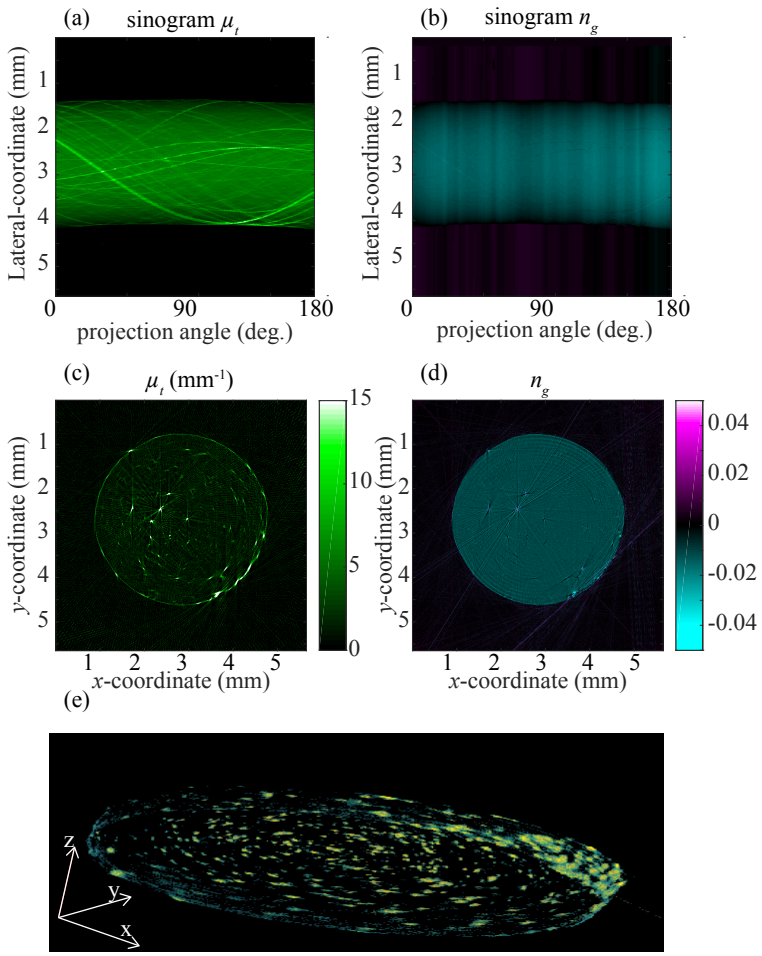

Figure 4.4: OCPT measurement of a scattering silicone phantom. Sinograms for the attenuation coefficient μ_t (a) and group refractive index n_g (b) for a single slice. Reconstructed quantitative images of the attenuation coefficient (c) and group refractive index (d). (e) False colored 3D representation of the attenuation coefficient of the sample. Figure created using a maximum intensity projection of the thresholded volume.

of the confocal lens system is measured at several positions from focus using a knife edge. Second, the though-focus FWHM of the beam waist is determined after performing the typical processing required for quantitative tomography, described in equation 4.8. In the tomographic image, clusters of titanium dioxide in the 3D volume are located and fitted with a bivariate Gaussian model across the volume. The FWHM spotsizes in the radial, tangential, and vertical directions are determined from the Gaussian fits and shown in Fig. 4.5(b).

Our analysis shows an isotropic 20 µm FWHM resolution at the center of the image, which is equal to the in-focus beam waist of the confocal lens system. The resolution in the tangential direction increases with the radial distance from the center of rotation following the though-focus beam waist of the lens system. At 1 mm from the center, the resolution in the tangential direction degrades to 36 µm. In the center of rotation the resolution in the vertical direction is the same as the in-focus beamwaist. For larger distances from the center of rotation the vertical resolution becomes smaller. This effect is attributed to 3D effects of combining in-focus and out-of-focus projection data in the tomographic reconstruction. Fitting the measured tangential and radial FWHM spot sizes from OCPT with the 2D OPT model from Eq. 4.6 gives $w_0 = (17.33 \pm 0.42)$ µm and $\lambda = (1613 \pm 120)$ nm. This is consistent with the parameters obtained from a separate OCPT processed knife-edge measurement of optical beam profile in the index matching fluid ($w_0 = (14.92 \pm 3.17)$ µm and $\lambda = (1272 \pm 339)$ nm). While these parameters do not describe the physical light intensity distribution in the confocal imaging system of the sample arm, they show the consistency of the knife edge measurement with the measured image resolution.

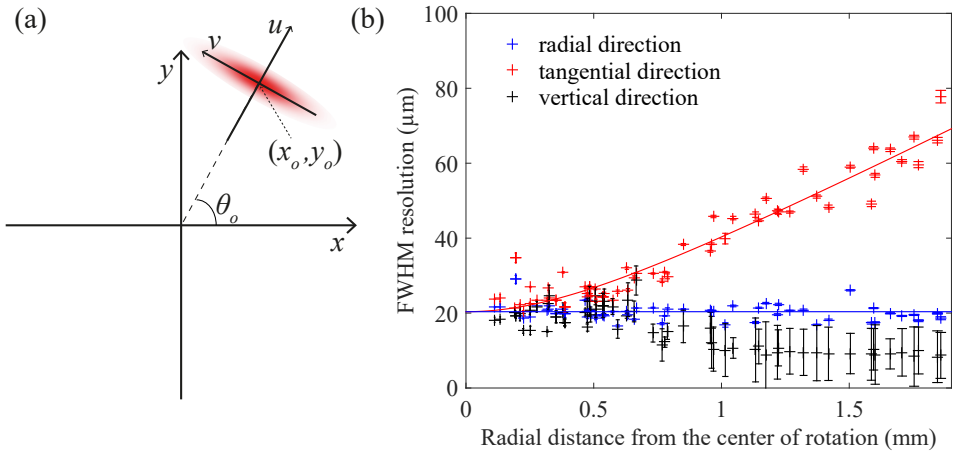

Figure 4.5: OCPT spatial resolution of characterization. (a) Definition of coordinate systems in the image plane. (b) FWHM resolution in the radial (blue points), tangential (red points), and vertical (black points) direction as a function of the radial distance from the center of rotation. Error bars indicate 95% confidence intervals. The in-focus beam waist (blue line) and though-focus beam waist (red line) predicting the radial and tangential resolutions respectively are plotted for comparison.

4.4.3. VALIDATION OF OCPT QUANTITATIVE IMAGING

The quantitative nature of the reconstructed tomographic images is validated in a series of OCPT imaging experiments with tissue phantoms. An agarose cylinder is imaged while immersed in several concentrations of water-diluted Intralipid, a lipid emulsion widely used in optical experiments to simulate the scattering properties of biological tissues. The addition of Intralipid to water changes both the refractive index as well as the attenuation of the medium. These optical properties of the Intralipid-water mixture are determined in bulk using transmission OCT [16] and compared with the values obtained in the tomographic images. Both values are in good agreement within the measured range of Intralipid concentrations, as shown in Fig. 4.6.

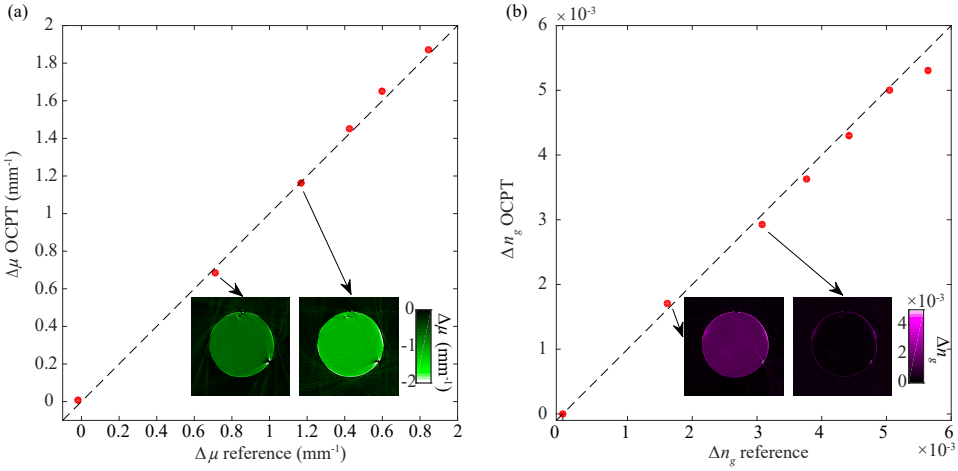

Figure 4.6: Validation of OCPT quantitative imaging. The attenuation coefficient (a) and group refractive index (b) determined from the tomographic OCPT images versus their corresponding reference values measured with transmission OCT. Errors associated with measurements are smaller than the marker size.

4.4.4. OCPT IMAGING OF ADULT ZEBRAFISH

Zebrafish larvae are extensively imaged as model animals in medical and biological research due to their easy maintenance, rapid reproduction, and optical transparency. In contrast, adult zebrafish are not as transparent as the larvae and therefore challenging to fully image in 3D at high resolution. We demonstrate that OCPT is capable of imaging an entire 20 mm adult zebrafish with high resolution, something that, to the best of our knowledge, is currently not possible. Experiments are performed on adult zebrafish mounted in low melting point agarose gel (see Methods for further details).

Figure 4.7 shows the full OCPT imaging of an adult zebrafish. Figures 4.7(a)-(c) show transverse cross-sections of the zebrafish attenuation coefficient. Several distinct anatomical features can be recognized such as the eye lens and retina, the swim bladder, and the spine. A false colored 3D visualization of the zebrafish attenuation coefficient is shown in figure 4.7(d), showing the overall structure of the fish. The 3D group refractive index image of the zebrafish is shown in figures 4.7(e)-(h). Again, the axial cross-sections in fig-

ures 4.7(f)-(h) show several anatomical features of the fish. The retina and the gas-filled swim bladder with $n_g = 1$ is clearly visible from the surrounding tissue that has a higher refractive index. The false color 3D visualization Fig. 4.7(e) also clearly shows the spine structure and the brains of the zebrafish.

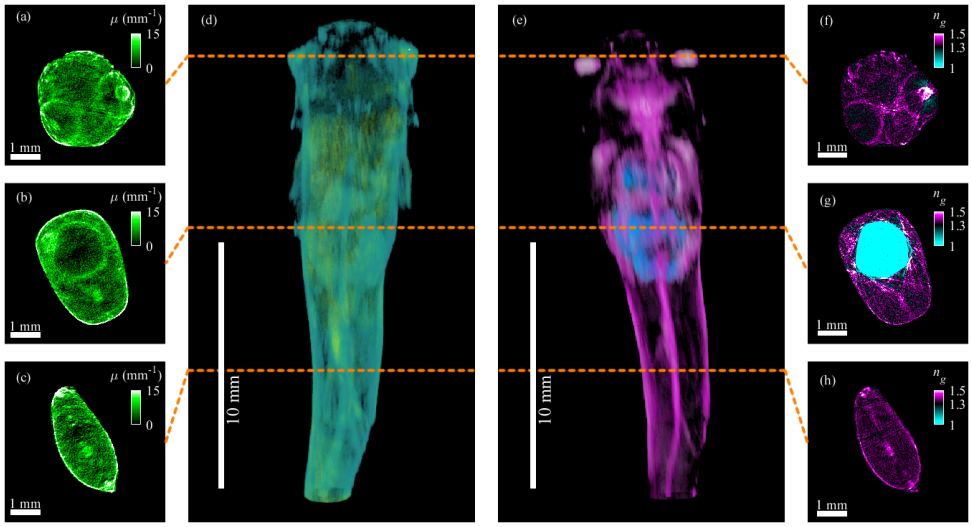

Figure 4.7: OCPT imaging of an adult zebrafish. Reconstructed transverse slices of the absolute attenuation coefficient μ_t [(a)-(c)], and group refractive index n_g [(f)-(h)] of an adult zebrafish. False-colored 3D visualizations for the attenuation coefficient (d) and group refractive index (e).

OCPT images allow quantitative analysis of tissue and organ properties in-toto. Figure 4.8 shows the brains, eyes, skin, spine and swim bladder of the zebrafish segmented with different methods based on OCPT images of the group refractive index or attenuation coefficient, as described in section 4.3.3. From the segmented organs, the volume median optical properties and volume are calculated. This allows for quantitative assessment of tissue development and status at high resolution in an adult zebrafish, something that is unfeasible with current state-of-the-art imaging equipment.

Table 4.1 gives an overview of quantitative OCPT imaging of zebrafish tissue properties. For various zebrafish organs the organ volume, volume median attenuation coefficient, and median group refractive index values are quantified. The values are compared with literature values of similar tissues from other organisms measured with different methods, as far as available. Overall, the organ attenuation coefficients are in good agreement with the values found in literature. The segmented brain is a mixture of grey matter, white matter, and thalamus and the attenuation coefficient is a weighted average of the attenuation coefficients of these tissues. The attenuation of the lens is in a good agreement with the literature value. The attenuation value of the spine is slightly higher than the literature value for spinal fluid. The difference is attributed to the inclusion of spinal bone, which is expected to raise the attenuation coefficient. In the gas bladder, we expect an attenuation of 0 mm^{-1}. The elevated value of the attenuation coefficient occurs primarily in the center of the bladder, which we attribute to incorrectly backpro-

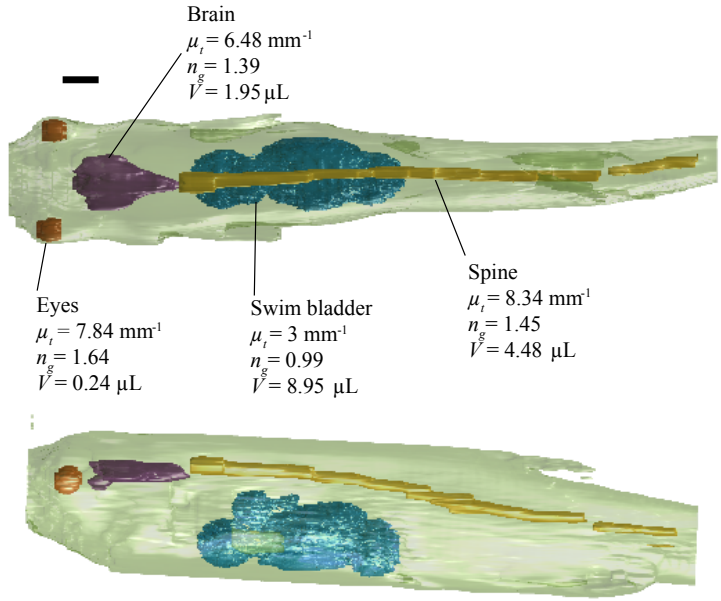

Figure 4.8: Optical properties of zebrafish tissue. Segmentation of multiple zebrafish organs with volume and median optical properties of the eyes, brain, spine, and swim bladder. Scale bar is 1 mm.

Table 4.1: Zebrafish tissue optical properties and organ sizes measured with OCPT. Volume (V), median attenuation (μ_t), and median group refractive index (n_g) values obtained using segmented OCPT measurements compared with literature values. gm: Gray matter, wm: white matter, thala: thalamus.

Organ	V (µL)	μ_t (mm^{-1})	Lit. value μ_t (mm^{-1})	n	Lit. value n_g
Brain	1.95	6.48	gm: 5 ± 3 [30] wm: 10 ± 2 [30] thala: 8 ± 3 [30]	1.39	1.41 ± 0.02 [31]
Lens	0.24	7.84	7 to 9 [32]	1.64	1.55 ± 0.02 [33]
Spine	4.48	8.34	spinal fluid 5 ± 0.7 [30]	1.45	
Gas bladder	8.95	3	0 [34]	0.99	1 [35]

jected values from the high attenuating surrounding to the interior of the gas bladder.

The group refractive index values are in good agreement with values reported in literature. The literature value of the refractive index for the lens [33] was measured at 800 nm. Considering typical dispersive properties of tissue we expect this wavelength dependence to only give deviations of the order of $\Delta n \approx 0.03$ for a wavelength of 800 nm compared to the measured value at 1300 nm [36]. The refractive index of the swim bladder and brain tissue was reported at the wavelength of 1300 nm [31, 35].

4.4.5. OCPT IMAGING DEPTH

To quantitatively analyze the deep-tissue imaging performance the optical thickness $\int \mu_t(x,y,z)\mathrm{d}s$ of the measured object is determined from the attenuation sinogram based on Eq. 4.8. The measured distribution of optical thickness for all the recorded rays gives an indication of the maximum imaging depth of the imaging system. In order to reduce the effects of noise the calculations are performed using a sinogram that is computed from the reconstructed data $\mu(x,y,z)$ using the Radon transform $\mathscr{R}$. The forward projected attenuation sinogram, $p_{\mu\text{forward}}(\theta,t,z) = \mathscr{R}\mu(x,y,z)$, allows us to take into account rays that in principle cannot be measured because of Eq. 4.2, but that are reconstructed based on other rays that travel through the sample.

Another measure to experimentally investigate the imaging depth is by comparing the forward projected attenuation sinogram with the attenuation sinogram obtained directly from the measurements $\Delta p_\mu(\theta,t,z) = |p_{\mu\text{forward}} - p_\mu|$. A deviation of the measured sinogram with the forward projected sinogram means that the ray measurement is not consistent with the overall object reconstructed from all the rays, indicating a measurement error. An estimate of the maximum imaging depth is made by computing how many rays of the forward projected sinogram deviate significantly (> 50%) from the corresponding measured sinogram rays.

The contributions of the confocal gate, coherence gate, and time gate to the imaging depth can be separated experimentally by reconstructing images with different input signals all derived from the same OCPT data set, as described in section 4.3.2. The capability of OCPT to image deep into strongly scattering media is evident by comparison of the different gating techniques on the images, shown in Fig. 4.9.

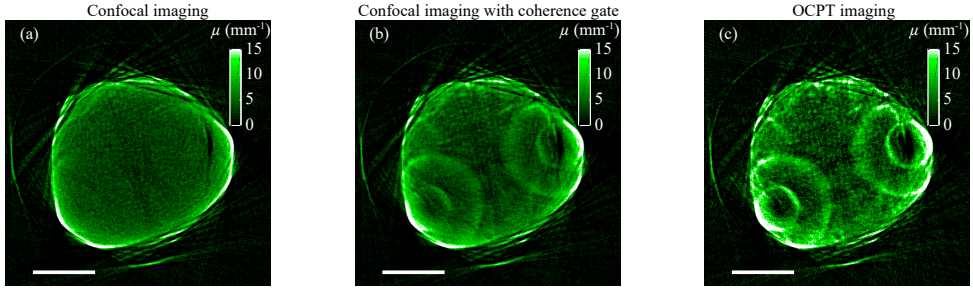

Figure 4.9: Comparison between confocal gated imaging and OCPT. (a), confocal gated image. (b), An image created by a combination between confocal gating and coherence gated imaging. (c), OCPT image made by combining confocal gating, coherence gating, and time gating. Scale bar 1 mm.

A single slice of the reconstructed confocal gated attenuation image of the zebrafish is shown in Fig. 4.9(a). The image clearly shows the outline of the zebrafish but no inner structures are observed in the fish. The MFP distribution of the measured rays for confocal gated tomographic imaging is shown in Fig. 4.10(a). The MFP distribution, terminates in the 15-20 MFP region. In confocal detection some of the scattered light is not rejected causing the detected signals to be higher than expected for ballistic transmission. This results in an underestimation of the attenuation, hence limiting the sampled MFP range. The analysis of inconsistent rays, shown in Fig. 4.10(b), indicates that the

background medium contributes a large number of rays with approximately 0 MFP of optical thickness. Also, a sharp increase in inconsistent rays can be observed at 19 MFP, which is at the end of the confocal gated imaging range. Inconsistencies at low MFPs are mainly caused by detector saturation errors.

A confocal and coherence gated image is obtained by summing over a region of 2 mm in the OPLD starting before the ballistic peak and extending in the multiple scattered path length regime. Light detected in each pixel on the spectrometer that lost coherence with the reference beam will cause a background signal in the spectrum but does not contribute to the interference pattern. The confocal and coherence gated attenuation image, shown in Fig. 4.9(b), shows many more internal structures of the zebrafish. The MFP distribution also shows an increase in rays with a larger optical thickness, indicating a higher sensitivity compared to the confocal gated image, and terminates in the 20-25 MFP range. For the confocal and coherence gated image a sharp increase in inconsistent rays (shown in Fig. 4.10(b)) is observed at 23 MFP, which is at the end of the confocal and coherent gated imaging range. This imaging performance is better than imaging with confocal gating only. For both the confocal gated image and the confocal plus coherence gated image our estimated imaging depth is slightly higher than the value predicted by Eq. 4.3 and stated in literature [23]. We attribute this to the ability of tomographic imaging to deal with missing (no signal) rays in parts of the object that are too thick to generate a transmission signal. The improvement of the image quality of the confocal image with the addition of the coherence gate is attributed to the increase in sensitivity of the system and the improved suppression of scattered light.

OCPT image quality is obtained using the full OCPT signal processing by selection of only the ballistic peak in the OPL distribution. The OCPT attenuation image, shown in Fig. 4.9(c), shows an improvement in image contrast compared to the confocal and coherent gated image. Hence, the addition of the time gate to select only ballistic light from the transmitted light is crucial to achieve high contrast images deep in tissue. The measured attenuation values are higher due to the improved suppression of scattered light. The MFP histogram shows the majority of the rays is within the 27 MFP limit computed for transmission OCT using equation 4.2. A small fraction of the rays show MFP values higher than the systems sensitivity limit. This is attributed to the tomographic reconstruction process in which the volume sampled by rays experiencing large attenuation is measured indirectly by rays propagating from directions that have smaller integrated attenuations. Consequently, the full object is reconstructed, even though it is optically thicker than z_{OCPT} at some angles and lateral positions. Not taking this effect into account, the maximum imaging depth z_{OCPT} is estimated from the measured data by analyzing inconsistencies in the sinogram for the attenuation coefficients. A fast increase of incorrect rays is observed in Fig. 4.10(b) at 27 MFP, the maximum OCPT imaging depth. This depth is in good agreement with the prediction of z_{OCPT} based on Eq. 4.2. Besides the significantly improved contrast, the selection of the ballistic peak also makes it possible to image the refractive index distribution of the sample allowing for multi-modal quantitative contrast.

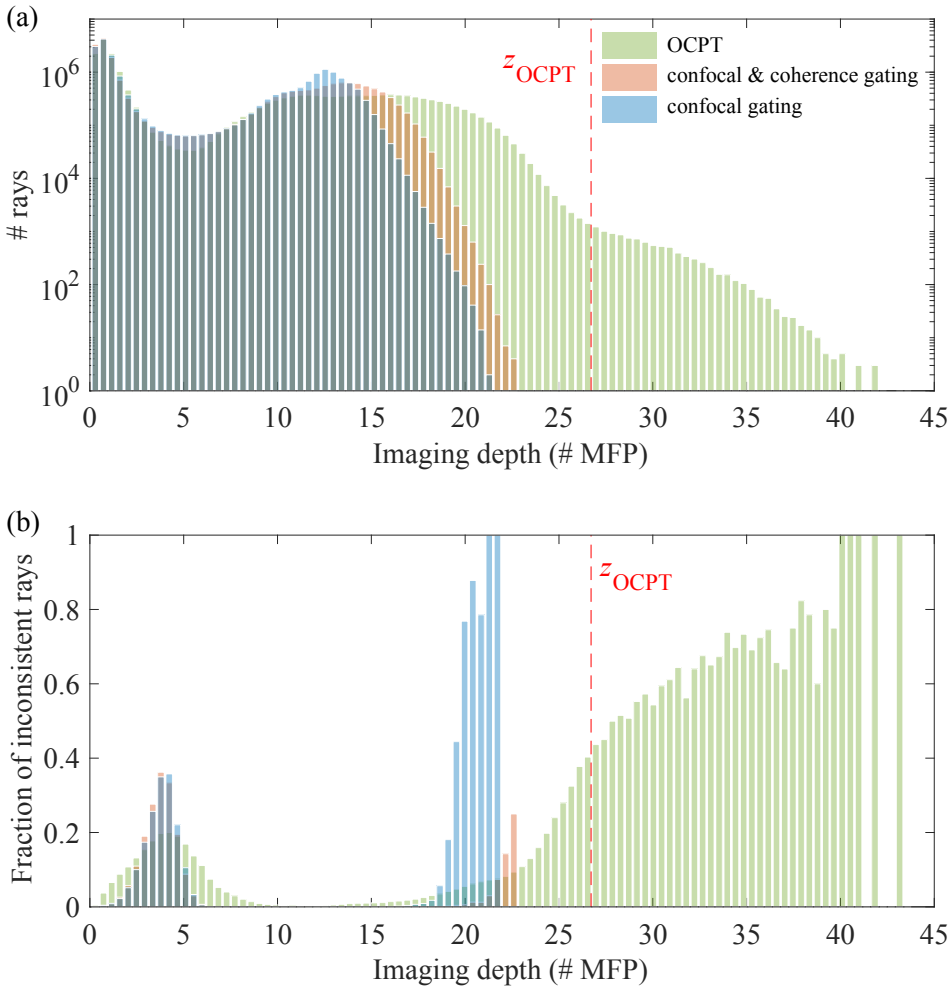

Figure 4.10: Evaluation of the OCPT imaging depth based on the zebrafish data of Fig. 4.7. (a) Histogram of the optical thickness for every computed ray through the measured tissue as a function of the number of MFPs traversed by the ray for OCPT, confocal imaging and confocal imaging with coherence gate. The dashed red line indicates z_{OCPT}. (b) The fraction of rays for which the computed sinogram with path length integrated attenuation coefficients deviates from the directly measured sinogram by more than 50%.

4.4.6. STATIC TIME GATING IN OCPT

By selecting the ballistic signal from the OPLD the time gating performed in OCPT is adjusted for each transmitted ray, optimizing the ballistic detection and the suppression of scattered light. However, to date mostly fixed time gates have been applied to imaging in scattering media [8, 9]. The collection of OPLDs measured with OCPT also can be used to extract a series of fixed time gated attenuation images from a single measurement. Each fixed time gate highlights different areas in the object, providing a versatile range of contrast mechanisms for qualitative tissue assessment and segmentation purposes.

We demonstrate the ability to create variable time gated OCPT images in Fig. 4.11, which shows a set of static time gated images. These time-gated images are computed by integrating the measured intensity in the OPLD within a Gaussian window with a FWHM corresponding to 63 fs travel time in air. The figure shows that different positions of the time gate result in changes in the visible anatomical features. Only with the Fourier-domain implementation of high speed OPLD acquisition in OCPT the adjustment of the time gate does not require any additional acquisition time and can be performed after data acquisition.

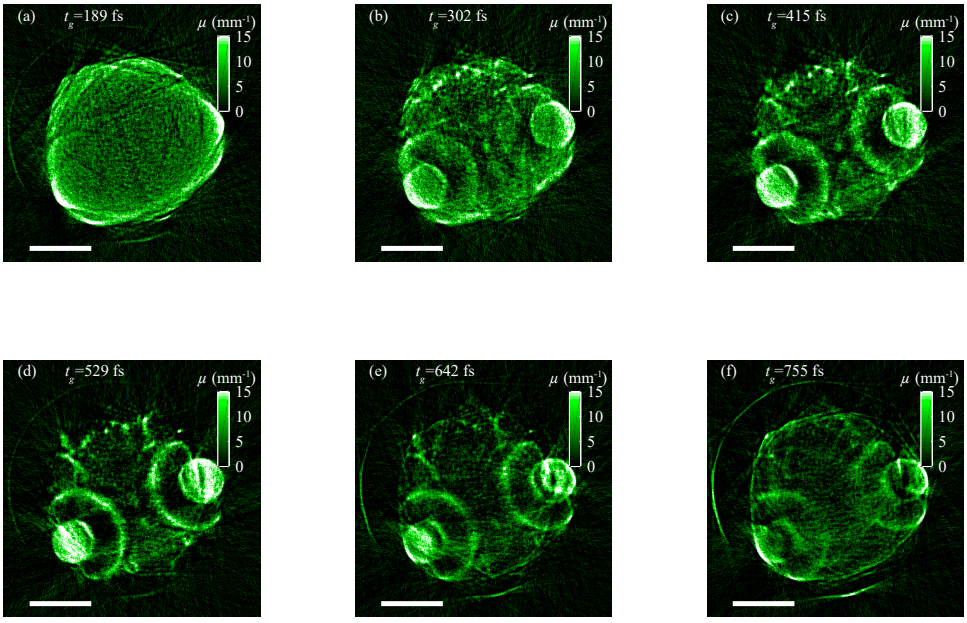

Figure 4.11: Sequence of static time-gated OCPT images. Application of static time gating to the OPLD for several time windows measured with OCPT on zebrafish.

4.5. DISCUSSION

We present OCPT as a novel optical imaging modality for quantitative, label-free 3D deep-tissue imaging. From the measured OPLD, images of both the optical attenuation coefficient and the group refractive index are reconstructed, providing two modes

of quantitative contrast.

The imaging depth of OCTP is related to the sensitivity of the transmission OCT system and the suppression of scattered light. OCPT suppresses scattered light in three ways. First, multiple scattered photons are filtered out since they do not couple efficiently to the single-mode fiber that acts as a collection pinhole (confocal gating). Second, photons that lose their coherence or polarization due to scattering do not contribute to the measured interference signal and are also suppressed in the image formation (coherence gating). Third, the path length selection identifies ballistic photons based on their path length, hence on their arrival time (time gating). As a result of the combined effect of these three gating techniques OCPT discriminates ballistic photons constituting a fraction as small as 10^{-12} of the total amount of scattered light.

Compared to backscatter-based OCT, performing OCT imaging in transmission increases the imaging depth by a factor of two as well as by an additional factor originating from the absence of the limited collection of backscattered light from the OCT sample arm's NA. Moreover, OCPT does not suffer from the ambiguity of depth and path length, which for highly scattering samples can lead to a reduction in contrast. Using parameters typical for tissue and OCT systems, a calculation of the imaging depth yields an improvement of the imaging depth of around 4 times compared to backscatter-based OCT (see section 4.2.2 for the comparison of the OCPT and OCT imaging depth). While for OCT an imaging depth of 7 MFP is possible, for OCPT the imaging depth is extended to 27 MFP. The OCPT imaging depth is also computed directly from the zebrafish measurements and agrees well with the 27 MFP computed from the SNR of the system (see section 4.2.2).

Compared to other existing imaging techniques for turbid media [21, 37], OCPT provides a significant increase in imaging depth due to the combination of gating methods and the use of imaging in transmission geometry. OCPT pushes the ballistic light scattering imaging range to its SNR limited range of 27 MFPs. Since OCPT is based only on ballistic light, it is robust against variations in the sample as reconstructions can be performed based on the known imaging beam geometry.

In OCPT, the measured attenuation coefficient is determined by all losses of the light as it propagates in a straight path through the object: absorption, scattering, and losses due to diffraction and reflections. The transmission geometry is sensitive to refraction effects causing light to change direction and decrease the coupling efficiency into the single-mode fiber at the detection end of the sample. At the outer interface these effects are minimized by immersing the measured object in a refractive-index matched medium. Despite not clearing the sample we still obtain geometrically correct images. However, an overestimation of the scattering coefficient of sample interfaces is currently present in our reconstructions as imperfect matching and refractive index variations inside the sample cannot be completely prevented. Possibly, the matching requirements can be relaxed and the detrimental effects corrected in the future by including a refraction correction in the reconstruction algorithm [38].

OCPT greatly increases imaging depth in tissue, improves contrast, and potentially allows for in-vivo imaging. The 3D measurements presented in this paper required imaging of several hours. These long times are caused by the use of mechanical scanning of the object to acquire the transmission OCT projections. In the current setup, less than

2% of the imaging time is actually used for collecting photons on the detector. Use of rapid beam-scanning techniques and/or limited angle acquisition can significantly improve the imaging speed in the future. Alternatively, an improved acquisition duty cycle can be used to increase the imaging depth by temporal averaging.

The presented method allows for quantitative 3D imaging of turbid objects without the need for optical clearing or labelling. We showed an unprecedented maximum imaging depth of 27 MFP in an adult zebrafish at a resolution determined by the propagation of ballistic photons only. In contrast to wavefront based techniques for deep imaging in turbid media (such as wavefront shaping [39, 40], time reversal [41] and coherent addition [37]), OCPT is not limited by the tissue correlation time or the memory effect, and can be even applied to objects that have sub-resolution movement (e.g. due to blood flow). OCPT is closely related to OCT and can therefore borrow of many of the hardware innovations and methodological advances made in that field. In the future we anticipate an increase in resolution, SNR, and imaging speed so that in-vivo imaging of zebrafish becomes feasible (currently unpractical due to the long imaging time). OCPT provided the first ever quantitative measurements of optical properties of an entire adult zebrafish, thereby opening a broad range of new applications for diagnosis and evaluation in life science and in medicine. The significant leap in imaging depth achieved with OCPT widens the possible range of optical imaging and could benefit the imaging of human biopsy tissues, small animals, embryos, plants, optically cleared larger biological systems like whole mice, and metrology in industry.

REFERENCES

[1] D. Zhu, K. V. Larin, Q. Luo, and V. V. Tuchin, *Recent progress in tissue optical clearing,* Laser & Photonics Rev. **7**, 732 (2013).

[2] J. Sharpe, U. Ahlgren, P. Perry, B. Hill, A. Ross, J. Hecksher-Sørensen, R. Baldock, and D. Davidson, *Optical projection tomography as a tool for 3D microscopy and gene expression studies,* Science **296**, 541 (2002).

[3] W. Denk, J. H. Strickler, W. W. Webb, *et al., Two-photon laser scanning fluorescence microscopy,* Science **248**, 73 (1990).

[4] W. R. Zipfel, R. M. Williams, and W. W. Webb, *Nonlinear magic: multiphoton microscopy in the biosciences,* Nat. Biotechnol. **21**, 1369 (2003).

[5] E. Papagiakoumou, A. Bègue, B. Leshem, O. Schwartz, B. M. Stell, J. Bradley, D. Oron, and V. Emiliani, *Functional patterned multiphoton excitation deep inside scattering tissue,* Nat. Photonics **7**, 274 (2013).

[6] J. Schmitt, A. Knüttel, and M. Yadlowsky, *Confocal microscopy in turbid media,* J. Opt. Soc. Am. **11**, 2226 (1994).

[7] T. H. Nguyen, M. E. Kandel, M. Rubessa, M. B. Wheeler, and G. Popescu, *Gradient light interference microscopy for 3D imaging of unlabeled specimens,* Nat. Commun. **8**, 210 (2017).

[8] G. M. Turner, G. Zacharakis, A. Soubret, J. Ripoll, and V. Ntziachristos, *Complete-angle projection diffuse optical tomography by use of early photons,* Opt. Lett. **30**, 409 (2005).

[9] L. Fieramonti, A. Bassi, E. A. Foglia, A. Pistocchi, C. D'Andrea, G. Valentini, R. Cubeddu, S. De Silvestri, G. Cerullo, and F. Cotelli, *Time-gated optical projection tomography allows visualization of adult zebrafish internal structures,* PLoS One **7**, e50744 (2012).

[10] J. Huisken, J. Swoger, F. Del Bene, J. Wittbrodt, and E. H. Stelzer, *Optical sectioning deep inside live embryos by selective plane illumination microscopy,* Science **305**, 1007 (2004).

[11] P. J. Keller, A. D. Schmidt, J. Wittbrodt, and E. H. Stelzer, *Reconstruction of zebrafish early embryonic development by scanned light sheet microscopy,* Science **322**, 1065 (2008).

[12] D. Huang, E. A. Swanson, C. P. Lin, J. S. Schuman, W. G. Stinson, W. Chang, M. R. Hee, T. Flotte, K. Gregory, C. A. Puliafito, *et al.*, *Optical coherence tomography,* Science **254**, 1178 (1991).

[13] J. A. Izatt, E. A. Swanson, J. G. Fujimoto, M. R. Hee, and G. M. Owen, *Optical coherence microscopy in scattering media,* Opt. Lett. **19**, 590 (1994).

[14] J. Kalkman, A. Bykov, D. Faber, and T. Van Leeuwen, *Multiple and dependent scattering effects in doppler optical coherence tomography,* Opt. Express **18**, 3883 (2010).

[15] V. D. Nguyen, D. Faber, E. van Der Pol, T. van Leeuwen, and J. Kalkman, *Dependent and multiple scattering in transmission and backscattering optical coherence tomography,* Opt. Express **21**, 29145 (2013).

[16] A. Trull, J. van Der Horst, J. Bijster, and J. Kalkman, *Transmission optical coherence tomography based measurement of optical material properties,* Opt. Express **23**, 33550 (2015).

[17] Y. Wang and R. K. Wang, *High-resolution computed tomography of refractive index distribution by transillumination low-coherence interferometry,* Opt. Lett. **35**, 91 (2010).

[18] A. M. Zysk, J. J. Reynolds, D. L. Marks, P. S. Carney, and S. A. Boppart, *Projected index computed tomography,* Opt. Lett. **28**, 701 (2003).

[19] M. R. Hee, E. A. Swanson, J. A. Izatt, J. M. Jacobson, and J. G. Fujimoto, *Femtosecond transillumination optical coherence tomography,* Opt. Lett. **18**, 950 (1993).

[20] L. Li and L. V. Wang, *Optical coherence computed tomography,* Appl. Phys. Lett. **91**, 141107 (2007).

[21] A. Badon, A. C. Boccara, G. Lerosey, M. Fink, and A. Aubry, *Multiple scattering limit in optical microscopy,* Opt. Express **25**, 28914 (2017).

[22] A. C. Kak and M. Slaney, *Principles of computerized tomographic imaging* (SIAM, 2001).

[23] M. Kempe, A. Genack, W. Rudolph, and P. Dorn, *Ballistic and diffuse light detection in confocal and heterodyne imaging systems,* JOSA A **14**, 216 (1997).

[24] V. Kodach, J. Kalkman, D. Faber, and T. G. van Leeuwen, *Quantitative comparison of the OCT imaging depth at 1300 nm and 1600 nm,* Biomed. Opt. Express **1**, 176 (2010).

[25] J. van der Horst and J. Kalkman, *Image resolution and deconvolution in optical tomography,* Opt. Express **24**, 24460 (2016).

[26] H. Kogelnik and T. Li, *Laser beams and resonators,* Proceedings of the IEEE **54**, 1312 (1966).

[27] A. F. Fercher, C. K. Hitzenberger, M. Sticker, R. Zawadzki, B. Karamata, and T. Lasser, *Numerical dispersion compensation for partial coherence interferometry and optical coherence tomography,* Opt. Express **9**, 610 (2001).

[28] D. J. Kroon, *Region growing,* (2008), matlab file exchange, Mathworks, https://nl.mathworks.com/matlabcentral/fileexchange/19084-region-growing.

[29] D. M. de Bruin, R. H. Bremmer, V. M. Kodach, R. de Kinkelder, J. van Marle, T. G. van Leeuwen, and D. J. Faber, *Optical phantoms of varying geometry based on thin building blocks with controlled optical properties,* J. Biomed. Opt. **15**, 025001 (2010).

[30] V. Tuchin, *Tissue optics: Light scattering methods and instruments for medical diagnosis,* SPIE (2007).

[31] J. Sun, S. J. Lee, L. Wu, M. Sarntinoranont, and H. Xie, *Refractive index measurement of acute rat brain tissue slices using optical coherence tomography,* Opt. Express , 1084 (2012).

[32] R. L. Vincelette, A. J. Welch, R. J. Thomas, B. Rockwell, and D. J. Lund, *Thermal lensing in ocular media exposed to continuous-wave near-infrared radiation: The 1150-1350-nm region,* J. Biomed. Opt. (2008).

[33] L. Garner, G. Smith, S. Yao, and R. Augusteyn, *Gradient refractive index of the crystalline lens of the black oreo dory (allocyttus niger): comparison of magnetic resonance imaging (MRI) and laser ray-trace methods,* Vision Research **41**, 973 (2001).

[34] Wikilectures, *Hounsfields units,* wikilectures.eu (checked 16 Oct 2017).

[35] P. Ciddor, *Refractive index of air: new equations for the visible and near infrared,* Appl. Optics (1996).

[36] H. Ding, J. Q. Lu, W. A. Wooden, P. J. Kragel, and X.-H. Hu, *Refractive indices of human skin tissues at eight wavelengths and estimated dispersion relations between 300 and 1600 nm,* Phys. Med. Biol. **51**, 1479 (2006).

[37] S. Kang, S. Jeong, W. Choi, H. Ko, T. D. Yang, J. H. Joo, J.-S. Lee, Y.-S. Lim, Q.-H. Park, and W. Choi, *Imaging deep within a scattering medium using collective accumulation of single-scattered waves,* Nat. Photonics **9**, 253 (2015).

[38] S. J. Doran and D. N. Yatigammana, *Eliminating the need for refractive index matching in optical CT scanners for radiotherapy dosimetry: I. concept and simulations,* Phys. Med. Biol. **57**, 665 (2012).

[39] I. M. Vellekoop and A. Mosk, *Focusing coherent light through opaque strongly scattering media,* Opt. Lett. **32**, 2309 (2007).

[40] A. P. Mosk, A. Lagendijk, G. Lerosey, and M. Fink, *Controlling waves in space and time for imaging and focusing in complex media,* Nat. Photonics **6**, 283 (2012).

[41] P. Lai, L. Wang, J. W. Tay, and L. V. Wang, *Photoacoustically guided wavefront shaping for enhanced optical focusing in scattering media,* Nat. Photonics **9**, 126 (2015).

5

Outlook

In this thesis techniques for high-resolution deep-tissue quantitative optical tomography have been demonstrated. In this context three challenges were defined related to improving imaging depth, contrast, and resolution. This chapter discusses the progress made in these areas, as presented in this thesis, as well as further possible developments in these fields and in optical tomography in general.

5.1. IMAGING DEEP IN TISSUE

A key challenge discussed in this thesis is the improvement of the imaging depth in tissue. With the development of OCPT a significant improvement of the imaging depth in tissue, compared to other optical imaging techniques, was demonstrated. Several factors attributed to the improvement of the imaging depth: First, the high sensitivity for the detection of small signals with the heterodyne detection used in OCT, which makes it possible to detect the low photon count signals associated with optical transmission through thick pieces of tissue. Second, the transmission measurement geometry allows for a factor of 2 increase in imaging depth compared with a reflection measurement geometry. Third, in the transmission measurement geometry all ballistic light is detected instead of the limited detection of backscattered light with a finite collection NA. Fourth, strong suppression of scattered light using confocal gating, coherence gating, and time gating of the transmitted light allows for a significant improvement of imaging depth, as discussed in chapter 4 of this thesis. The use of ballistic light in the image formation makes it possible to achieve higher resolution images than compared to conventional techniques used in imaging turbid media as the resolution is not deteriorated by scattering.

In this thesis we demonstrated an imaging depth of 27 MFP, which was identical to the signal to noise limited detection range. Ultimately the imaging depth of OCPT is limited by shot noise and the maximum acceptable integration time and sample irradiance. As the number of ballistic photons decreases exponentially with depth, the ballistic imaging depth range is limited to several millimeters in tissue considering useful tissue illumination powers. In practice, thicker non-cylindrical samples can be measured with this image range as the measured projections can contain missing angles or missing rays from the sides where the object is too thick to observe any transmission. This allows for OCPT imaging of objects that are larger than 27 MFP in one direction, as these parts of the object are sampled from directions for which the sample is thinner.

In the future, mostly forward scattered non-ballistic photons that have pathlengths that are only a little bit larger than the pathlength of ballistic photons may be included into the image formation. These snake photons still travel in approximately straight paths through scattering media, hence they still contain much of the useful information along the path straight through the object [1]. Snake photons can be used for imaging by treating them as ballistic photons, thereby increasing the signal to noise ratio while slightly reducing the resolution. Alternatively an appropriate light transport model, if available, may be used to compute a widened PSF due to scattering that can be included in the tomographic image reconstruction [2].

5.2. HIGH-RESOLUTION OPTICAL TOMOGRAPHIC IMAGING

Another challenge discussed in this thesis was to provide high-resolution imaging in tissue. In this respect two contributions are made to this issue. First, the developed OCPT imaging system provides high-resolution imaging in deep tissue by strongly reducing the influence of scattered light in the image formation. In chapter 2 we showed that the resolution of the OCPT system is only determined by the imaging optics and not affected by the light scattering in the sample that is measured. Second, a theoretical model was developed for the resolution obtained in optical tomography for an imaging system with a limited depth of focus that is used to measure the projections. This model is tested for both OPT (chapter 2) and OCPT (chapter 4) and provided a spatial filter, which was used to improve the resolution by means of deconvolution algorithms applied to OPT. In the presented work, the theoretical model and corresponding correction algorithm are based on a 2D approximation.

Recently, we implemented a PSF correction inside the tomographic reconstruction algorithm [3, 4] that performs well for non-sparse objects at high signal to noise ratio. This provides an alternative and more versatile method compared to deconvolution based PSF correction. In the future this could make it possible to include other physical phenomena such as scattering and refraction in the reconstruction process. These physical processes are important for many optical tomographic imaging systems. In future work the theoretical model and PSF correction algorithms are extended to 3D geometries, other imaging configurations, and PSFs.

Improving the resolution in optical tomographic imaging systems by numerical algorithms, such as image deconvolution described in this thesis, has its limits. Noise and the finite information content of the measured data ultimately limit the performance of these algorithms. Several approaches can be considered for further resolution improvement: Combining numerical tomographic resolution enhancement techniques with previously reported hardware solutions such as multi-focus scanning [5] or astigmatic imaging [6] potentially can further improve the resolution performance of optical tomographic imaging systems. Additionally non-diffracting beams such as the Bessel beam can be used, instead of the Gaussian shaped beam with limited depth of focus used in this thesis. Bessel beams exhibit a large depth of field for a given resolution (see Fig. 5.1) and their application would reduce the degradation of the tangential resolution towards the edges of the image. The self-healing properties of the Bessel beam may also provide increased imaging depth in turbid media [7].

In many practical cases only a smaller part of a large sample is of interest, for example the zebrafish brain. In this case it is not necessary to image the entire sample with high resolution. The size of the limited region of interest (ROI) allows for using higher numerical aperture lenses that have a smaller depth of field. For ROI tomographic imaging, limited FOV tomography reconstruction algorithms [8, 9] or hardware solutions [10] can be used.

Optical tomography techniques often use reconstruction algorithms developed for straight ray tomography such as X-ray CT. However, the effects of refraction at sample interfaces, diffraction of the focused light beam, absorption and scattering are much stronger in optical tomography compared to X-ray CT. As the performance of optical tomographic imaging devices improves these physical interactions with the object become

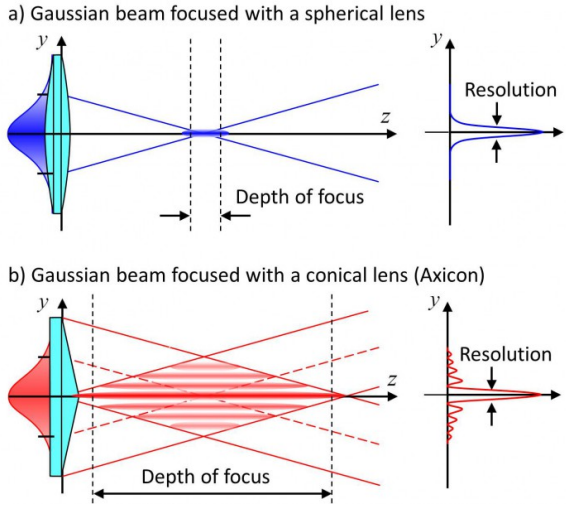

Figure 5.1: Depth and focus and resolution for a Gaussian beam (a) and a Bessel beam (b). Image taken from http://obel.ee.uwa.edu.au/research/techniques/beam-shaping.

important. The effects of diffraction of the focused light beam on the image formation have been extensively discussed in chapter 2 and a correction procedure was proposed. This section discusses some future improvements to the image quality that are possible by incorporating the effects of light propagation in the sample in the reconstruction algorithm.

5.2.1. REFRACTION COMPENSATION

Like light diffraction, refraction also causes light to deviate from the straight ray model used in most tomographic reconstruction algorithms. Refraction at the edges of the sample and on internal interfaces changes the light path causing artifacts in the reconstructed images. Matching the refractive index of the immersion medium with that of the sample is an important experimental method that can strongly improve the obtained image quality. However, index matching with an immersion medium cannot account for refractive index changes inside the sample and hence, not all image artifacts caused by refraction can be prevented in this way. In OCPT, light refraction influences the position and exit angle of the transmitted ballistic light beam causing variations in collection efficiency at the single mode fiber [11]. This effect causes an overestimation of the attenuation coefficient at interfaces in the sample and other artifacts in the reconstructed images.

Some work has been done to include refraction effects in the tomographic image reconstruction by including the ray path in the analysis [12–14]. These algorithms focus on the deviation from the straight ray path. We adapted the reconstruction algorithm to include both the physical ray path as well as the reduced confocal detection efficiency in

OCPT. In this case the reconstruction problem of Eq. 1.3.1 is cast into the form

$$\underset{\mathbf{f}}{\operatorname{argmin}} \quad \|\mathbf{A}(\mathbf{f})\cdot\mathbf{f}-\mathbf{p}\|_2^2. \tag{5.1}$$

In Eq. 5.2.1 the geometry matrix **A** is not fixed but is dependent on the refractive index of the object f. The general scheme of the refraction-correcting reconstruction algorithm is presented in figure 5.2.

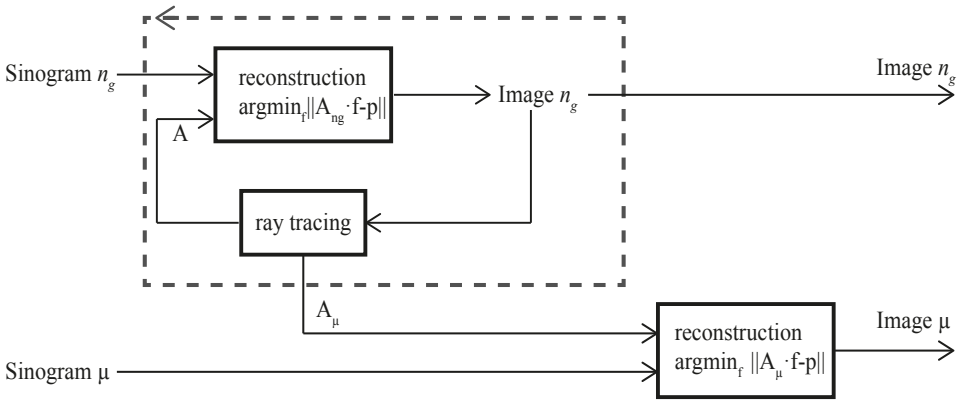

Figure 5.2: Schematic of the refraction-compensated OCPT image reconstruction algorithm that includes non-straight ray trajectories though the object.

Since the refractive index distribution of the sample is measured with OCPT, ray tracing algorithms are applied to find the deviating ray paths for all entries in the sinogram, Fig 5.3(g). The computed ray paths are used to update the weighting matrix $\mathbf{A}_{n_g}(\mathbf{f}_i)$ describing the relationship between the object and pixels in the sinogram. The updated $\mathbf{A}_{n_g}(\mathbf{f}_i)$ matrix is subsequently used in a new optimization to find an improved refractive index image $\mathbf{f}_{i+1}$. This procedure is repeated iteratively to converge to an optimal output image. The final refractive index image and actual ray paths are used to compute the detection efficiencies for every measured ray that are included in $\mathbf{A}_\mu$. Finally, the attenuation sinogram is reconstructed using the final weighting matrix $\mathbf{A}_\mu$ that takes into account the actual ray paths and detection efficiencies.

Figure 5.3 shows a simulation of the reconstruction scheme described above. By ray tracing and solving the forward problem of finding the sinograms **p** from the optical properties a simulated reconstruction can be generated using filtered back projection. These simulated images show strong artifacts induced by beam refraction, Fig. 5.3(b) and (e). Upon application of the iterative scheme described above refraction-corrected images for μ and n_g are computed, the resulting images show a significant reduction of refraction-induced artifacts, as shown in Fig. 5.3(c) and (f). The performance of the refraction-correction algorithm is evaluated by computing the total root-mean-square (rms) error in the reconstructed images. In the presented simulation, images are reconstructed for each version **A**(**f**) using 10 iterations of the MATLAB *lsqr* algorithm. After

10 iterations $\mathbf{A}_{n_g}(\mathbf{f})$ is updated and the optimization continues. Figure 5.3(h) shows the convergence of the total image error versus the number of iterations of the algorithm.

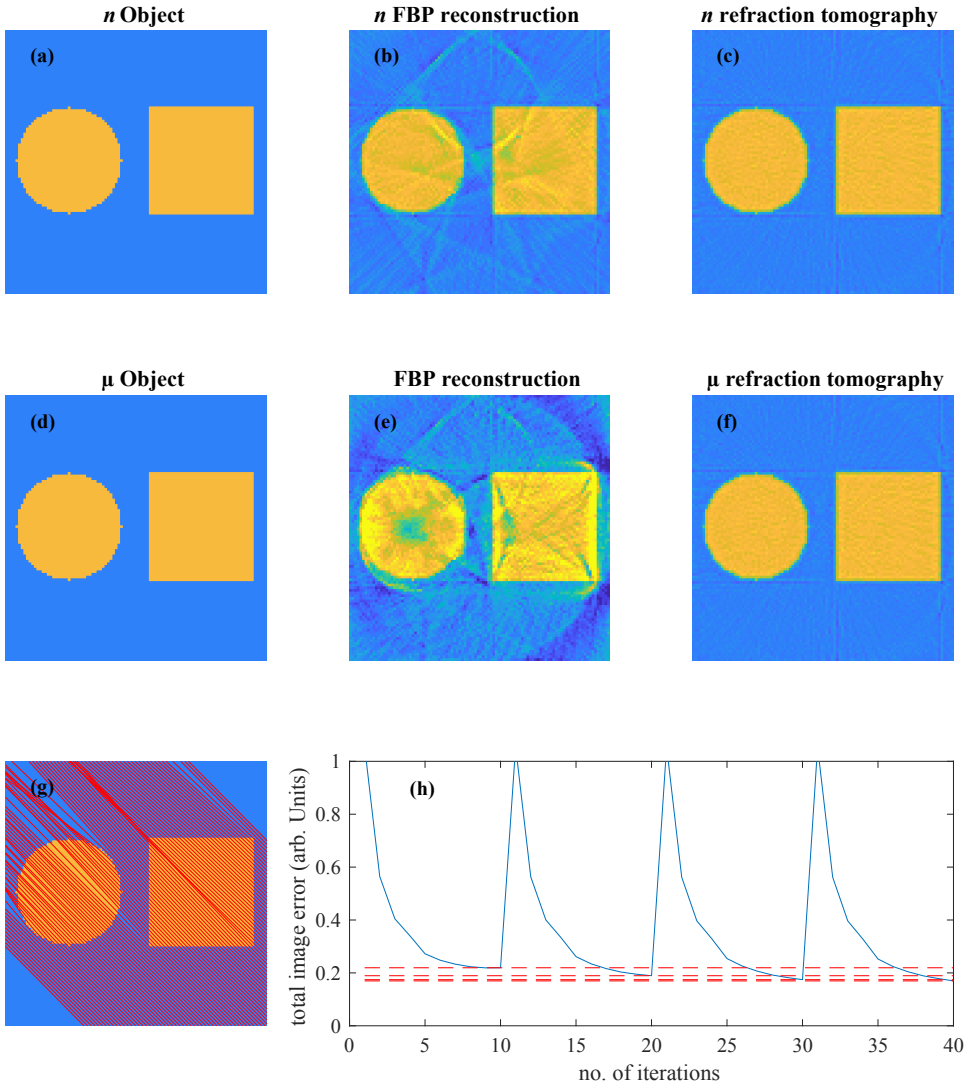

Figure 5.3: Refraction-compensated OCPT image reconstruction. (a)(d) Refractive index and attenuation objects used in the simulation. (b)(e) Reconstruction with straight ray based FBP leads to artifacts in the tomographic images. (c) Refraction corrected refractive index image based on iteratively updated weighting matrix. (f) Refraction corrected reconstructed μ image using a reduced detection efficiency and reconstructed with the most recent weighting matrix. (g) Ray trajectories through an object with refractive index variations of 0.03. (h) Image error versus iteration number.

5.2.2. ATTENUATION COMPENSATION

A second way of using the light propagation models in the tomographic reconstruction is to use the quantitative attenuation images measured with OCPT to improve fluorescence OPT images of the same object. Attenuation of the fluorescence excitation from the excitation source to the probe and emission light from the emitter in general is not taken into account in the tomographic image reconstruction, which leads to image artifacts. Figure 5.4 shows the attenuation of the excitation and emission light for a single location in an object. As the attenuation coefficient of the object can vary locally, the attenuation of the excitation and emission light differs for each object location and projection angle. The OCPT attenuation images can be used to model the light propagation inside the object. Since, OPT and OCPT are not measured using the same wavelength light, the attenuation images measured with OCPT need to be scaled to account for the difference in wavelength.

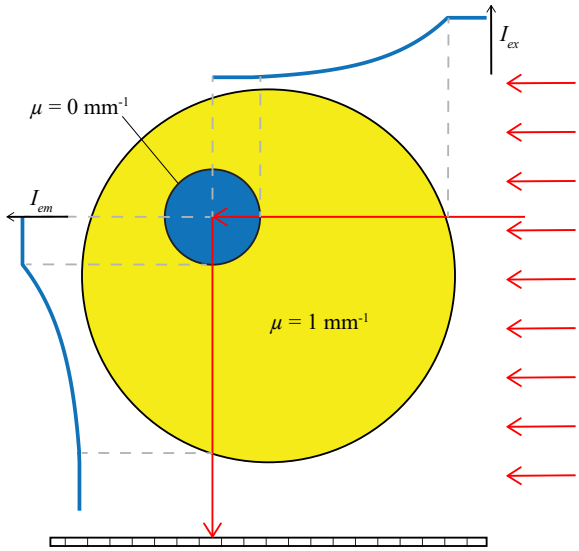

Figure 5.4: The attenuation of fluorescence excitation and emission light by an attenuating object, illustrated for a single object location and projection angle.

With algebraic reconstruction techniques based on Eq. 1.3.1 the effects of attenuation can be included in the reconstruction. Each row in the geometry matrix **A** describes the contributions of each object pixel to a sinogram pixel. The columns of **A** describe the relative contribution of each object pixel to the entire sinogram. In the most simple rectilinear light propagation model, the attenuation of the excitation light by the object can be modelled by an exponential decay described by Eq. 1.1 and calculated for each projection angle. The resulting intensity distribution of the excitation light is used to correct each row of **A**. The attenuation of the emitted fluorescent light can be computed for each object pixel for every projection angle. The resulting attenuation factor is included in **A** by multiplication with the corresponding column segment.

Figure 5.5 shows the results of a simulated measurement and reconstruction with

and without attenuation by the object. The simulation computes the OPT sinogram from the input attenuation image (Fig. 5.5(a)) and the distribution of fluorescent molecules (Fig. 5.5(b)). The sinogram for a fluorescent object embedded in an object with attenuation, shown in Fig. 5.5(d), shows a significant drop in overall signal strength compared to the sinogram in a totally transparent object shown in figure 5.5(c). Furthermore, an angle dependent signal loss can be observed in the attenuation along the sinusoid in the sinogram. Reconstruction of the attenuated sinogram with a normal SIRT reconstruction results in lower contrast and artifacts, as shown in 5.5(e). The SIRT reconstruction of the attenuated sinogram using the adapted geometry matrix is shown in Fig. 5.5(f). By inclusion of the excitation and emission attenuation into the reconstruction, as described above, yields a higher contrast and a reduction of the image artifacts.

5.3. ENHANCED OPTICAL TISSUE CONTRAST

The last challenge discussed in this thesis is to improve contrast. Our contribution is described in chapters 3 and 4 and concerns the quantitative multi-contrast information content of transmission OCT measurements. Transmission OCT, provides contrast in both the group refractive index as well as in the attenuation coefficient. For high signal to noise ratio samples also the dispersive characteristics and wavelength dependent attenuation coefficient can be quantitatively determined (chapter 3).

Future work on increasing the functional information obtained in tissue may focus on using shorter wavelength systems. Many materials show interesting spectral behavior at visible wavelengths, as shown in Fig. 1.3. Implementing, the wavelength dependent refractive index and attenuation information that can be obtained from transmission OCT (Chapter 3) into the path length resolved OCPT imaging reconstruction, provides a way for quantitative 3D imaging of the main tissue constituents such as for example water, fat, and blood.

Another approach that may provide additional contrast in tissue is to make use of the signal from transmitted scattered light. The pathlength distribution measured with OCPT, as shown in Fig. 5.6, may be fitted with a model describing the 3D scattered light transport such as the diffusion equation [15]. This type of analysis may provide information on the scattering anisotropy and the decoupling of the absorption and scattering coefficients.

Refractive index measurements are known to provide information on tissue function and can in some cases be used as a biomarker for disease. We demonstrated the multi-modal contrast in imaging an entire zebrafish using OCPT in chapter 4. In the future, combining OCPT with fluorescence OPT would allow for functional information to be extracted from the measurements. Scattering strongly degrades the resolution and contrast in OPT. Information of attenuation coefficient and refractive indices measured by OCPT could be used to guide the image reconstruction in OPT. With this multi-modal approach, higher quality OPT images potentially can be reconstructed.

Recently, several fluorescent probes operating in the near infrared range have become available and new probes are being developed with improved performance and emission at higher wavelengths [16]. Use of these probes promises an increased imaging depth of fluorescent techniques in tissue, this may facilitate the combination of OCPT and fluorescence OPT for deep-tissue imaging of structure and function.

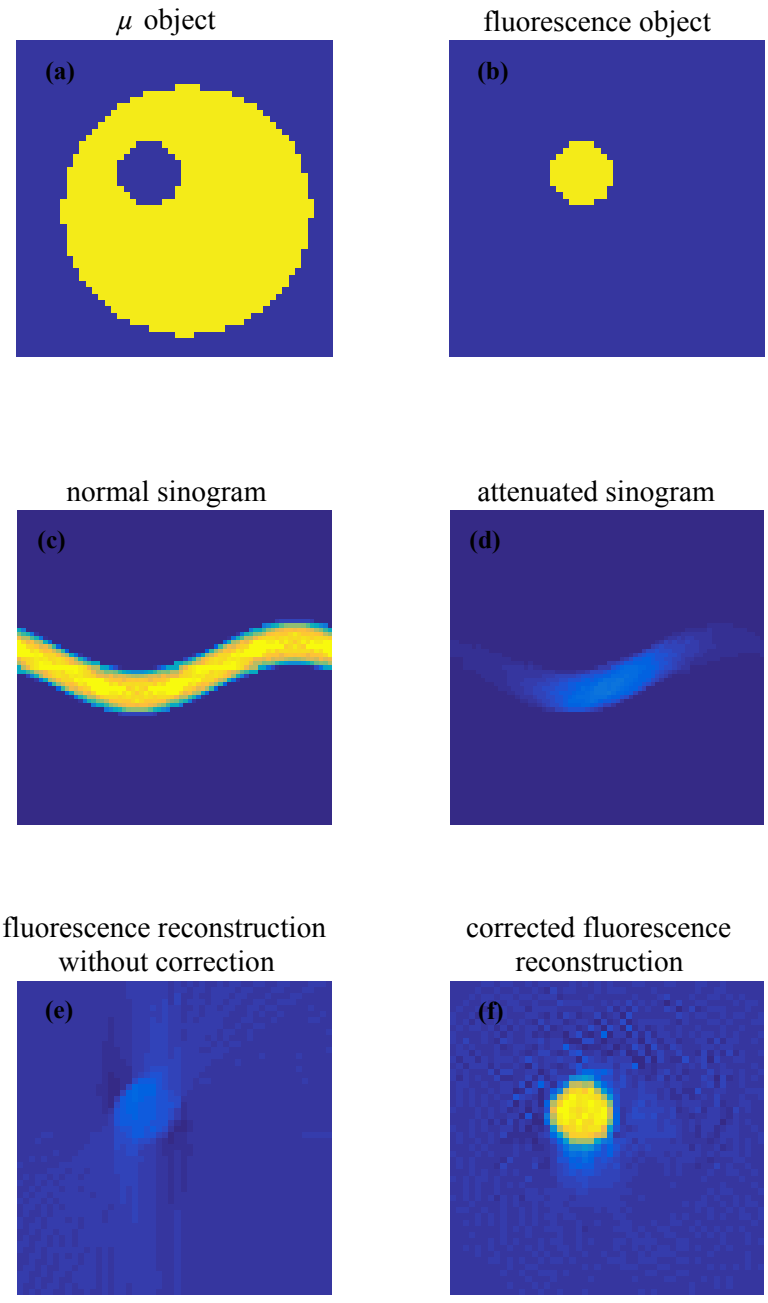

Figure 5.5: Simulation of inclusion of the attenuation of excitation and emission light into the OPT reconstruction using the attenuation measured with OCPT. (a) The OCPT attenuation image. (b) Input distribution of fluorescent molecules. (c) Sinogram without taking attenuation into account. (d) Simulated sinogram with attenuation. (e) Reconstruction of the attenuated sinogram using SIRT. (f) Reconstruction of the attenuated sinogram using SIRT with adapted geometry matrix **A**.

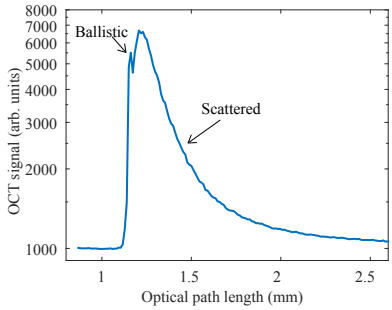

Figure 5.6: Example of a measured path length distribution.

5.4. CONCLUDING REMARKS

This thesis demonstrated techniques for high-resolution deep-tissue quantitative optical tomography. A model for the spatially-varying image resolution in optical tomography is presented in chapter 2. In addition, we present a numerical correction of the images for this spatially-varying resolution. This allows for optical tomographic imaging such as OPT to operate at higher spatial resolutions while still having the same depth range. As such this technique shifts the resolution boundary of this technique downwards, as indicated in 5.7.

In this thesis OCPT is presented as a novel 3D optical imaging modality for quantitative imaging of deep tissue. A thorough theoretical description of the measured OCPT signals is presented in chapter 3 together with experimental validation. In chapter 4 the OCPT system is demonstrated by imaging of both phantoms and biological samples. OCPT provides high resolution images in a range around 4 mm in tissue at resolution of approximately 20 µm. This range is not yet available for fully optical techniques, allowing for novel contrast in its imaging depth range.

Figure 5.7 shows the approximate applicable depth and resolution range of OCPT referenced to the optical techniques mentioned in the introduction of this thesis.

One of the most important improvements needed for the adoption of OCPT to current medical research is the speed enhancement. Currently the speed of the OCPT imaging is limited by the slow mechanical scanning of the sample. Although, in-vivo imaging is possible, it is currently not practical due to the long imaging times. The imaging time can be improved by scanning of the beam instead of the sample. However, this requires scanning both the light excitation and collection paths in identical ways. Use of a beam scanning system is also beneficial for the mechanical stability of the sample, prevent degradation of biological samples over time, and make rapid in-vivo imaging of adult zebrafish possible.

Several steps need to be taken for practical use of OCPT in biological and medical practice. Aside from the speed improvement the system needs to become more robust. The ease of use should be improved by implementing practical and semi-automatic systems for sample mounting and alignment, setting system parameters, data analysis and image reconstruction. Furthermore, a more versatile imaging system needs to be developed that facilitates easy interchange of imaging lenses for imaging different length scale

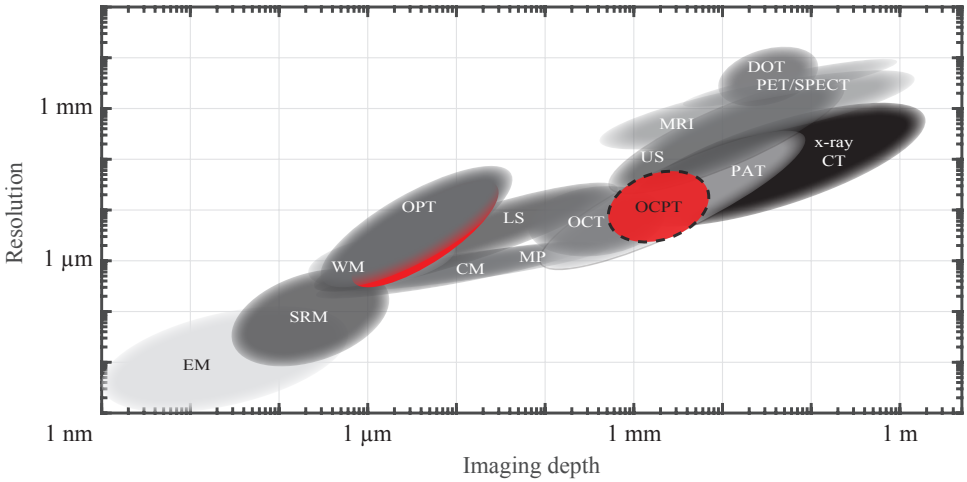

Figure 5.7: Approximate ranges of resolution and imaging depth for 3D imaging techniques including OCPT. EM: electron microscopy, SRM: super-resolution microscopy, WM: widefield microscopy, OPT: optical projection tomography, LS: light sheet microscopy, CM: Confocal microscopy, MP: Multi-photon microscopy, OCT: Optical coherence tomography, PAT: Photoacoustic tomography, US: Ultrasound, MRI: Magnetic resonance imaging, CT: computed tomography, DOT: Diffuse optical tomography, PET: Positron emission tomography, and SPECT: Single photon emission computed tomography. Data combined from [2, 17–21].

objects. Finally, the addition of fluorescent OPT imaging modes to OCPT would allow a wider practical application of the developed techniques.

Aside from zebrafish imaging OCPT is applicable to a wide range of samples of varying size and optical properties. The main advantage over existing modalities is that OCPT is able to image turbid samples with high resolution. Smaller objects that are more scattering such as other small animals or biopsy tissues can be imaged. Alternatively, larger samples with a lower attenuation coefficient can be imaged, such as jellyfish or turbid liquid or gas systems. OCPT may also be applied to quality control in the fabrication industry for example the 3D printing of optics or other semi-transparent objects.

Long after the invention of the first microscope, imaging techniques are still expanding the borders of knowledge in life sciences. Since that first microscope, many imaging modalities have been developed to image with higher resolutions, larger imaging depths, and novel modes of contrast. In this thesis we developed novel quantitative imaging techniques with higher resolution and imaging depth providing a basis for new discoveries in life science.

REFERENCES

[1] T. E. Matthews, M. G. Giacomelli, W. J. Brown, and A. Wax, *Fourier domain multispectral multiple scattering low coherence interferometry,* Appl. Opt. **52**, 8220 (2013).

[2] C. Dunsby and P. French, *Techniques for depth-resolved imaging through turbid media including coherence-gated imaging,* J. Phys. D **36**, R207 (2003).

[3] A. K. Trull, J. van der Horst, W. J. Palenstijn, L. J. van Vliet, T. van Leeuwen, and J. Kalkman, *Point spread function based image reconstruction in optical projection tomography,* Phys. Med. Biol. **62**, 7784 (2017).

[4] A. K. Trull, J. van der Horst, L. J. van Vliet, and J. Kalkman, *Comparison of image reconstruction techniques for optical projection tomography,* Appl. Opt. **57**, 1874 (2018).

[5] K. G. Chan and M. Liebling, *Direct inversion algorithm for focal plane scanning optical projection tomography,* Biomed. Opt. Express **8**, 5349 (2017).

[6] K. Itoh, A. Hayashi, and Y. Ichioka, *Digitized optical microscopy with extended depth of field,* Appl. Opt. **28**, 3487 (1989).

[7] F. O. Fahrbach and A. Rohrbach, *Propagation stability of self-reconstructing bessel beams enables contrast-enhanced imaging in thick media,* Nat. Commun. **3**, ncomms1646 (2012).

[8] A. Ziegler, T. Nielsen, and M. Grass, *Iterative reconstruction of a region of interest for transmission tomography,* Med. Phys. **35**, 1317 (2008).

[9] B. Sahiner and A. E. Yagle, *Region-of-interest tomography using exponential radial sampling,* IEEE Trans. Image Process. **4**, 1120 (1995).

[10] T. Watson, N. Andrews, E. Harry, L. Bugeon, M. J. Dallman, J. A. McGinty, and P. M. French, *Remote focal scanning and sub-volume optical projection tomography,* in *Cancer Imaging and Therapy* (Optical Society of America, 2016) pp. JM3A–15.

[11] S. Yuan and N. A. Riza, *General formula for coupling-loss characterization of single-mode fiber collimators by use of gradient-index rod lenses,* Appl. Opt. **38**, 3214 (1999).

[12] M. A. Haidekker, *Optical transillumination tomography with tolerance against refraction mismatch,* Comput. Methods Programs Biomed. **80**, 225 (2005).

[13] S. J. Doran and D. N. Yatigammana, *Eliminating the need for refractive index matching in optical CT scanners for radiotherapy dosimetry: I. concept and simulations,* Phys. Med. Biol. **57**, 665 (2012).

[14] D. White, *Two-dimensional seismic refraction tomography,* Geophys. J. Int. **97**, 223 (1989).

[15] F. Martelli, S. Del Bianco, A. Ismaelli, and G. Zaccanti, *Light propagation through biological tissue and other diffusive media: Theory,* Solutions, and Software (SPIE Press, Bellingham, 2009) (2010).

[16] G. Hong, S. Diao, J. Chang, A. L. Antaris, C. Chen, B. Zhang, S. Zhao, D. N. Atochin, P. L. Huang, K. I. Andreasson, *et al.*, *Through-skull fluorescence imaging of the brain in a new near-infrared window,* Nat. Photonics **8**, 723 (2014).

[17] V. Ntziachristos, *Going deeper than microscopy: the optical imaging frontier in biology,* Nat. Methods **7**, 603 (2010).

[18] A. A. Appel, M. A. Anastasio, J. C. Larson, and E. M. Brey, *Imaging challenges in biomaterials and tissue engineering,* Biomaterials **34**, 6615 (2013).

[19] S. Manohar, A. van Apeldoorn, and W. Steenbergen, *Photoacoustic imaging: cells make themselves heard,* Nat. Photonics **9**, 216 (2015).

[20] J. Yao and L. V. Wang, *Sensitivity of photoacoustic microscopy,* Photoacoustics **2**, 87 (2014).

[21] G. H. Karunamuni, S. Gu, M. R. Ford, L. M. Peterson, P. Ma, Y. T. Wang, A. M. Rollins, M. W. Jenkins, and M. Watanabe, *Capturing structure and function in an embryonic heart with biophotonic tools,* Front. Physiology **5**, 351 (2014).

SUMMARY

Optical imaging is one of the primary tools in biological and medical research. Over the years many different optical imaging modalities have been developed that have driven the imaging performance in terms of image resolution, contrast, imaging time, and maximum allowed sample size. The goal of this work is to develop techniques for 3D optical imaging of turbid media that provide high resolution and high contrast images deep in tissue.

We focused on improving the resolution in optical tomography systems. The resolution in optical tomography is determined by the performance of the imaging system used to measure the projections. In on-axis focusing the center of the sample is always in focus, while other parts of the measured object are less sharp for some projection angles. After reconstruction this causes blurring of the tomographic images in the tangential direction (in the direction of the angle increment). We derived a description of the spatially-variant resolution in optical tomography based on the through-focus point spread function of the imaging system used to record the projections. The presented resolution model is validated with optical projection tomography (OPT) imaging of fluorescent beads embedded in agarose gel. Based on our theoretically derived resolution model a deconvolution filter for correction of the spatially variant resolution in the tomographic images is developed. On fluorescent bead data, the corrected tomographic images show a homogeneous and isotropic pixel-limited resolution over the entire reconstructed image. The presented technique is demonstrated on a tomographic image of a zebrafish larva showing an improvement of the image quality. In addition, our resolution model provides guidelines for the design of optical tomography systems.

Light scattering deteriorates the resolution and contrast of OPT images of biological tissue as it causes photons to interact with a larger volume of material. Consequently, light scattering acts as a low pass filter reducing the spatial resolution. Since the number of ballistic (non-scattered) photons decays exponentially with depth high resolution imaging in tissue becomes increasingly more difficult with increasing depth. To avoid these problems, we developed a novel interferometric technique for deep tissue imaging based on transmission optical coherence tomography (OCT).

In transmission OCT the sample is placed in the sample arm of a Mach-Zehnder interferometer where the transmitted, broadband light interferes with light from the reference arm. The interference spectrum is measured using a home-build spectrometer. From its Hilbert transform the amplitude and the phase of the interference pattern are determined. For non-scattering media these parameters are used to determine the group refractive index and the group velocity dispersion for various types of glass, ethanol, water, and glucose-water mixtures. For water and suspensions of silica particles the wavelength dependent scattering coefficient is determined. From the Fourier transform of the interference spectrum, the optical path length distribution (OPLD) is determined. In the OPLD the ballistic light, i.e., light travelling straight through the ob-

ject, is selected and used for determination of the scattering coefficient. The obtained scattering coefficients are in good agreement with theoretical calculations based on Mie scattering and dependent scattering.

The transmission OCT technique is used to perform 3D tomographic imaging using ballistic light selection in the OPLD. Transmission OCT provides path length integrated optical properties. From multiple transmission OCT measurements from different lateral positions and angles, quantitative 3D images of the optical properties are reconstructed using tomographic reconstruction techniques. We named this novel imaging modality optical coherence projection tomography (OCPT). OCPT combines sensitive heterodyne detection with strong suppression of scattered photons using coherent gating, confocal gating, and time gating. We present a complete overview of the data acquisition and image reconstruction in OCPT. We obtain an isotropic resolution of 20 μm at the center of the sample. At 1 mm from the center of the sample the resolution in the tangential direction decays to approximately 40 μm. This resolution is fully determined by the properties of the sample arm lenses used in the imaging system and is not degraded by light scattering in the sample. With tissue phantoms we tested the quantitative OCPT imaging of the group refractive index and attenuation coefficients imaged and found good agreement with reference values. We demonstrate OCPT on tissue by imaging a full adult zebrafish, achieving an unprecedented imaging depth of 4 mm, equivalent to 27 mean free paths (MFP) of photon transport without the use of optical clearing. Image segmentation algorithms are applied to the volumetric images to compute the volume averaged group refractive index and attenuation coefficients of multiple zebrafish organs. Furthermore, we demonstrated that the measurement of the optical path length distribution of the photons transmitted by the sample allows for applying time varying detection gates enabling a wide range of contrast types for qualitative image assessment and tissue segmentation purposes.

We indicate how, in the future, OCPT can be improved by: implementing beam scanning to reduce the image acquisition time, using multi-focus, or Bessel beam imaging to obtain higher resolution, and to include the beam-shape and refraction in the tomographic reconstruction to obtain improved image quality. Multimodal imaging by combining OPT and OCPT may allow an improved image quality by correcting for refraction, fluorescence absorption and scattering.

In this thesis we pushed the spatial resolution limits of OPT downwards. In addition, a new imaging modality is developed that enables imaging of millimeter sized objects with quantitative contrast and resolutions in the 10 μm range.

SAMENVATTING

Optische beeldvorming is een van de belangrijkste instrumenten in biologisch en medisch onderzoek. Door de jaren heen zijn er veel verschillende optische beeldvormingsmodaliteiten ontwikkeld met voortschrijdende prestaties op het gebied van spatiele resolutie, contrast, beeldvormingstijd, en de maximum toelaatbare objectgrote. Het doel van dit werk is om technieken te ontwikkelen voor 3D optische beeldvorming van troebele media die een hoge resolutie en hoog contrast bieden in weefsel.

We hebben ons gericht op het verbeteren van de resolutie in optische tomografiesystemen. De resolutie in optische tomografie wordt bepaald door de prestaties van het beeldvormingssysteem dat wordt gebruikt om de projecties te meten. Bij focussering op de rotatie-as is het centrum van het monster altijd scherpgesteld, terwijl andere delen van het gemeten object minder scherp zijn voor sommige projectiehoeken. Na reconstructie veroorzaakt dit vervaging van de tomografische beelden in de tangentiële richting (in de richting van de hoektoename). We hebben een beschrijving van de ruimtelijk-variabele resolutie in optische tomografie afgeleid op basis van de door-focus punt spreidingsfunctie van het beeldvormingssysteem dat wordt gebruikt om de projecties te registreren. Het gepresenteerde resolutiemodel is gevalideerd met optische projectietomografie (OPT) van fluorescerende deeltjes ingebed in agarosegel. Op basis van het door ons theoretisch afgeleide resolutiemodel is een deconvolutiefilter ontwikkeld voor correctie van de ruimtelijk afwijkende resolutie in de tomografische beelden. Bij de opnames van fluorescente deeltjes vertonen de gecorrigeerde tomografische afbeeldingen een homogene en isotrope pixel-gelimiteerde resolutie over het gehele gereconstrueerde beeld. De gepresenteerde techniek is gedemonstreerd op een tomografisch beeld van een zebravislarve die een verbetering van de beeldkwaliteit laat zien. Daarnaast biedt ons resolutiemodel richtlijnen voor het ontwerp van optische tomografiesystemen.

Lichtverstrooiing verslechtert de resolutie en het contrast van OPT beelden van biologisch weefsel omdat fotonen door verstrooiing interacteren met een groter volume aan materiaal. Hierdoor werkt het als een laagdoorlaatfilter dat de ruimtelijke resolutie vermindert. Omdat het aantal ballistische (niet-verstrooide) fotonen exponentieel afneemt met de diepte, wordt beeldvorming met hoge resolutie in weefsel steeds moeilijker met toenemende diepte. Om deze problemen te voorkomen, hebben we een nieuwe interferometrische techniek ontwikkeld voor optische beeldvorming diep in weefsels op basis van transmissie optische coherentietomografie (OCT).

In transmissie OCT wordt het monster in de monsterarm van een Mach-Zehnder interferometer geplaatst waar het doorgelaten breedbandige licht interfereert met licht van de referentiearm. Het interferentiespectrum wordt gemeten met behulp van een spectrometer. Uit de Hilbert-transformatie van het gemeten signaal worden de amplitude en de fase van het interferentiepatroon bepaald. Voor niet-verstrooiende media worden deze parameters gebruikt om de groepsbrekingsindex en de groepsnelheids-

dispersie voor ethanol, water, verschillende soorten glas, en glucose-watermengsels te bepalen. Voor water en suspensies van silicadeeltjes wordt de golflengte-afhankelijke verstrooiingscoëfficiënt bepaald. Uit de Fouriertransformatie van het interferentiespectrum wordt de optische padlengteverdeling (OPLD) bepaald. In de OPLD wordt het ballistische licht, d.w.z. licht dat recht door het voorwerp is gereisd, geselecteerd en gebruikt voor het bepalen van de verstrooiingscoëfficiënt. De verkregen verstrooiingscoëfficiënten komen goed overeen met theoretische berekeningen op basis van Mie-verstrooiing en concentratie afhankelijke verstrooiing.

De transmissie OCT-techniek is toegepast om 3D-tomografische beeldvorming te doen gebruikmakend van ballistische lichtselectie in de OPLD. Transmissie OCT meet padlengte geïntegreerde optische eigenschappen. Uit transmissie OCT-metingen met vanuit verschillende laterale posities en hoeken, worden kwantitatieve 3D beelden van de optische eigenschappen gereconstrueerd met behulp van tomografische reconstructietechnieken. We noemden deze nieuwe beeldvormingsmodaliteit optische coherentie projectie tomografie (OCPT). OCPT combineert gevoelige heterodyne detectie met sterke onderdrukking van verstrooide fotonen met behulp van coherentie-selectie, confocale selectie en reistijdselectie. We presenteren een compleet overzicht van de dataacquisitie en beeldreconstructie in OCPT. Het OCPT systeem heeft een isotrope resolutie van 20 µm in het midden van het beeld. Op 1 mm van het midden van het beeld vervalt de resolutie in de tangentiële richting tot ongeveer 40 µm. Deze resolutie wordt volledig bepaald door de eigenschappen van de lenzen van de monsterarm die in het beeldvormingssysteem worden gebruikt en wordt niet verslechtert door lichtverstrooiing in het monster. Met weefselfantomen hebben we de kwantitatieve OCPT beeldvorming van de groepsbrekingsindex en verzwakkingscoëfficiënten in beeld gebracht en een goede overeenstemming met referentiewaarden gevonden. We demonstreren OCPT op weefsel met een volwassen zebravis en bereiken een ongekende indringdiepte van 4 mm, gelijk aan 27 gemiddelde vrije weglengtes (MFP) van fotonentransport zonder chemische optische weefselopheldering. Beeldsegmentatiealgoritmen zijn toegepast op de volumetrische afbeeldingen om de volume-gemiddelde groepbrekingsindex en verzwakkingscoëfficiënten van meerdere zebravisorganen te berekenen. Verder hebben we aangetoond dat de meting van de optische padlengteverdelingen van de getransmitteerde fotonen een flexibele selectie op basis van reistijd toestaat wat een breed scala van contrasttypes mogelijk maakt voor kwalitatieve beeldbeoordeling en weefselsegmentatiedoeleinden.

In de toekomst kan OCPT verbeterd worden door: het toepassen van bundel scanning om de beeldacquisitietijd te verkorten, een multi-focus of een Besselbundel te gebruiken voor een hogere resolutie, de bundelvorm en lichtbreking op te nemen in de tomografische reconstructie om een verbeterde beeldkwaliteit te verkrijgen. Tevens kan multimodale beeldvorming door OPT en OCPT te combineren een verbeterde beeldkwaliteit mogelijk maken door correctie voor breking, fluorescentie-absorptie en verstrooiing.

In dit proefschrift hebben we de spatiele resolutielimieten van OPT naar beneden geschoven. Daarnaast is een nieuwe beeldvormingsmodaliteit ontwikkeld die optische beeldvorming van millimetergrote objecten mogelijk maakt met kwantitatief contrast en resoluties rond 10 µm.

CURRICULUM VITÆ

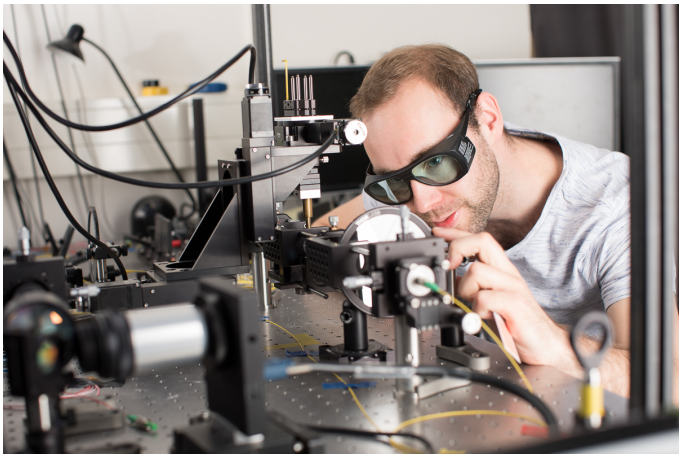

Jelle van der Horst

Jelle van der Horst was born in Utrecht, the Netherlands on 19 July 1988. He obtained his BSc degree in applied physics from Eindhoven University of Technology in 2010 with a minor in education and communication. The topic of his BSc thesis was the determination of bead out-of-focus position in microscopy. Afterwards, he obtained his MSc degree from Eindhoven University of Technology, specialising in fluid mechanics and medical physics. His MSc. research was on the topic of enhanced groundwater remediation by chaotic advection. During his MSc education he also obtained a certificate in business administration.

In January 2014 he started his PhD in the department of imaging physics at Delft University of Technology. His project was on 3D optical tomography imaging of scattering objects, described in this thesis.

Since January 2018, he is a post-doc researcher in optical tomography at Delft University of Technology.

List of Publications

Publications contributing to this thesis

[1] **J. van der Horst**, A. K. Trull, and J. Kalkman, *Deep-tissue label-free quantitative optical tomography*, Manuscript in preparation.

[2] **J. van der Horst** and J. Kalkman, *Image resolution and deconvolution in optical tomography*, Optics Express, 24(21), 24460-24472, (2016).

[3] A. K. Trull[1], **J. van der Horst**[1], J. G. Bijster, and J. Kalkman, *Transmission optical coherence tomography based measurement of optical material properties*, Optics Express, 23(26), 33550-33563, (2015).

Other publications

[1] A. K. Trull, **J. van der Horst**, L. J. van Vliet, and J. Kalkman, *Comparison of image reconstruction techniques for optical projection tomography*, Applied Optics, 57(8), 1874-1882, (2018).

[2] A. K. Trull, **J. van der Horst**, W. J. Palenstrijn, L. J. van Vliet, T. van Leeuwen, and J. Kalkman, *Point spread function based image reconstruction in optical projection tomography*, Physics in Medicine & Biology, 62(19), 7784, (2017).

[3] **J. van der Horst** and J. Kalkman, *Frequency domain analysis of spatially-varying image resolution in optical projection tomography*, Computational optical sensing and imaging, Optical society of America, p. CW2D. 2 (2016).

[1] These authors contributed equally to this work

ACKNOWLEDGEMENTS

Working on this PhD thesis was a nice adventure and a lot of fun, made possible with the help of many great people.

First, I would like to thank my co-promotor Jeroen for giving me the opportunity to work on this project, introducing me to the field of optics, his enthusiasm, and patient supervision. I really enjoyed our collaboration and many of our discussions on how to tackle our imaging issues.

I would also like to thank my promotor Lucas for providing excellent supervison. During our many progress meetings you took the time to discuss my work, always keeping in mind the bigger picture and personal development and the fun of doing research.

Also, thanks to Tjakko and Herma of the Erasmus Medical Centre, for their help with the zebrafish experiments.

In the Quantitative Imaging Group I would especially like to thank Annelies, Ronald and Ron. Not only for all the help you provided over the years but also for contributing to the great atmosphere in our group.

I would also like to thank all the other (former) group members of the the Quantitative Imaging Group for the many nice coffee breaks, foosball games, friday afternoon drinks and much more. Jeroen H, Lena, Christiaan, Jelle (the other one), and Anna for the nice atmosphere in the office. Mojtaba, for the great times in the lab, and the many foosball games. I believe we still have some matches to play. Nadya, it was always fun to have you around in the lab. Boling (Mr. Tea), for introducing me to Chinese tea. Robert M, the reason for working at home on Wednesdays, for the bad jokes and many after work drinks. Leon, Gyllion and Jos for helping me continue the foosball madness. And all the other group members; Alois, Babak, Bernd, Davide, Dirk, Ellen, Emile, Frans, Hamidreza, Jaap, Jelena, Jeroen S, Jianfei, Joor, Joost, Juan Pedro, Kedir, Koen, Lisa, Mohammed, Pierre, Piet, Rasmus, Richard, Robiel, Robert N, Roel, Sjoerd, Taylor, Ted, Tian, Tom, Vincent, Willem, Yan and Zhang,

Finally I would like to thank my family and friends for their fun and support, especially Renske, who had a front row seat to the whole thing.

Jelle van der Horst
Delft, march 2017